Classe di Scienze

PhD Thesis in Molecular Biophysics

Unraveling alterations of excitation/inhibition balance in *in vivo* models of epilepsy and genetic autism

Candidate:

Enrico Pracucci

Supervisor:

Prof. Gian Michele Ratto

2018/2019

Preface

During my years as PhD student, I had the opportunity to be involved in a few different projects and learn about several experimental techniques. This period was also important to better understand how research works and to think carefully about my future as a researcher and to start working for it (Vannini et al. 2014; Pederzoli et al. 2016; Petrucco et al. 2017; Sulis Sato et al. 2017; Cozzolino et al. 2018).

My main project is about the study of excitation and inhibition balance in the mammalian cortex. In this project, I mostly performed electrophysiology on mice models for neurological diseases and performed two-photon microscopy on mice. Electrophysiology is one of the oldest techniques used in neuroscience and is still a field of study that can give us precious insight of brain functions, since it measures, the currents generated by neurons during their functioning. Another tool for getting a closer look to the working brain is a more recent technique: two-photon microscopy. This technique allows the researcher to image the live brain and study its functions with minimal interference with the brain integrity.

With two-photon imaging, I was able to visualize important intracellular ionic changes (for calcium and chloride) as they happened in the live animal, without the use of invasive techniques like the ones needed for recording electrophysiology.

My PhD thesis will focus mostly on the role of the excitation/inhibition equilibrium in drug-induced epilepsy-like models and in a genetic epilepsy model. Here, I would like to mention briefly another project I was involved into and that led to a publication. Over these few years, I have developed a mouse model of glioblastoma, one of the most malignant and lethal tumors that affect humans, and still the most common type of brain cancer. The model was obtained by injecting glioblastoma cancer cells directly into the mouse brain, allowing a tumor to be formed.

I have developed this model starting from glioma cells, that I have stably transfected with DNA encoding different fluorescent proteins and a genetically encoded fluorescent calcium sensor (GCaMP6s).

This model was supposed to be instrumental to test biocompatible nanoparticles that were produced by Francesca Pederzoli in Giovanni Tosi's laboratory (University of Modena). These nanoparticles have a potential to be used in human treatment of glioblastoma, since their superficial functionalization allows them to pass the blood brain barrier when injected into the blood stream.

In this study, I have performed the biophysical and photophysical characterization of these nanoparticles (Pederzoli et al. 2016). Then I trained a PhD student who is now continuing the project on glioblastoma and who has now produced a new model of inducible glioblastoma to overcome the limitations of the previous model.

During my PhD course, I participated in the following published studies:

Peer-Reviewed Original Research

1. Sulis Sato, S., Artoni, P., Landi, S., Cozzolino, O., Parra, R., **Pracucci, E.**, Trovato, F., Szczurkowska, J., Luin, S., Arosio, D., Beltram, F., Cancedda, L., Kaila, K., Ratto, G.M. (2017) Simultaneous two-photon imaging of intracellular chloride concentration and pH in mouse pyramidal neurons in vivo. *Proc Natl Acad Sci U S A*. 114(41):E8770-E8779. doi: 10.1073/pnas.1702861114.

2. Petrucco, L.*, **Pracucci, E.***, Brondi, M., Ratto, G.M., and Landi, S. (2017). Epileptiform activity in the mouse visual cortex interferes with cortical processing in connected areas. *Sci. Rep*. 7:40054.
   *Equal contributors.

3. Pederzoli, F., Ruozi, B., **Pracucci, E.**, Signore, G., Zapparoli, M., Forni, F., Vandelli, M.A., Ratto, G., and Tosi, G. (2016). Nanoimaging: photophysical and pharmaceutical characterization of poly-lactide-co-glycolide nanoparticles engineered with quantum dots. *Nanotechnology* 27(1):015704.

4. Vannini, E., Panighini, A., Cerri, C., Fabbri, A., Lisi, S., **Pracucci, E.**, Benedetto, N., Vannozzi, R., Fiorentini, C., Caleo, M., and Costa, M. (2014). The bacterial protein toxin, cytotoxic necrotizing factor 1 (CNF1) provides long-term survival in a murine glioma model. *BMC Cancer* 14:449.

Other Publications in Peer-Reviewed Journals

1. Cozzolino, O., Marchese, M., Trovato, F., **Pracucci, E.**, Ratto, G.M., Buzzi, G., Sicca, F., Santorelli, F.M., (2018) Understanding spreading depression from headache to sudden unexpected death. *Frontiers Neurology* 9:19.

Abstract

One prominent feature of brain computation is the excitation inhibition balance (E/I balance) that represents one of the main homeostatic functions of the brain. Its aim is to maintain the neural circuits in a narrow and safe range of action. Within this range, the brain network can receive and analyze sensory inputs and produce a modulated output, proportional to the stimuli intensity. Any imbalance in this equilibrium leads to abnormal responses to external stimuli and results in pathological behavior.

Indeed, neurological pathologies known for featuring a deep alteration of the E-I balance are epilepsy and autism, which often occur together in the same patient. Several human genetic syndromes caused by alterations of genes involved in neural development feature signs like autism and epilepsy. Thus, they represent important cases for studying and understanding the role of these single altered genes in the development and regulation of the brain balance. In return, we hope that this knowledge of these genes and more generally of human brain network can be useful in treating the patients affected by these conditions and can help us improve their quality of life.

In my work, I studied the regulation of the E/I balance in mouse models of neurological diseases from three different points of view.

In the first set of experiments, I studied the E/I balance in a focal model of epileptiform activity. This model is produced by the local application of bicuculline to the mouse cortex. Bicuculline is a competitive $GABA_A$ receptor antagonist that, when applied, leads to the development of persistent and periodic interictal spikes at the injection site, while activity appears to be normal in nearby areas that are not reached by bicuculline. In our experiments, we showed that, even in the apparently normal area, there is a disruption of cortical computation. Specifically, the disruption occurs whenever an interictal spike is generated in the epileptic focus. This can have important impact on our understanding of epilepsy and of its treatment since interictal spikes are a common feature not only of epileptic patients, but can also appear in non-epileptic subject, apparently without any consequence. From our results, we concluded that interictal activity can actually interfere with brain operation not only in the center of the epileptiform activity, but also in the connected areas, where the E/I balance is not directly disrupted. These results provide an example of the fact that apparently non-symptomatic interictal spikes can affect brain computation.

The second experimental model that I studied is a mouse model for a specific human genetic disease: the Phelan-McDermid syndrome. This is a developmental disease, caused by a genomic deletion at site 22q13. The main suspect for causing the disease is one gene, Shank3, which encodes for a scaffold protein localized in the post-synaptic density of glutamatergic synapses.

In this model, we studied the computation of visual stimuli and we found an alteration of the contrast-response curve. This is a defining relationship of visual processing: it is the transfer function that converts the visual input into a neural output. This means that to each intensity of visual stimulation corresponds a certain intensity of the neural response, of the visual cortex. We determined that, in Shank3 mutant mice, this curve was altered and showed an increased response to less intense stimuli and showed also a poor modulation of responses to high-contrast stimulations. An interpretation of this can be that these mice are more sensitive to low-contrast stimuli, but completely lose the ability of telling apart different high-contrast stimuli from each other. Therefore, the Phelan McDermid mouse becomes “blinded” by weak stimulations as if they were seeing strong stimulus.

Finally, we studied the behavior of the chloride ion in a drug-induced epileptic seizure model. Chloride ion is of pivotal importance in neurons were the activation of ionotropic GABA and glycine receptors, which increase chloride membrane conductance in response to GABA or glycine release

respectively. The intracellular concentration of chloride ions decides what is the effect of GABA release. Traditionally, ionotropic GABA receptors activation was thought to be inhibitory only, but the excitatory or inhibitory nature of these receptors is determined by the intracellular concentration of chloride ions. This concentration in normal adult neurons is thought to be around 5 mM: at this concentration, the effect of the activation of GABA receptors is an inhibition of the postsynaptic element. We investigated if the chloride concentration can be varied under extreme pathologic conditions as during epileptic seizures in a drug induced mouse model. In these animals, the epileptic seizures were produced by local administration of 4-aminopyridine (4-AP), a potassium channel antagonist. The effect of 4-AP is to cause accumulation of chloride ions in neurons and this suggests that, in epileptic crisis, the role of inhibitory neurons can actually favor excitation.

Index

Preface I
Abstract IV
Chapter 1: Epileptiform activity effect on connected areas 1
1.1 Introduction 1
1.1.1 Epilepsy 1
1.1.2 Recording brain activity: Local Field Potential 1
1.1.3 Cortical oscillations: a physiological network phenomenon 2
1.1.4 Epilepsy: an aberrant network phenomenon 3
1.1.5 Interictal activity 4
1.2 Materials and Methods 6
1.2.1 Mouse preparation 6
1.2.2 Local field potential and loose-patch recordings 6
1.2.3 Two-photon calcium imaging combined with LFP recordings 7
1.2.4 Visual evoked potentials (VEPs) 7
1.2.5 Data analysis 7
1.3 Results 10
1.3.1 Slow-wave oscillations are synchronized between hemispheres 10
1.3.2 ISs cause the fragmentation of up states in the opposite hemisphere 11
1.3.3 ISs alter the neuronal firing probability in the contralateral hemisphere 16
1.3.4 Contralateral interictal spikes interfere with visual processing in the non-treated hemisphere 18
1.4 Discussion 21
Chapter 2: : Gain adaptation disruption in an autism-related model 23
2.1 Introduction 23
2.1.1 Phelan McDermid Syndrome 23
2.1.2 Shank3 23
2.1.3 Mouse models of PMS 25
2.1.4 Contrast response curve and gain adaptation 26
2.1.5 Parvalbumin interneurons as modulators of gain adaptation 28
2.2 Materials and methods 30
2.2.1 Mouse model 30
2.2.2 Surgical procedures 30
2.2.3 Electrophysiology recording and visual stimulation 30
2.2.4 Up states and down states detection 30
2.2.5 Spectrogram 31

2.2.6 Analysis of Visual Evoked Responses 31
2.2.7 Power spectra 31
2.2.8 Power computation of traces 31
2.2.9 Spectrogram 32
2.2.10 Recording from human subjects 32
2.3 Results 34
2.3.1 Steady state analysis showed increased activity 34
2.3.2 Gain control is impaired in Shank KO mice 36
2.3.3 Pharmacological enhancement of mGluR5 pathway affects gain control acting on visual processing 38
2.3.4 Recording in human. The problem of timing. 40
2.3.5 Hermes. A simple system to synchronize stimulation and recording 41
2.3.6 Hermes-based *in vivo* recording 43
2.4 Discussion 45
2.3 Chapter 3: : Chloride concentration measurement and GABAergic inhibition inv lem o sh. @ ec

Chapter 1: Epileptiform activity effect on connected areas

Work published as:

Petrucco L., Pracucci E., Brondi M., Ratto G.M., Landi S. Epileptiform activity in the mouse visual cortex interferes with cortical processing in connected areas. Sci Rep. 2017 Jan 10;7:40054.

1.1 Introduction

1.1.1 Epilepsy

Epilepsy is one of the most common neurological pathologies. It affects 70 million people worldwide and every year, 2.4 million people are diagnosed with this disease. Its main feature is the enduring predisposition to develop seizures. Seizures are a transient behavioral status, that can be either manifested as sign or subjective symptom (Fisher et al. 2014). The most common type of seizures have a convulsive nature with major motor signs, but more generally seizures can have motor, sensory, psychic or autonomic manifestations. Seizures are characterized by a change in the clinical state of the patient caused by an excessive neuronal firing or depolarization of brain neurons, which can start spontaneously for an intrinsic instability of the brain network or can be induced by an external triggering stimulus (also in this case the network must have a degree of intrinsic instability, that the external stimulus exacerbates).

The International League Against Epilepsy gave a working definition for epilepsy (Fisher et al. 2014, 2018; Scheffer et al. 2018), according to which epilepsy is when either two of the following conditions are met:

1) Two or more seizures occurring more than 24 hours apart.

2) One unprovoked seizure must occur and the probability of further seizures over the next 10 years.

After the first events that indicate that an epileptic seizure occurred, the patients undergo medical evaluations that try to do a precise diagnose of the disease in a multi-step process. A careful diagnosis is vital, because a misdiagnosis of epilepsy could lead to an abuse of anti-seizure drugs, which can produce adverse effects, and the failure to diagnose the true disease. Conversely, an undiagnosed epilepsy condition can be very dangerous and possibly lethal, because of the lack of specific treatment to prevent possibly severe conditions.

The diagnosis of epilepsy is performed with different medical evaluations, namely the assessment of medical history, physical examination, EEG and neuroimaging. In these tests, doctors exclude other diagnosis first, then apply the working definition of epilepsy and assess the type of epilepsy and epileptic seizure (Fisher et al. 2014). The electrophysiological recording of brain activity is essential in the evaluation of the epilepsy in human patients and is also an important tool for the study of animal models of epilepsy.

1.1.2 Recording brain activity: Local Field Potential

One of the classical ways of recording electrical activity from mammalian cortex is to insert in the cortical area of interest a small extracellular electrode. According to the physical properties of this electrode and of the amplifying device connected to it, the recorded electrical signal is called Local

Field Potential (LFP), and carries information about the activity of the population of neurons localized in the volume surrounding the electrode. In the LFP, it is possible also to single out contributions from single neurons (called "single units") but only if they are close enough to the electrode (<65 µm (Gray et al. 1995)); single units are visible in the LFP as fast spikes, that are the LFP correlates of single action potentials. Single units can be observed only in a frequency band >500 Hz. Lower frequency components (0-300 Hz) of the LFP are the result of the integration of population neuronal activity. In particular, the LFP is estimated to be representing the activity of a total volume with a diameter of 280 µm, in layer 2/3 of visual cortex (Xing, Yeh, and Shapley 2009).

The relationship between the recorded LFP signal and its sources is very complex and is strongly influenced by the composition of the brain volume (Buzsáki, Anastassiou, and Koch 2012): currents propagating in the volume, meet an alternation of fluids and membranes and only 6% of this volume is occupied by extracellular fluids, while all the rest is occupied by axons, dendrites, glial cells. Since all these components have very different conductivity and permittivity, it is not surprising that the brain tissue is electrically highly nonhomogeneous and this fact contributes to the frequency-filtering properties observed in the LFPs (Bédard, Kröger, and Destexhe 2004). In general, the power of the LFP decreases with the frequency as P=1/f, where P is the power spectral density (a quantification of how much energy is in each frequency component of LFP) and f is the frequency (Buzsáki and Draguhn 2004).

LFP recording in the cortex allows the evaluation of the physiological status of the cortex (e.g. by the analysis of naturally occurring brain oscillations) and its processing capability (like the responsiveness to sensory stimulation). Regarding the responsiveness to sensory information, it has been demonstrated that stimulus-evoked spiking activity induces ש ב ş a (Esghaei, Daliri, and Treue 2017). For this reason, the activity of the primary visual cortex in response to visual stimuli can be measured with LFP recording as a visual evoked potential (VEP).

As stated above, the LFP can also allow evaluation of other physiological features of the brain, one of which is cortical oscillations, an old subject of study in neuroscience that is still not completely understood, but it is known to be essential to brain functions.

1.1.3 Cortical oscillations: a physiological network phenomenon

In mammalian cortex, several different oscillations or rhythms can be measured by recording LFP, and are classified according to their characteristic frequency of oscillation. They are believed to be involved in information processing, learning, behavior, sleep (X.-J. Wang 2010) and to be essential to the well-being of the brain, since several neurological diseases are associated with an impairment in oscillations (Assenza et al. 2017; Ahnaou et al. 2017; Holt et al. 2019).

A wide body of work is directed to the understanding of the yet largely mysterious underlying cellular mechanisms, and it is emerging that the origin of the brain rhythms can be tracked down to the coordinated interaction between excitatory and inhibitory neurons. The presence of a rhythm in an LFP trace is in fact the electrophysiological correlate of a neuronal network synchronization, which means that ש ב opulation of neurons are all firing rhythmi cally and in phase with each other. For this to happen, it is fundamental that there is a very strictly regulated interplay of inhibitory and excitatory components (Zhou and Yu 2018; Dupret, Pleydell-Bouverie, and Csicsvari 2008), that make the network oscillate. For this reason any disruption of oscillations suggests an impairment in the excitation/inhibition equilibrium.

One of the most studied rhythms of the cortex are gamma oscillations, which are defined as oscillations in the 20-80 Hz frequency range. The function and exact mechanism of this rhythm are

still a matter of debate, but it is believed to be associated to attentive behavioral states and to play a role in the integration of sensory information. For example, gamma oscillations can be observed in the visual cortex in response to a visual stimulation and here the synchronization that occurs during these oscillations makes the responding neurons emerge from the random noise of sporadic activity that usually is found in the cortex. For this reason, one hypothesis for the role of the gamma oscillations is to activate a sufficient number of neurons, so that their collective spiking can elicit a strong activation of the postsynaptic neuron (Buzsáki and Wang 2012).

Another important rhythm that is found in the cortex is the slow wave activity (SWA), which is characterized by a slow frequency of oscillation in the 0.75-4 Hz range and that is typical of a specific sleep phase (slow wave sleep) and of some forms of anesthesia. Slow wave activity is peculiar in its special pattern: it involves all of the cortex during slow wave sleep, so all neurons of all cortical areas oscillate in phase with each other (Massimini et al. 2004). This reason for this massive recruitment in these oscillations is still poorly known, but what is known is that it is of critical importance for the brain functioning. In experiments where the SWA has been disrupted, the subjects' learning capabilities were impaired (Aeschbach 2009). Also, in several neurological diseases, SWA is disrupted or abnormal, confirming the importance of this oscillation (Weisman and McKeith 2007; Kyllerman 2013; Halász et al. 2019).

During SWA, neurons oscillate between two states of polarization, called up states and down states, in which neurons are respectively depolarized (subthreshold) and in resting state. Therefore during up states neurons are closer to their threshold potential and their firing rate is increased. The origin of slow wave activity is debated, one area that has often been proposed to play a key role in slow wave generation is the thalamus through thalamo-cortical fibers. Even though the isolated cortex and thalamus retain some slow-wave generation capabilities, thalamocortical network has been proposed to be the single functional and dynamic unit that is able to generate the SWA (Crunelli et al. 2015). In a work from the group of Tommaso Fellin (Zucca et al. 2017), a critical role was found for cortical interneurons in SWA and in particular they were seen to be involved in the down-to-up state transition and up-to-down state transition. Briefly, they photo-induced activity or silencing in interneuron *in vivo* by means of optogenetic tools and they found that interneuronal photo-induced activation terminated up states, while their inhibition prolonged the up state duration. In their work, they also found another interesting evidence: the photo-induced activation of interneurons during down states induced transitions to up states, and they found that actually a weak firing activity of interneurons is needed to maintain the cortical circuitry in a silent state. Thus, looking at the SWA pattern in an animal model for a neurological disease can shed light on the status of excitation/inhibition balance.

Given that the oscillatory regimes present in the brain are intimately associated with neuronal computation, it is not surprising that mouse brain disease are associated to alterations of the underlying oscillators. For their link to the status of the network and in particular to the E/I balance, both gamma oscillations and SWA can be investigated to assess the status of a circuit in pathology, which is what we did in our model of epileptiform activity and also in a Phelan McDermid Syndrome model (Chapter 2).

1.1.4 Epilepsy: an aberrant network phenomenon

As seen in the introduction, the oscillatory regimes of the LFP are strictly correlated to inhibitory neuron activity, and they are strongly affected by the properties of synaptic transmission and by the intrinsic properties of neuronal populations.

Similarly to oscillations, also epilepsy is a network phenomenon. Whereas in physiological oscillatory regimes neurons fire in a controlled way thanks to the E/I feedback, during epileptic seizures the neuronal network is outside this equilibrium and neuronal firing is uncontrolled. Moreover, whereas in physiological oscillations, groups of neurons show orchestrated firing that produces the oscillatory regime, epileptic activity is characterized by a hypersynchronization of the network, which makes the activity lose its content of information. In other words, if all neurons are hypersynchronous and fire all at the same time, there is only little information than can be contained by the neuronal firing pattern, whilst in a "normal" network different groups of neurons would be activated codifying for different internal states, leading to a correspondence between spatial-temporal pattern of activation and the information conveyed (Trevelyan et al. 2013).

During epilepsy, the abnormal neuronal activation can thus be correlated to a landscape of several phenomena: imbalance between excitatory and inhibitory activity, abnormal connectivity, neuronal recruitment, failure of the normal homeostatic mechanisms and changes in intrinsic properties of neurons (Duncan et al. 2006). Even outside the epileptic seizure, the affected brain can show abnormal features and subtle alterations: this is the case of interictal activity.

1.1.5 Interictal activity

While ictal events are defined as the active manifestation of an epileptic condition, interictal activity is the diverse ensemble of abnormal electrophysiological features that can occur between different seizures. Therefore, it can be heterogeneous in nature, is not associated with major neurological or behavioral signs but, nevertheless, is quite different from normal brain activity.

In the broad definition of interictal activity, hypersynchronous interictal spikes (ISs) are quite common features of epileptiform activity with large ensemble of neurons periodically firing hypersynchronous potentials (Noachtar et al. 1999; M de Curtis, Radici, and Forti 1999). This activity is present as slow periodic oscillations of the local field potential. Each interictal event can be identified as a spike of large amplitude. These spikes last for a short time (up to 250 ms) and they are followed by a period of time in which the trace is silent.

Although often critical, seizures may appear only sporadically with no clear leftovers, while interictal activity may lurk in an apparently normal brain even in the absence of any record of past ictal events and without overt neurological symptoms. Since during an IS neuronal firing is hijacked by the pathological rhythm, local computation is obviously altered and ISs can cause cognitive deficits even in absence of seizures (Holmes and Lenck-Santini 2006; Nicolai et al. 2012; Trevelyan et al. 2013; Kleen et al. 2013; Hernan et al. 2014; van Ool et al. 2016). Indeed, studies based on EEG observations concluded that ISs can lead to transitory cognitive effects in humans (Hutt, Newton, and Fairweather 1977; Aarts et al. 1984; Shewmon and Erwin 1988; Krauss et al. 1997; Binnie 2003). For example, driving ability is impaired by ISs since they extend reaction time in simulated driving tests (Krestel et al. 2011), and serious effects of ISs are evident in children where ISs are correlated to attentional deficits and poor scholastic performances (Landi et al. 2019; Lenck-Santini and Scott 2015).

Most studies addressed the impact of ISs on neuronal computation occurring in the epileptogenic region. However, we should also expect that focal ISs can affect brain functions in a more subtle and extensive way, by propagation through long-range connections to areas not directly engaged in epileptiform activity (Schwartzkroin et al. 1975; Sherwin 1982). In fact, coupled EEG and fMRI recordings in human subjects have shown that changes of the BOLD signal are present in remote structures far from the epileptic generator (Kobayashi et al. 2005, 2006).

We studied a mouse model of focal ISs, to understand how focal ISs interfere with neuronal processing of connected areas. Focal IS activity was triggered in the visual cortex of the anesthetized mouse by strictly localized superfusion of the $GABA_A$ antagonist bicuculline (Fisher 1989; Hirase et al. 2004; Meldrum 1971; Collins and Caston 1979; Uva et al. 2005). Local delivery of this drug induced patterns of interictal activity resembling the one appearing in lesional human epilepsy (Chatrian, Shaw, and Leffman 1964) and in idiopathic benign partial epilepsies of childhood (Beaussart 1975; M de Curtis, Manfridi, and Biella 1998). Indeed, bicuculline has been extensively used in studies addressing the mechanisms of IS generation (Schwartz and Bonhoeffer 2001; Schroeder et al. 1990; Ma, Wu, and Wu 2004). By recording *in vivo* LFP and single-cell firing by loose patch-clamp we determined that, even if ISs did not invade the opposite hemisphere, the EEG was subtly disrupted, with a decrease in length and an increase in frequency of up states. By phase-locked averaging of the LFP we found that every IS caused a peculiar change of the firing probability of the contralateral hemisphere during slow-wave activity. Initially the ISs facilitated firing in this area but, after about 100 ms, the cortex was completely silenced for almost 300 ms leading to a precocious termination of the up state. Finally, we determined that visual evoked responses were affected by ISs depending on the temporal relationship between stimulus presentation and contralateral spike burst.

With this data, I could prove that ISs interact with other cortical dynamics far from the epileptic focus, disrupting endogenous oscillatory rhythms and affecting brain information processing. This evidence sustains the notion of an IS-induced cognitive impairment in local and distant areas, an idea that has major clinical implications in the ongoing discussion about the pharmacological treatment of subclinical EEG anomalies (Binnie 2003; Holmes 2013; Beghi et al. 2013), especially in children, where cognitive impairment induced by ISs is more severe (Besag 1995; Bourgeois 2004). Here we studied the effects of acute IS induced in a naïve brain on cortical processing and we determined that brain computation is strongly affected even in absence of the circuitry rearrangements proper of chronic epilepsy.

1.2 Materials and Methods

1.2.1 Mouse preparation

Adult (age > postnatal day 60) C57BL/6 J mice were used (n = 26). Animals were reared in a 12 h light/dark cycle, with food and water available ad libitum. All experimental procedures conformed to the European Communities Council Directive n° 86/609/EEC and were approved by the Italian Ministry of Health.

Mice were anesthetized by intraperitoneal injection of urethane (0.8 ml/hg in 0.9% NaCl; Sigma). Additional doses (10% of initial dose) were intraperitoneally administered to maintain the anesthetic level when necessary. The head was fixed in a stereotaxic frame. Body temperature during the experiments was constantly monitored with a rectal probe and maintained at 37 °C with a heating blanket. The depth of anesthesia was evaluated by monitoring pinch withdrawal reflex and other physical signs (respiratory and heart rate). A portion of the skull overlying the visual cortex (0.0 mm anteroposterior and 2.7 mm lateral to the lambda suture) was drilled on both the hemispheric sides and the *dura mater* was left intact. A double chamber was created with a thin layer of a synthetic resin (Paladur, Heraeus Kulzer GmbH & Co.) around the edges of the craniotomy. Cortex was maintained constantly wet with artificial cerebrospinal fluid (ACSF) solution, composed as follows: NaCl 132.8 mM, KCl 3.1 mM, $CaCl_2$, 2 mM, $MgCl_2$ 1 mM, K_2HPO_4 1 mM, HEPES 10 mM, $NaHCO_3$ 4 mM, glucose 5 mM, ascorbic acid 1 mM, myo-inositol 0.5 mM, pyruvic acid 2 mM, pH = 7.4. In order to induce interictal spikes, the solution inside one chamber was replaced by ~40–60 µL of $GABA_A$ receptor agonist bicuculline methiodide (BMI, 100 µM in ACSF solution; Sigma). The drug superfusion was restricted to a single hemisphere and verified by means of paired local field potentials recordings. BMI was occasionally added in order to keep constant the interictal activity pattern. Animals deeply anesthetized under urethane were sacrificed by cervical dislocation without regaining consciousness at the end of the experiment.

1.2.2 Local field potential and loose-patch recordings

To record local field potentials (LFPs) in the two hemispheres, two glass micropipettes (impedance ~2 MΩ, filled with ACSF solution) were positioned into the visual cortex at a depth of 250–300 µm (layer 2/3) with a motorized micromanipulator (MPI electronic). A common reference Ag-AgCl electrode was placed on the cortical surface.

For the loose-patch recordings, glass micropipettes (4–8 MΩ resistance, filled with ACSF; Sigma) and an axopatch-1D amplifier were used. The pipette was inserted through the *pia* by applying about 300 mbar of positive pressure until layer 2/3 was reached. Cells were searched in voltage-clamp mode with the positive pressure lowered to 30 mbar while monitoring the tip resistance with a square-wave current pulse (test stimulus 20 mV). On approaching a cell, pressure was relieved and light suction was applied. Voltage responses were recorded in current clamp mode (I = 0) with a 10-fold gain.

Electrophysiological signals were amplified 1000-fold (EXT-02F, NPI), band pass filtered (0.1–1000 Hz), and sampled at 10 kHz with 16-bit precision by a National Instruments (NI-usb6251) AD board controlled by custom made LabView software. Line frequency 50 Hz noise was removed by means of a linear noise eliminator (Humbug, Quest Scientific).

1.2.3 Two-photon calcium imaging combined with LFP recordings

Imaging was performed on adult mice (P > 90) obtained by crossing a homozygous B6;Cg-Tg(CaMKIIa-cre)T29-1Stl/J female (Jackson lab, stock number #005359) with a B6;129 S-Gt(ROSA)$^{26Sortm95.1(CAG-GCaMP6f)Hze}$/J homozygous male (Jackson, stock number #024105). In this animal (CaMKII-GCaMP6f) the expression of the genetically encoded Ca^{2+} sensor GCaMP6f was restricted to pyramidal cells. The mouse was head-fixed and a craniotomy of 2–3 mm in diameter was drilled over the visual cortex as for electrophysiological experiments. A perforated glass was glued to the craniotomy in order to facilitate the penetration of drugs after the acquisition of the baseline activity of the brain and to record LFPs. Imaging was performed with a two-photon microscope (Ultima IV, Prairie Technology) equipped with a 18 W laser (Chameleon Ultra 2, Coherent) tuned at 890 nm that delivered about 30 mW at the sample. Images were acquired 200–250 µm below the cortical surface with a water immersion objective (Olympus XLUMPLFLN-W 20X, numerical aperture) at a resolution of 512 x 512 pixels at 10 Hz (spiral scan). The same field was acquired in baseline condition and after administration of BMI 100 µm.

1.2.4 Visual evoked potentials (VEPs)

VEPs in response to alternating checkerboards modulated at different contrasts were recorded at the same depth of LFPs. All visual stimuli were computer-generated on a display (mean luminance at maximum contrast, 3 cd/m2) by a MATLAB custom script that exploits the Psychophysics Toolbox (Brainard 1997; Pelli 1997; Kleiner, Brainard, and Pelli 2007). The luminance of the checkerboard was calibrated by means of a photometer (Konica Minolta). The contrast values were calculated with the Michelson's formula: $(I_{max} - I_{min})/(I_{max} + I_{min})$. Transient VEPs were recorded in response to the reversal (0.5 Hz) of the checkerboard (spatial frequency 0.04 c/deg). The response to a blank stimulus (0% contrast) was also recorded to estimate noise.

1.2.5 Data analysis

Collected data were visually inspected, and traces presenting drift or other artefacts were excluded (~1% of the data). All the subsequent analysis was performed on

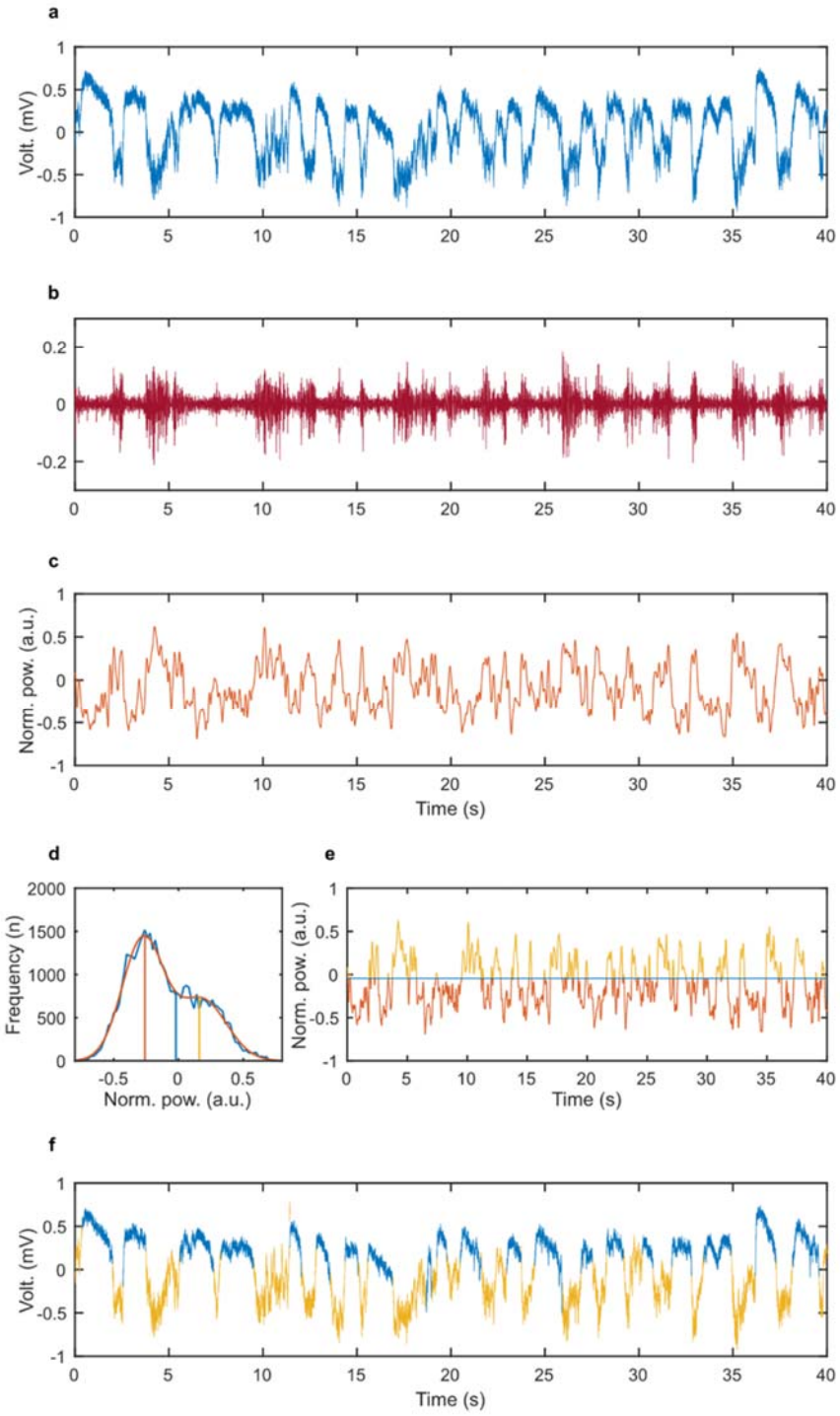

*Figure 1.1. Unbiased detection of up states. (**a**) Recording of a raw LFP during slow-wave oscillation. (**b**) The same signal has been high-pass filtered in the frequencies used for up state detection. (**c**) Gamma-band activity (GBA). Note that peaks in the time series perfectly overlap the up states in the original LFP track. (**d**) Histogram for the log(GBA) values with the double Gaussian fit and the calculated threshold. (**e**) Thresholded GBA. (**f**) Final segmented signal according to the threshold set in d.*

To detect ISs in the LFP signal a threshold was fixed at 3 standard deviations from mean. Peri-IS spectrograms were calculated using MATLAB STFT function with an overlapping Blackman window of 200 ms. Spectrograms were then normalized by the average LFP spectrum far (>2 sec) from IS events.

The recording was high-pass filtered (200 Hz) for the spike detection on loose-patch recordings; a threshold of 3 standard deviations was used to detect spike events. Cell recordings that included less than 100 interictal spikes were excluded from subsequent analysis.

VEP amplitudes were calculated as the mean voltage in a window of 400 ms starting from 100 ms after stimulus presentation. The temporal distribution of amplitude values was smoothed with a Gaussian kernel of 100 ms to generate the temporal evolution of VEP amplitudes reported in Figure 1.12 b; two animals were excluded because of the low number of events.

1.3 Results

1.3.1 Slow-wave oscillations are synchronized between hemispheres

We first analyzed how the primary visual cortex (V1) behaved in the urethane anesthetized mice in resting state. In these recordings, no visual stimulation was performed. The mice showed the typical slow-wave activity that is normally observed during non-REM sleep and resting wakefulness (Figure 1.2). During slow-wave activity, we could observe oscillations between up and down states. The up states showed a negative potential of 0.8 mV in extracellular recording configuration.

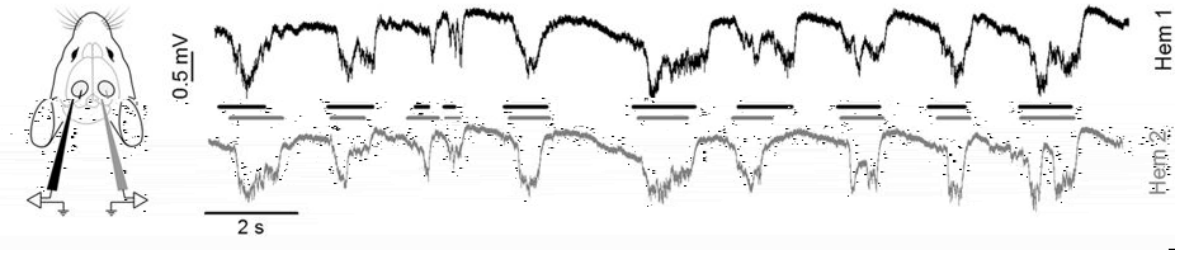

Figure 1.2. Examples of baseline activity in the urethane anesthetized mouse in the two hemispheres (black line: Hem 1, gray line: Hem 2).

Different parameters that characterized the up and down states were analyzed. The duration of the up states ranged between 0.45 and 0.75 s and the frequency ranged between 0.55 and 0.95 Hz. When the extracellular potential was recorded in both hemispheres, the up states appeared to be synchronized, as has already been reported (Contreras and Steriade 1995; Mohajerani et al. 2010).

To quantify this synchronization, the delay between an up state in hemisphere 1 (Hem 1) and the closest up state in hemisphere 2 (Hem 2) was calculated. Then we computed the distribution of the time lag between the nearest neighbor (NN), which showed a peaked distribution around 0 s (Figure 1.3 b, black line). To test whether the NN distribution supports the up states synchronization between the two hemispheres, we generated a shuffled sequence of up and down states in one hemisphere and computed the NN distribution of the shuffled data. Then we compared the original and shuffled NN distribution and found a significant difference (KS test, $p<0.001$ for each animal), thus proving that oscillations are coupled (Figure 1.3, b). Since the distributions were also symmetrical, we could conclude that there was no dominant hemisphere in the generation of slow wave oscillations.

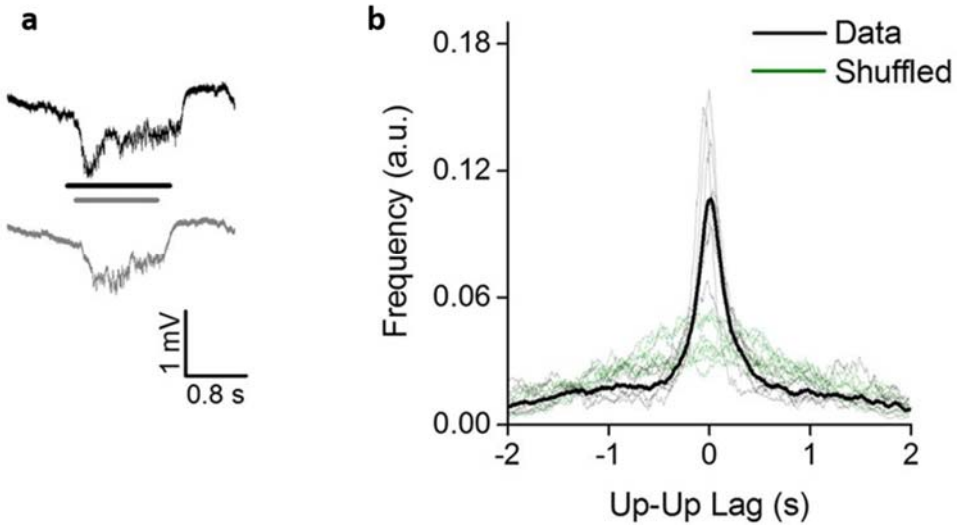

*Figure 1.3. (**a**) Magnification of a single up state recorded simultaneously in both hemispheres. (**b**) The distribution of lag times between the middle point of up states in the two hemispheres (dashed lines: single animals; continuous line: average), compared to the distributions obtained after randomly shuffling up states sequence in Hem 2 (green traces). The shuffling returns a far more dispersed distribution indicating the correlation between the two hemispheres.*

1.3.2 ISs cause the fragmentation of up states in the opposite hemisphere

After the resting state analysis, the brain activity was altered by superfusion of 100 µM bicuculline methiodide (BMI) to the visual cortex of Hem 2, while the extracellular potential was recorded from both Hem 1 and 2. Within a few minutes from the administration of bicuculline, interictal spikes appeared, only in Hem 1, with their characteristic stereotyped shape of sharp deflections of 2-6 mV.

During the interictal spikes, most of the neurons of the affected area underwent a fast and transient activation, as demonstrated by two-photon intravital calcium imaging (Figure 1.4 and Figure 1.5) and also by loose-patch clamp recording (Figure 1.6).

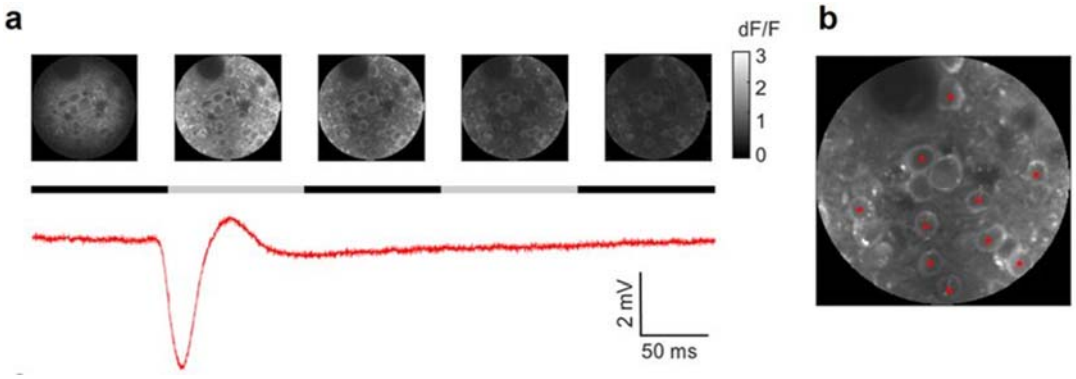

*Figure 1.4. (**a**) Sample images obtained during in vivo two-photon imaging in the visual cortex of a CaMKII-GCaMP6f mouse. The time lapse sequence is over imposed to the simultaneous recording of the extracellular potential and shows that ISs are accompanied by a calcium transient that occurs simultaneously in all neurons in the field. The horizontal black and gray bars show the sampling period for each frame. (**b**) Sample ΔF/F traces measured for neurons (red asterisks) in the field.*

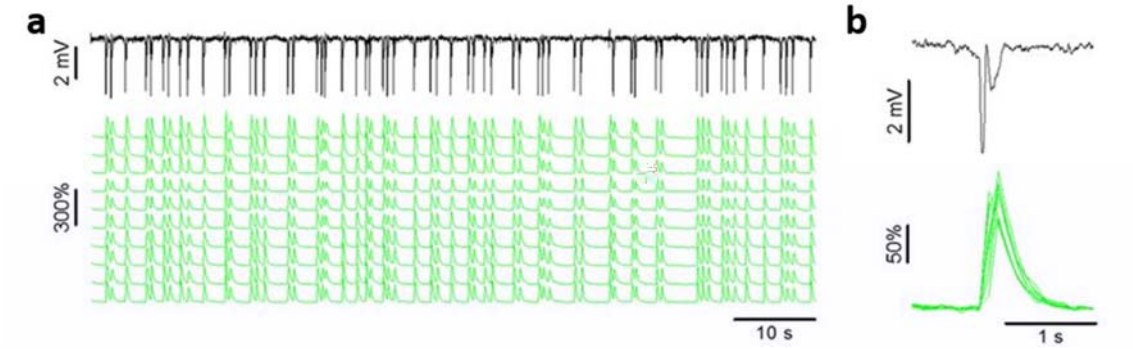

*Figure 1.5. (**a**) The LFP is aligned to the calcium responses. The inset (**b**) shows the stereotyped Ca^{2+} transients recorded during a single IS.*

Loose-patch cell recordings showed a very narrow temporal window of about 50 ms during the IS in which neurons could fire. Interestingly, most of the cells produced a very small number of action potentials for each IS, a median of 2.6 action potentials per interictal spike (Q_1 = 1.9, Q_2 = 4.0, n=9 cells from 6 mice).

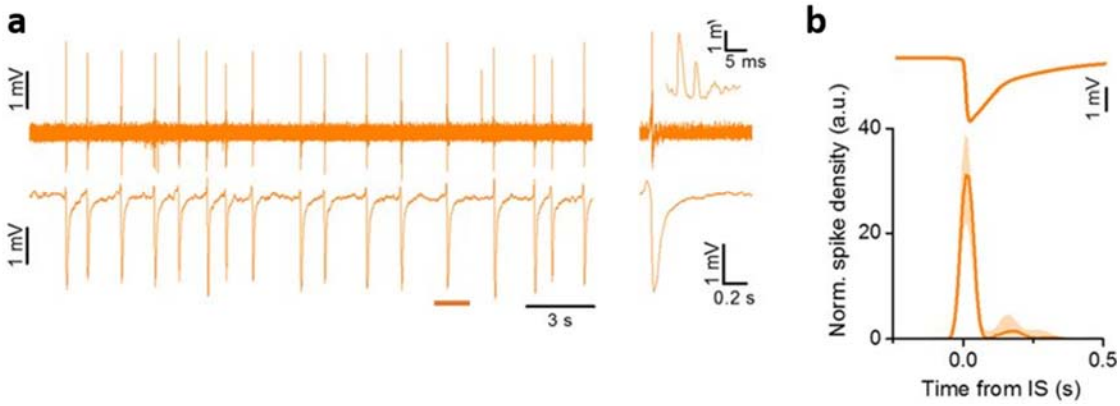

*Figure 1.6. (**a**) Sample loose-patch recording from a L2/3 neuron during interictal activity (upper trace) and the simultaneous LFP recording from a nearby extracellular electrode. The inset shows the neuronal firing during a single IS event, with an enlargement around the IS onset. (**b**) Spike density mediated on all recorded neurons aligned to the ISs after normalization with mean firing frequency (median +/− quartiles, n = 9 cells from 6 mice). The vast majority of action potentials are fired within a 100 ms wide interval centered on the IS (horizontal bar).*

The interval between two consecutive interictal spikes was found to be normally distributed (Lilliefors normality test, p<0.001). The median interval duration was 2.6 s (frequency 0.38 Hz). The interictal activity was also investigated in relationship with slow-wave activity of the contralateral hemisphere, where the interictal spikes were not present (Figure 1.7).

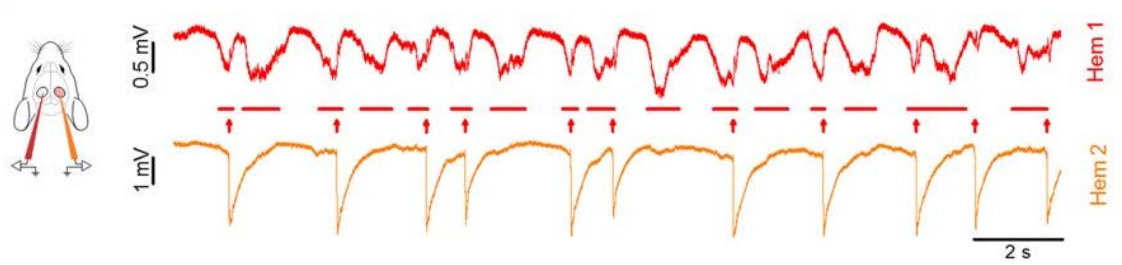

Figure 1.7. Traces showing activity in Hem 1 when in Hem 2 focal ISs are induced by localized application of BMI 100 µM.

During an interictal spike, there was a transient interruption of the ongoing up state. The presence of the interictal spikes in Hem 2 changed the statistics of the up states in Hem 1. In particular, frequency of the up states was increased from 0.57 to 0.64 Hz. The up state duration decreased from 0.74 s to 0.64 s

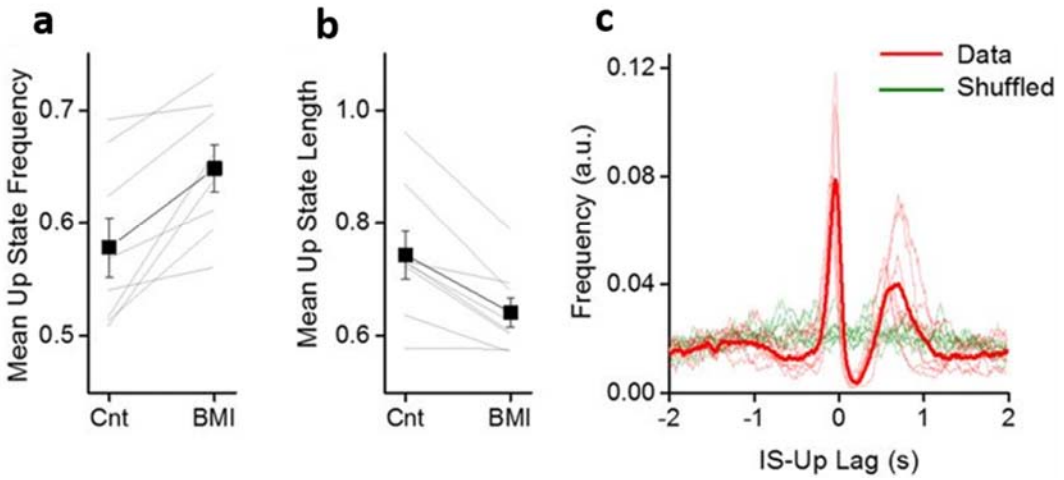

(

Figure 1.8).

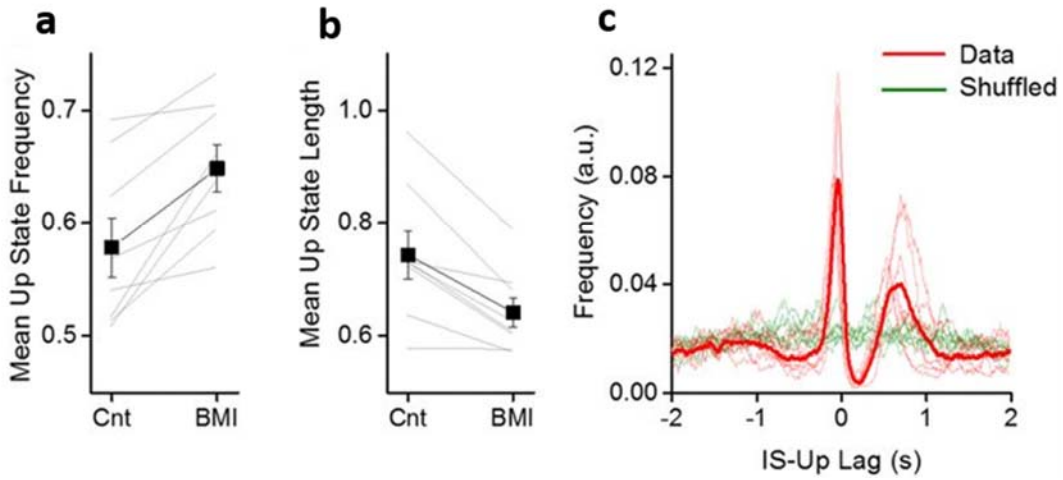

*Figure 1.8. (**a**) The mean frequency of up states is increased after BMI in Hem 2. The thin lines indicates the change in mean frequency in the same mouse before and during the BMI treatment (CTRL, 0.57 ± 0.03 vs. BMI, 0.64 ± 0.02, paired t-test, n = 8, p = 0.004). (**b**) The duration of up states is shortened by ISs in Hem2 (CTRL, 0.74 ± 0.04 vs. BMI, 0.64 ± 0.03, paired t-test, n = 8, P = 0.003). (**c**) Distributions of lag times between the middle point of up states in Hem 1 and the onsets of IS events (dashed lines: single animals; continuous line: average). The double peak in the distribution shows that the ISs follow the up states with a small jitter evidenced by the small dispersion of the first left peak. The broader peak on the right is due to the reappearance of the up state that follows the IS with a more variable duration, as evidenced by the broader distribution. Notice that ISs are never over imposed to up states.*

These data suggest an interesting interaction between up states and ISs: the onset of an up state caused an IS, which in turn, fragmented the up state in the contralateral cortex. To verify this hypothesis, we computed the distribution of the time lag between each IS and the middle point of the nearest up state in Hem 1

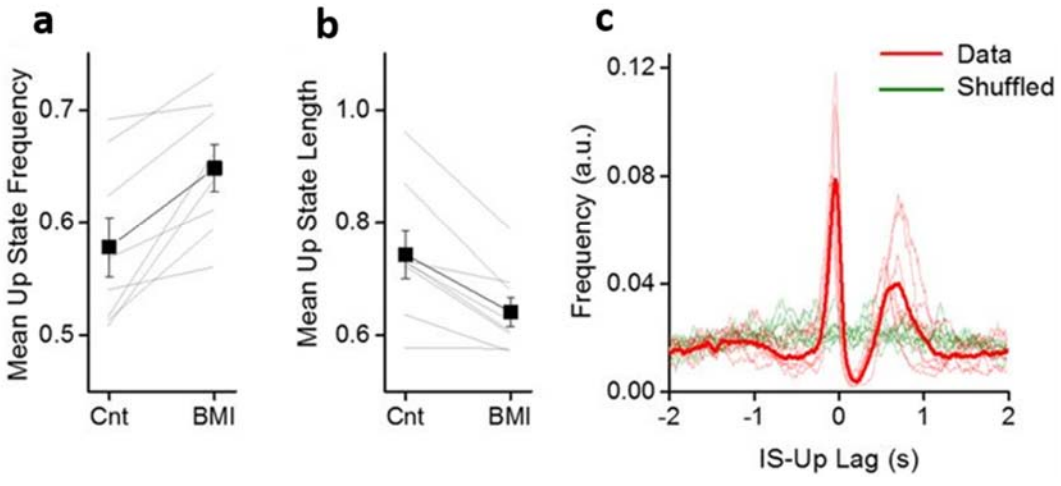

(Figure 1.8, c). The lag distribution showed a peculiar double peak and a strong decrement in correspondence of the zero-lag point. This suggests that the majority of ISs occurred immediately after the onset of an up state and that the ISs in Hem 2 caused the interruption of the up state in Hem 1. The random temporal shuffling of the up state sequence led to completely different distributions of lags (green lines in

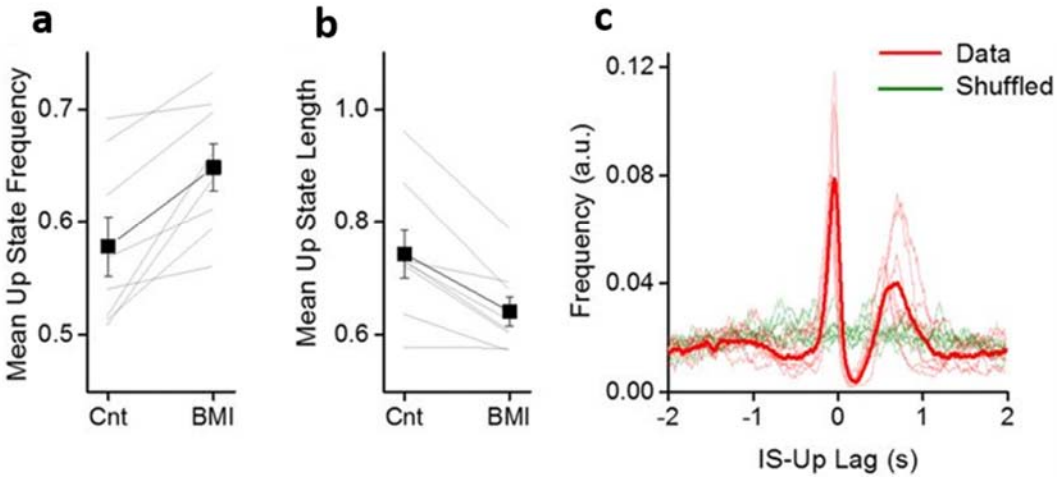

Figure 1.8, c), demonstrating the correlation between the two processes.

To analyze further this relationship, we divided the LFP recorded in Hem 1 in short segments centered on the onset of each IS. The raster plots in Figure 1.9 represent the cropped LFP recorded from the two hemispheres of one representative mouse. The interruption of the up states in Hem 1 following the IS in Hem 2 was a consistent phenomenon (see red bar in Figure 1.9 b), as it occurred in every fragment. The average field shown above the raster plot clearly reports the temporal dynamic of the interplay between up states and ISs: each IS was preceded by an up state onset, and in turn caused a brief, transient interruption of the up state. On average, the lag between the up state and the following IS was about 200 ms and the up state interruption caused by the IS lasted for about 300 ms. A characteristic small deflection of the LFP was observed in Hem 1 in correspondence to the IS.

Figure 1.9. (

Figure 1.10 reports the mean of the IS-locked LFPs of every recorded animal (thin lines) and the population mean.

We analyzed the LFP segments in the frequency domain by computing the average spectrogram of the LFP segments (Figure 1.10, a). The up state interruption was clearly visible as a reduction in all frequencies up to 100 Hz (red bar), and in correspondence of the interictal peak there was a sharp increase in the power of all frequencies. We supposed that at this time Hem 1 was receiving a transient excitatory stimulation from the contralateral cortex, with an increased probability of neuronal firing.

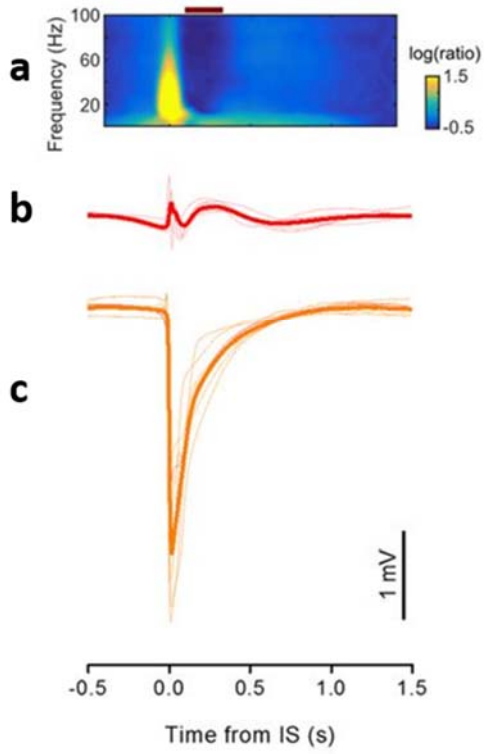

*Figure 1.10. Mean traces of up state waveforms in Hem 1 phase-locked with the beginning of ISs in Hem 2. Data recorded in 8 mice (dashed lines) and their average (continuous line). The silencing period is always present. (**a**) The average spectrogram of the LFP segments in Hem 1, phase-locked on the IS. The window of reduced activity is clearly associated with a strong reduction in the spectral power (horizontal red bar). (**b**) The average LFP trace in hemisphere 1, corresponding to the spectrogram shown in (a). (**c**) The average LFP trace in hem 2, showing the average IS.*

1.3.3 ISs alter the neuronal firing probability in the contralateral hemisphere

In order to verify that contralateral ISs changed neuronal firing probability, we performed loose-patch recordings of neurons in Hem 1 (Figure 1.11).

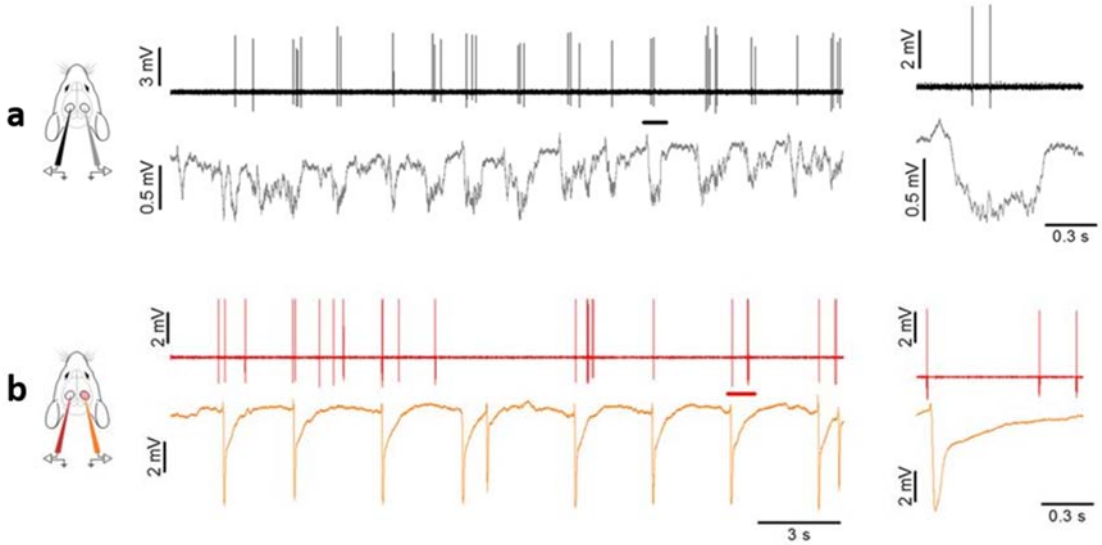

*Figure 1.11. (**a**) Loose-patch recording from one neuron in Hem 1 (upper black line) and contralateral LFP in Hem 2 (lower gray line) displaying sparse firing during slow oscillations. Insert shows a magnification of firing activity during a single up state (black bar). (**b**) The same neuron has been recorded (upper red line) during focal IS activity (LFP, orange trace) caused by focal superfusion with BMI in Hem 2. The inset shows a magnification of a single IS.*

Before superfusion of bicuculline each neuron fired up to a few action potentials only during each up state (Figure 1.11, a). When bicuculline was added in Hem 2 (Figure 1.11, b), we observed a biphasic effect on the firing probability in Hem 1 (Figure 1.12, a, b). Interestingly, the temporal pattern of the firing density is perfectly mirrored by the temporal evolution of the gamma band power (Figure 1.12, b (blue trace). In correspondence with the IS peak, the firing probability was briefly boosted and this facilitation was immediately followed by a window of decreased firing of about 0.3 s, which overlapped perfectly with the silencing observed in the field recordings. Between 0.3 and 0.8 s after the IS, the firing rate incremented again, following the reappearance of the up state observable in the field potential (Figure 1.12, c). These data showed that contralateral ISs modified the temporal pattern of spontaneous discharges in the control hemisphere. This happened without a large increase in the overall number of spikes (CTRL: median 1.72 spikes/s, n = 28 neurons from 12 mice; BMI: 2.00 spikes/s, n = 20 neurons from 6 mice; KS-test: p = 0.1). In conclusion, ISs strongly modulated the density of firing probability in a brief time window, thus suggesting a transient alteration of cortical computation and, presumably, of the processing of visual stimuli.

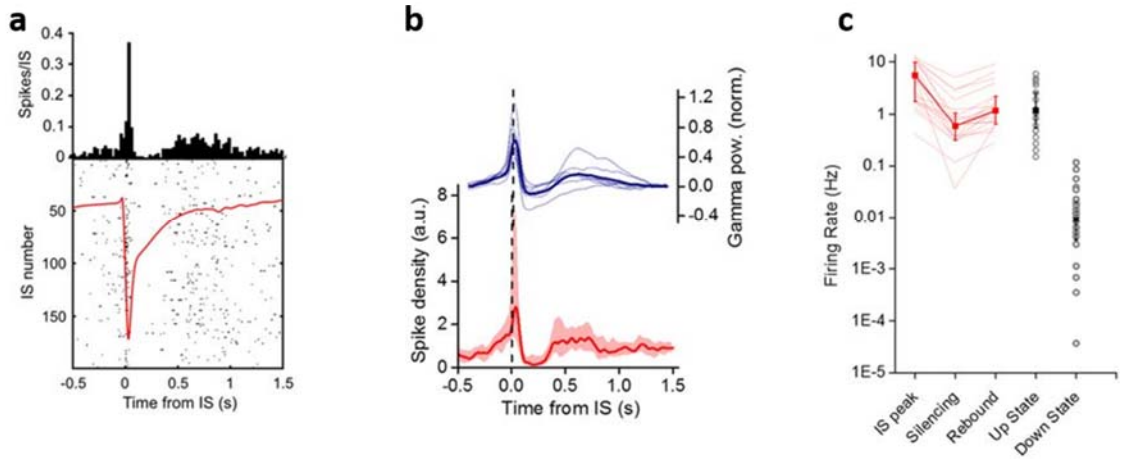

*Figure 1.12. (**a**) Peri-IS raster plot showing spike pattern during 200 different ISs. The upper diagram is the spike distribution computed from the raster plot. The distribution has a sharp peak centered on the peak of the contralateral IS (red trace) that is followed by a period of reduced firing. (**b**) The red trace is the median distribution of firing for all the recorded cells in Hem 1 phase-locked to the ISs occurring in Hem 2 (median +/− quartiles, n = 20 from 6 animals). The blue trace represent the power in the gamma band (40–100 Hz) of the LFP in Hem 1 (n = 7 mice; thick line: mean, thin lines: single experiments). (**c**) Firing rates in different stages during contralateral ISs. The firing rate during rebound is extremely close to the firing rate during the up state (rebound: 1.18 spikes/s, n = 20 neurons from 6 mice; up state: 1.19 spikes/s, n = 28 neurons from 14 mice; p = 0.81, KS test).*

1.3.4 Contralateral interictal spikes interfere with visual processing in the non-treated hemisphere

We evaluated the processing of visual stimuli by recording the visual evoked potentials (VEPs) in V1, in response to the periodic reversal of a checkerboard (2 s period; Figure 1.13).

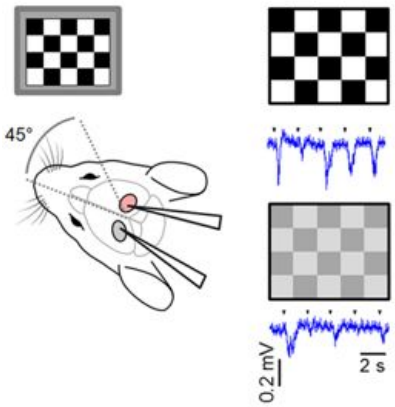

Figure 1.13. Schematic of the experimental setup and exemplificative traces at two different contrasts. For each reversal of the checkerboard (small dot above the trace), there is a response in the LFP recording. The amplitude of responses is proportional to the intensity of the stimulation.

The probability distribution of the timing of the ISs relative to the checkerboard reversal clearly demonstrated that visual stimuli did not influence IS statistics (upper panel of Figure 1.14 a). To evaluate the effects of ISs on sensory responses, we sorted the records containing the VEPs according to the distance of the stimulus onset from the nearest IS occurring in Hem 2. A raster plot of the records from one single animal is depicted in Figure 1.14 c. The checkerboard reverses at 0 s and the VEPs are represented by the vertical blue band that appears with a latency of about 150 ms from the stimulus onset; the dotted line marks the timing of ISs. As exemplified in this plot, ISs had an effect on the VEPs depending on their relative timing: ISs falling shortly before the stimulation caused an increment in the recorded potential compared to the VEPs recorded in baseline conditions, while ISs occurring immediately after the stimulation suppressed the evoked potential (see Figure 1.14).

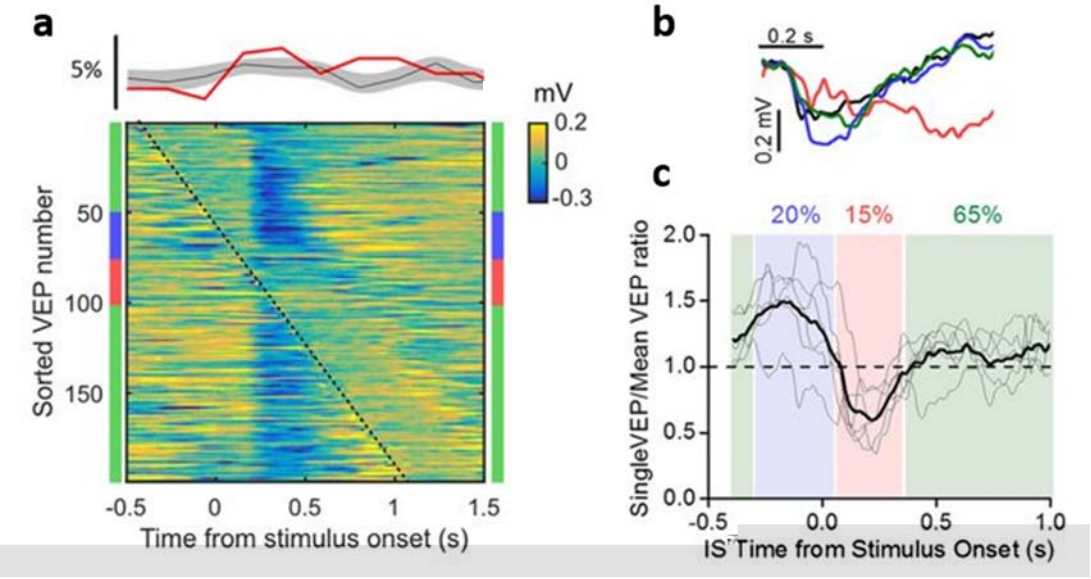

*Figure 1.14. (**a**) The upper panel shows the probability distribution of IS onset in respect of the stimulus (red trace: lower panel experiment; gray area: mean +/− SD for n = 8 animals). The lower panel shows the raster plot obtained by sorting VEP traces according to the delay between stimulus and IS. The dotted black line represents the appearance of IS; time 0 indicates the stimulus presentation. (**b**) Black trace reports a single response to a stimulus presentation in the control recording (before of BMI superfusion). The blue and red traces report the responses when IS immediately preceded (−0.35 to 0.05 s, blue) or followed (0.05 to 0.35 s, red) stimulus presentation. In green there are the mean traces obtained when the stimulus and the closest IS were farther away than 0.35 s. These windows are indicated by the colored bars adjacent to the raster plot in b. (**c**) VEP amplitudes depend on the lag between stimulus and contralateral ISs (N = 6 mice; average in thick line, each mouse in thin lines). The colored shaded zones span the time windows used for the averaging in c. The percentages report the fraction of stimuli falling in the three conditions averaged on all mice.*

We quantified this effect by calculating the VEP amplitude in response to a high contrast checkerboard as a function of the temporal distance between the IS and the stimulus presentation (Figure 1.14, c). In every experiment we observed an enhancement of the response (blue band) followed by a strong suppression (red band). When the distance between reversal and the closest IS was larger than about 350 ms, the response was similar to the response measured before BMI superfusion (green bands). These temporal windows are reported in Figure 1.15 c together with the effect of ISs on the firing rate (replotted from Figure 1.12 b). The firing increase caused by ISs, masked the external stimulus, interrupting the ongoing VEP and causing a brief window of functional blindness. On the other side, the following silencing appeared to increase the sensitivity of the cortex to the visual stimulus. A similar behavior has been observed for sensory stimulations elicited during the down state, especially for high-intensity stimuli (Reig et al. 2015; Sela et al. 2016),

strengthening the idea that during this time window the contralateral cortex switched to a down state.

To assess the ability of V1 of extrapolating significant features of visual stimuli in presence of contralateral IS activity, we measured the contrast response by recording the evoked potentials in response to checkerboards of variable contrast (Porciatti, Pizzorusso, and Maffei 1999). We divided the recordings in three groups, according to the interval between the stimulus and the closest IS. The first group was represented by records in which the stimulus was farther away from any IS than 350 ms (green zone in Figure 1.14 c and Figure 1.15 a). The second group (blue zone) included records in which the IS immediately preceded (−0.35 to 0.05 s) the sǝmulus. Finally, the third group (red zone) included records in which the IS followed (0.05 to 0.35 s) stimulus presentation.

The contrast response curves in the three conditions are shown in Figure 1.15 b and were calculated by measuring the integral of the VEPs in a window of 0.4 s from their onset (0.1 s after stimulus presentation). As it can be seen in Figure 1.15 c, occurrence of an IS before or after the presentation of a visual stimulus significantly altered the detection of different contrasts. In our experimental conditions, visual processing was disrupted intermittently for about 35% of the time (Figure 1.14 c). These data demonstrated that each focal IS transiently influenced signal processing in wide cortical territories following a complex biphasic modality dependent on the relative timing between IS and stimulus in homotypic regions of different hemispheres.

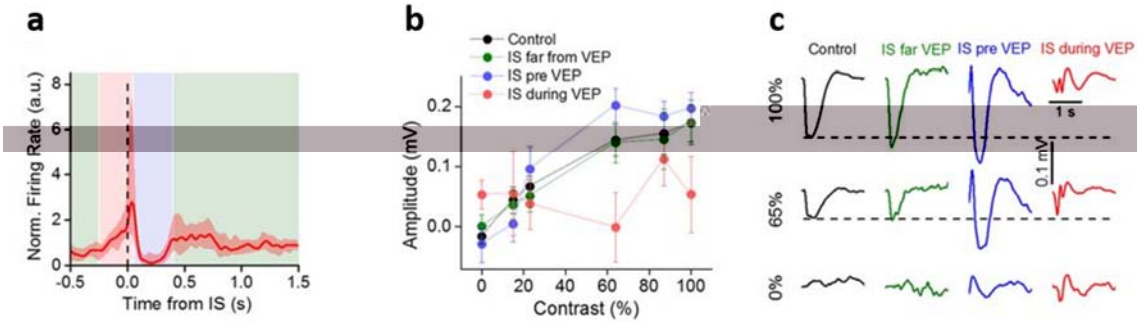

*Figure 1.15. (**a**) Periods of VEP alteration have been superimposed on the peri-IS spike histogram of Figure 1.12 center with the same color code in Figure 1.14 (bottom right), to show the relationship between the effect of ISs on neuronal firing and VEP alteration. (**b**) Contrast response for the three groups of responses compared to control (n = 8 mice). Curves from the VEPs falling after the ISs (IS pre VEP) and for the VEPs interrupted by the ISs (IS during VEP) showed a significant difference, while curve from the VEPs far from the ISs was no significantly different from control (t-test, p-value > 0.05). (**c**) Mean VEP waveforms recorded in the same mouse at different contrasts for the different conditions reported in center panel.*

1.4 Discussion

Epilepsy is a multiform pathology with variable etiology and clinical development (Marco de Curtis, Jefferys, and Avoli 2012). Consequently, it is difficult to reproduce it in the experimental context: although there are several transgenic or pharmacological models for most part of diagnosed forms of epilepsy, many types of diseases remains still to be investigated. Aim of our study is to investigate how an abnormal acute activity induced in a previously normal brain affects information processing in cortical areas far from the epileptiform focus in the anesthetized animal.

It is known that epilepsy produces cognitive impairment at different levels according the magnitude and frequency of seizures and the areas involved; these deficits are usually temporary, but their severity correlates with developmental onset time (Elger, Helmstaedter, and Kurthen 2004), being more severe in children. Interestingly, it has been seen that chronic interictal activity in children can be comparable to epilepsy with seizures in terms of cognitive deficits, even if its effects can be less pronounced in number of areas involved and in extension (Nicolai et al. 2012).

With our work, we found two different mechanisms that can affect cortical function in areas connected to foci of epileptiform activity. Firstly, ISs interact with slow-wave activity, fragmenting up states and potentially interfering with their role on the homeostasis of cortical circuitry. Secondly, ISs interfere with cortical computation by introducing an external non-physiological modulation of neuronal excitability in correspondence of every contralateral IS.

Cortical slow-wave oscillations are critical for memory consolidation and brain homeostasis (Vyazovskiy and Harris 2013; Tononi and Cirelli 2014) and alterations of this rhythm potentially lead to long-term cognitive dysfunctions. Our data suggest that the same cellular mechanism causing the up state onset in Hem 1, triggers an IS in Hem 2 after a brief and variable lag. Thus, slow-wave activity promotes ISs, as also demonstrated in human patients (Frauscher et al. 2015). In turn, ISs close prematurely the up state, forcing the cortex in a brief down state, thus fragmenting the slow-wave cycle. Recently, a similar alteration has been found in a chronic rat model of hippocampal interictal epileptiform discharges, suggesting the generality of this mechanism (Gelinas et al. 2016). There is also clinical evidence pointing toward the importance of a disruption of the sleep slow oscillation in the emergence of pathological conditions. For example, in children affected by Landau-Kleffner syndrome (Irwin et al. 2001; Hughes 2011; Deonna 1991), a form of partial epilepsy with continuous spikes and waves during sleep (>85% of time), there is regression of cognitive function, long-standing developmental delay and loss of acquired language skills that are irreversible after two years from appearance of symptoms. In this disease, the putative role of horizontal connectivity is supported by the ameliorative effects of intracortical resection (Morrell, Whisler, and Bleck 1989; Cross and Neville 2009).

The second question we address in our study regards the impact of epileptiform activity on interconnected regions of the brain not directly involving the focus. Although early reports have already shown that neurons in the contralateral cortex may display altered activity after the induction of an interictal focus (Schwartzkroin et al. 1975; Sherwin 1982), the relationship of this alteration with up and down states as well as its effects on visual processing are still unknown.

These experiments evidence a biphasic effect of ISs on contralateral activity: after a brief time period of increased firing in correspondence with the IS a window of strongly reduced firing appear. The effects on the responses to visual stimuli mirror this dual effect of ISs on spontaneous firing. Indeed, the subdivision of VEPs according to their temporal connection with ISs demonstrate that ISs can enhance or suppress visual responses depending on their temporal relation with the stimulus. Given the average frequency of ISs in our model, the visual cortex operates in an altered state for about 35% of time. This would be hardly compatible with a proper control of visually driven behavior. Indeed, several papers have shown that electrophysiological estimations of visual properties correlate with

behavioral analysis (Ridder and Nusinowitz 2006; Pizzorusso et al. 2006; Sale et al. 2007; Guzzetta et al. 2009; Baroncelli et al. 2012). However, further studies could be done to better investigate perception in these epileptiform mice in future.

Furthermore, if interictal spike activity is generated in one associative area, its propagation to the contralateral side may affect both local associative functions and possibly, related sensory perception. Conversely, propagation of interictal events into primary sensory cortices might be responsible of sporadic neglect or alteration of bottom-up sensory coding. These phenomena might be triggered by focal epileptiform activity localized millimeters away from the control region, leading to a revision of the concept of "focal activity" and possibly promoting a more brain-wide approach to epilepsy treatment.

Chapter 2: : Gain adaptation disruption in an autism-related model

Paper under preparation for publication

2.1 Introduction

2.1.1 Phelan McDermid Syndrome

Phelan McDermid syndrome (PMS) is a rare genetic condition with at least 600 cases reported worldwide but, due to diagnostic difficulties, it is almost certainly heavily underdiagnosed. The molecular underpinning of the disease is a deletion localized at the long arm of chromosome 22, near the telomeric region (22q13.3). These clinical manifestations include hypotonia, global developmental delay and intellectual disabilities, together with absent or severely delayed speech and several autistic spectrum signs.

The first report of a 22q13 deletion causing PMS occurred in 1985 (Watt et al. 1985) and, after that, a series of follow up studies refined the critical region causing the disease, including a series of reports in which small deletions affecting only the gene SHANK3 were found to be sufficient to induce the syndrome (Costales and Kolevzon 2015). These reports strongly suggested a critical role for SHANK3 gene in causing PMS and could also explain the large heterogeneity found in PMS patients: this is probably caused by the existence of several Shank3 isoforms thus opening the possibility that different isoforms might be differentially affected by the mutation.

2.1.2 Shank3

The SHANK3 gene is composed of 22 exons and its product includes several domains that are functional to the protein role, as it will be clear soon. Shank3 protein is expressed throughout the whole brain and, at a subcellular level, is localized in excitatory neuronal synapses (Heise et al. 2016), where it acts as a postsynaptic scaffolding protein, critical for excitatory synaptic transmission. As a scaffold, its role is to interact with several proteins composing the postsynaptic element and to keep them close by, so that they can participate correctly to synaptic functions. Some of the proteins Shank3 interacts with are N-methyl-D-aspartate receptor (NMDA-R) via the post-synaptic density-95 (PSD-95)/guanylate kinase-associated protein (GKAP) complex and the metabotropic glutamate receptor (mGluR) via Homer (Uchino and Waga 2013). These interactions explain the existence of several domains inside Shank3: they are needed to bind different proteins composing the postsynaptic density (PSD), which is vital to keep receptors and signaling complexes close to the area where the neurotransmitter is released and to intracellular effectors (Figure 2.1).

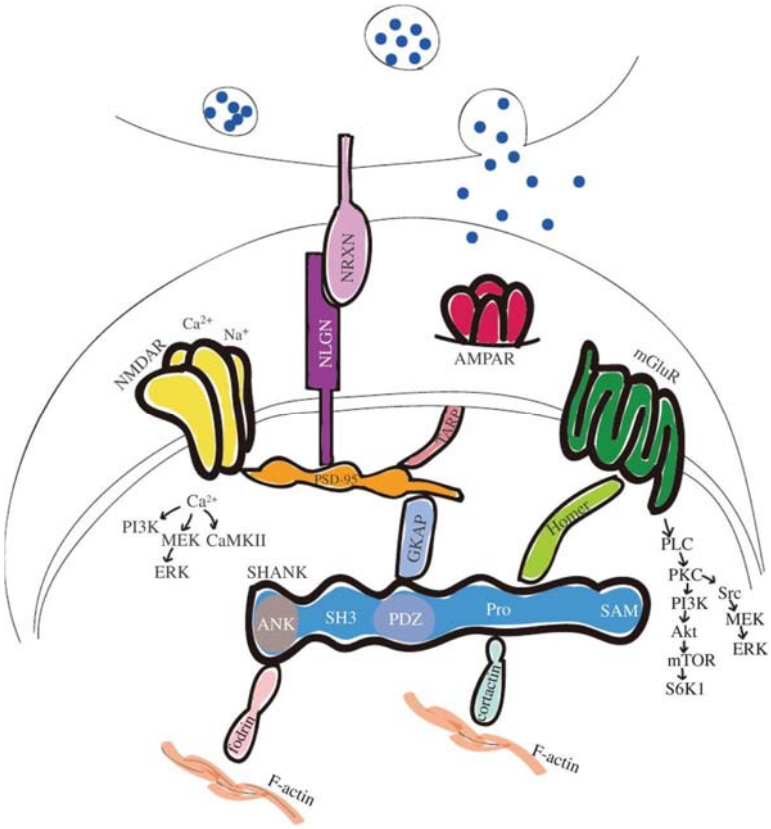

Figure 2.1. Different domains of Shank3 interact with different proteins to maintain the PSD proteins close together (Yoo et al. 2014). *mGluR: metabotropic glutamate receptor; AMPAR, NMDAR: the two main ionotropic glutamate receptors; PSD-95, Homer: main components of the post-synaptic density.*

An example of the importance of the role of Shank3 in the postsynaptic density is its interaction with the metabotropic glutamate receptor 5 (mGluR5). In this interaction, Shank3 has a critical role, because by interacting with the protein Homer it binds to both the mGluR5 receptor present on the cell membrane of the postsynaptic density and to the downstream effector inositol trisphosphate receptor (IP_3R) on the endoplasmic reticulum membrane. When glutamate binds to the mGluR5 receptor it activates the coupled protein G_q which in turn activates phospholipase C (PLC) that initiates the production of inositol trisphosphate (IP_3). IP_3 is a cytosolic second messenger that binds to IP_3R on endoplasmic reticulum and can induce a myriad of cell responses through the release of Ca^{2+} from the endoplasmic reticulum stores. All these cascade signals are potentiated when all the involved parts are spatially clustered together (Figure 2.2) and, indeed, the loss of Shank3 impairs mGluR5 signaling (Verpelli et al. 2011; Piers et al. 2012). In fact, in mouse models of the disease, some mGluR5 positive allosteric modulators like 3-cyano-N-(1,3-diphenyl-1H-pyrazol-5-yl)benzamide (CDPPB) and VU0409551 have been tested and have reverted the phenotype.

This mGluR-mediated calcium release from intracellular stores is important for late phases of LTP and for controlling local protein translation (Mukherjee and Manahan-Vaughan 2013).

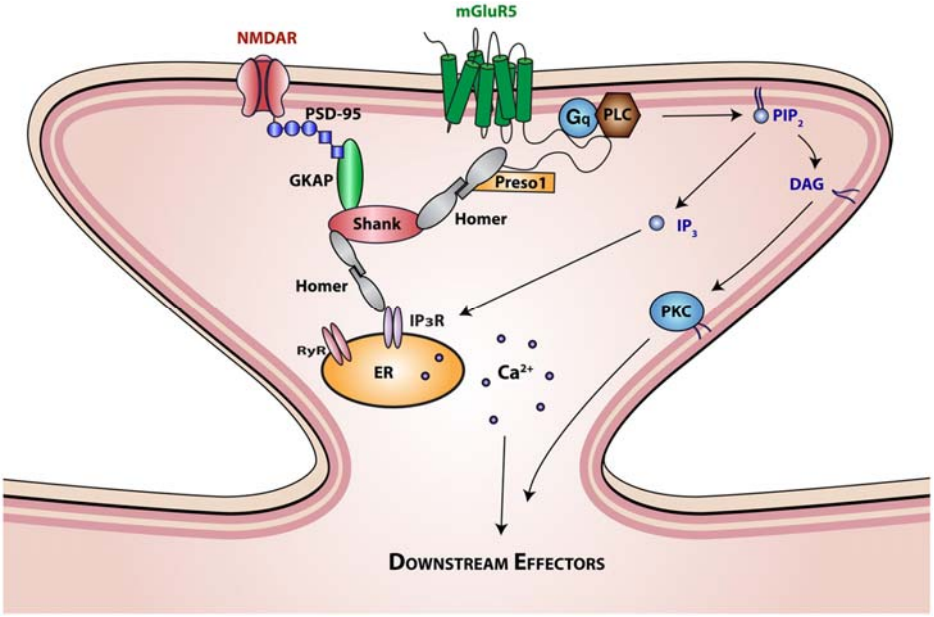

Figure 2.2. Shank3 is critical for keeping mGluR5 close to proteins involved in its signaling pathway, like IP_3R. When mGluR5 is activated, IP_3 is produced and binds to IP_3R on endoplasmic reticulum, causing Ca^{2+} release from the intracellular stores. Ca^{2+} release is potentiated through calcium-induced calcium release (CICR), thanks to the activation of the ryanodine receptors (RyR) (Piers et al. 2012).

2.1.3 Mouse models of PMS

As stated previously, Shank3 protein is composed of different domains, which mediate its interaction with other synaptic proteins. The domains are, from N-terminal to C-terminal:

- 5/6 ankyrin repeated domains, which provide contacts with the actin cytoskeleton mediated by α-fodrin.
- A Src homology-3 (SH3) domain, that allows the anchoring of AMPA receptors to the post-synaptic density (PSD) through the glutamate receptor-interacting protein GRIP.
- A PSD-85-Discs Large-zona occludens-1 (PDZ) domain, which indirectly mediates the contact between Shank and PSD-95 and then to NMDA receptors.
- A prolin-rich region which provides the binding with members of the Homer family.
- A sterile alpha motif (SAM) at the C-terminal, which mediates Shank multimerization and Zn^{2+} sensitivity in Shank2 and Shank3 isoforms.

Apart from the full-length protein, Shank3 variants of different exon constitution can be found and are missing some of the domains of the full-length protein (summarized in Figure 2.3). The expression of the different isoforms is variable in its spatial distribution in the brain, and can be also specific of a certain cell type or a certain developmental stage (X. Wang et al. 2014).

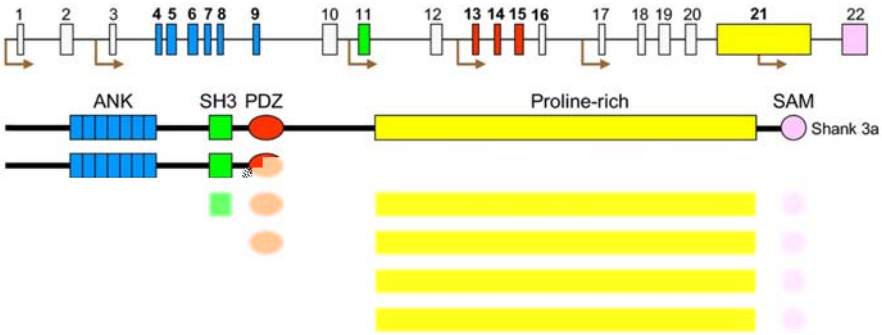

Figure 2.3. Main protein isoforms generated by putative alternative promoters (indicated by the brown arrows) and alternative splicing (not indicated) (Sala et al. 2015).

Because of the existence of these different isoforms of Shank3 protein, different mutations of SHANK3 gene can affect differently different Shank3 isoforms. A few mouse models have been generated, carrying different mutations and causing different impairments, namely Shank3Δ4-7, Shank3Δ4-9, Shank3Δ11, Shank3Δ13-16 and Shank3Δ3-21, even though a mouse that lacks all isoforms of Shank3 has not been produced yet.

In our experiments, we used the Shank3Δ11$^{-/-}$ model, that was produced and published by (Schmeisser et al. 2012), which has a deletion of exon 11 that produces a frameshift mutation with the formation of a stop codon site right after the deletion site. This mutation prevents the expression of isoforms a and b and the effect on the behavior of the mouse has been characterized accurately. The most important alterations are increased self-grooming and aggressiveness, higher sensitivity to pain, reduced social interaction and cognitive rigidity (Schmeisser et al. 2012; Vicidomini et al. 2017).

The Shank3Δ11$^{-/-}$ model has also been quantified by a molecular point of view by the group of Carlo Sala and Chiara Verpelli and they found a reduction of mGluR5 and Homer1b/c protein was found in the PSD fraction of brain samples, together with a reduction in their colocalization in the striatum and somatosensory cortex. Even if in human PMS epilepsy is present in about 25% of patients (Sarasua et al. 2014), Shank3Δ11$^{-/-}$ model does not show any spontaneous epileptic activity, but could have more subtle alterations that are less easy to spot. We hypothesized that we could have detected hints of hyperexcitability in the visual system that, as we discussed previously, is finally tuned by the excitation/inhibition balance.

Before describing our experimental data, I would like to introduce the theoretical foundation of the electrophysiological experiments we designed. The tools we decided to use to investigate the status of excitation/inhibition balance in this mouse model are 1) the analysis of the steady state activity of the visual cortex during anesthesia-induced slow-wave sleep and 2) visual responsivity and the contrast transfer function.

2.1.4 Contrast response curve and gain adaptation

To study the alterations of cortical processing, we measured the contrast response curve of the mice. The contrast response is one of the classical methods of assessing visual computation capability of visual cortex and it can be measured in several ways. The common feature in this test is the presentation of a stimulus whose contrast can be modulated in terms of intensity.

Most commonly, the stimulus is presented as a grating, of white and black bars that can be static, drifting or inverting (every bar changes color from black to white and vice versa). The grating can be

square-wave (bars) or also sinusoidal. If the study of orientation is not important, a checkerboard can be used in place of the grating. In the checkerboard, the stimulus is provided by the reversal of the black and white squares that form the checkerboard. The levels of white and black defines the contrast of the stimulus. The contrast is modulated by changing the luminance of the black and white squares.

The contrast in studying the visual system is usually expressed as Michelson contrast:

$$K = \frac{L_{max} - L_{min}}{L_{max} + L_{min}}$$

where L_{min}

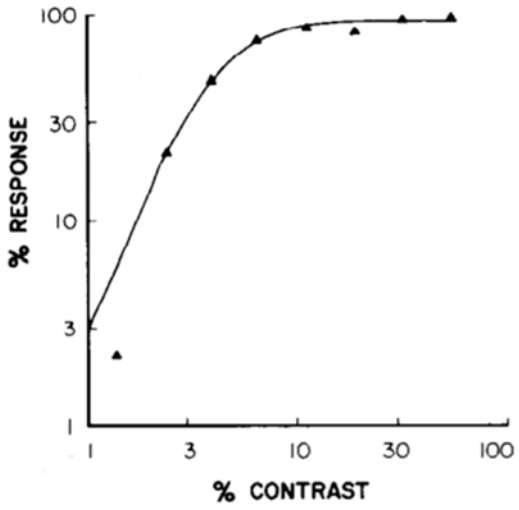

Figure 2.4. Typical contrast response function of a cell of striate cortex of a macaque monkey (Albrecht and Hamilton 1982).

Gain adaptation is now known to be a major computational principle of central nervous system, and it is not just limited to sensory cortices, but it is ubiquitous in the brain and very important also for associative and motor functions (Salinas, Thier, and Jolla 2000).

2.1.5 Parvalbumin interneurons as modulators of gain adaptation

In 2012, a work by the group of Massimo Scanziani (Atallah et al. 2012) dissected the circuit responsible for gain adaptation in response to a contrast stimulation. In mouse primary visual cortex, they investigated the relationship between pyramidal cells of layer 2/3, which are the main "output" population of cells in the cortex (exclusively excitatory), and parvalbumin (PV) interneurons, a class of inhibitory neurons that target soma and perisomatic compartments of pyramidal cells. In this study, they expressed optogenetical tools in PV interneurons, which allowed either activating or inhibiting specifically these interneurons, while recording the electrophysiological activity of pyramidal neurons. They showed that cortical responses in primary visual cortex to a visual stimulation are tuned by the activity of PV interneurons. In particular, a strong effect was shown on the gain adaptation of contrast response curve: when PV interneurons are inhibited, the gain of the contrast response function is increased (Figure 2.5 a, b), while when PV interneurons are activated, the gain of contrast response function is decreased (Figure 2.5 c, d).

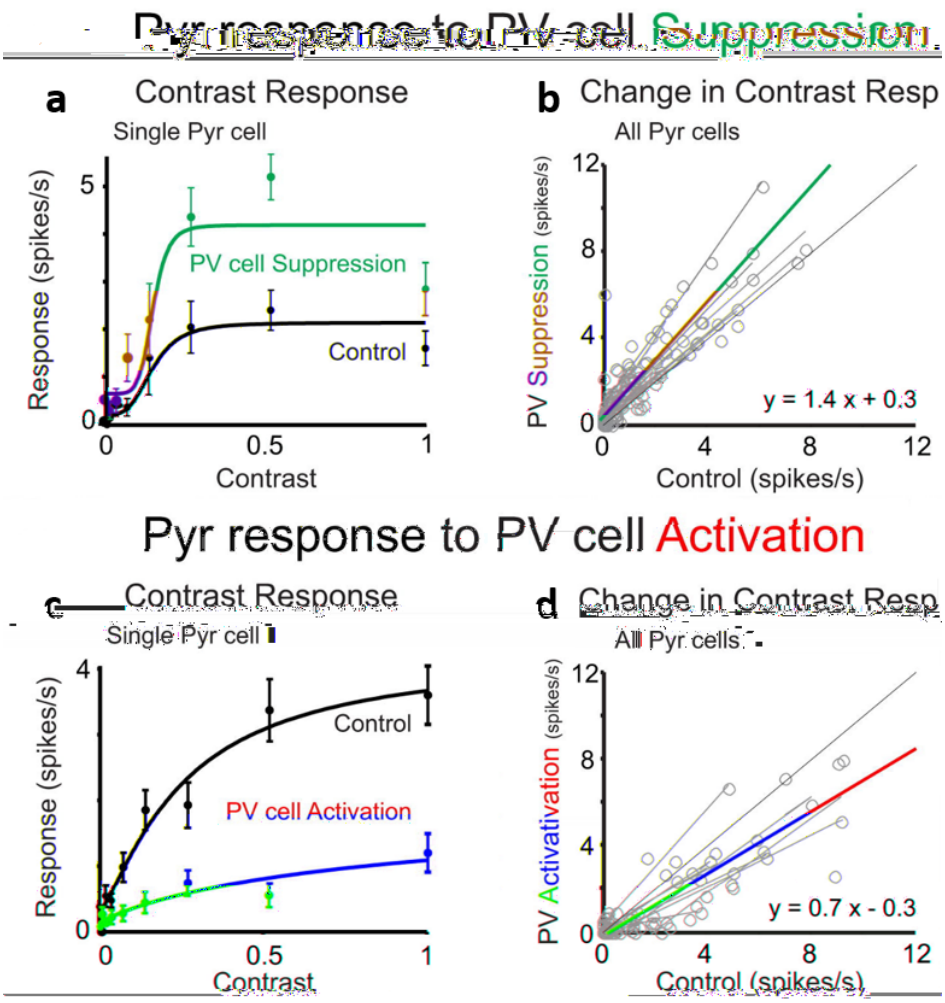

*Figure 2.5. (**a**) Contrast response of a single pyramidal cell in control (black) and during suppression of PV cells (green). Error bars are the SEM. (**b**) Gray: visually evoked spike rate of pyramidal cells under control conditions versus during PV cell suppression (circles; 8 different contrasts for each cell; n = 17 cells). Lines: linear fits to each cell; green line: average linear fit; dotted line at unity. (**c**) Example of contrast response of a single pyramidal cell in control (black) and during activation of PV cells (red). Error bars are the SEM. (**d**) Gray: visually evoked spike rate of pyramidal cells under control conditions versus during PV cell activation (circles; 8 different contrasts for each cell; n = 10 cells). Lines: linear fits to each cell; red line: average linear fit; dotted line at unity.* (Atallah et al. 2012)

These data clearly demonstrate that, by estimating contrast gain, we can estimate the E/I balance in the cortex of the PMD mouse model by investigating steady state SWA and the contrast response.

The analysis of the contrast gain was performed successfully in mice and is also in progress in human patients, to validate the findings that we got in the animal model.

2.2 Materials and methods

2.2.1 Mouse model

Adult (>postnatal day 60) Shank3Δ11$^{-/-}$ mice were used. Mice were generated as previously described by Schmeisser et al. (Schmeisser et al. 2012) and re-derived in a C57BL/6 background (Charles River Laboratories, Calco, Italy). They were housed under constant temperature (21-22°C) with a 12 h light/dark cycle, and provided with food and water *ad libitum*. Shank 3 KO and Control mice were used according a protocol approved by the Italian Ministry of Public Health and they were measured during their subjective day, during the light phase of the illumination cycle.

2.2.2 Surgical procedures

Mice were anesthetized with a solution of urethane 20% as already described in the previous chapter.

The surgical procedure is also similar to the procedure previously described. The mouse was fixed to a stereotaxic apparatus, a craniotomy was performed in correspondence of the visual cortex and a chamber was created around the craniotomy with dental cement (Vertex Dentals).

2.2.3 Electrophysiology recording and visual stimulation

The visual stimuli were provided by an LCD monitor (120 Hz frame and refresh rate, Asus). The stimuli were generated with a custom-made MATLAB program based on the Psychophysics Toolbox (Brainard 1997; Pelli 1997; Kleiner, Brainard, and Pelli 2007).

The stimulus consisted in a black and white, contrast-reversing checkerboard (0.5 Hz of stimulation frequency, 0.04 cycles/degree of square dimension). The contrasts used were: 0%, 1.8%, 2.3%, 5.7%, 28%, 100%.

2.2.4 Up states and down states detection

Analysis of slow-wave oscillations was performed using a custom-made algorithm slightly different from what I described in the previous study. Briefly, a time course of the gamma power was obtained as the root mean square (RMS) of the traces filtered in the gamma band (25-80 Hz), calculated on overlapping time windows of 150 ms. The distribution of the logarithm of the time-resolved gamma power was bimodal, reflecting high gamma activity during up states and low gamma activity during down states. This distribution was then fitted with a double gaussian; the threshold for the discrimination of up states was chosen as the intersection of the two gaussians. A cut-off in the minimum up (down) states duration was set to 100 ms, and up (down) states shorter than the cut-off were assigned to the ongoing down (up) state.

2.2.5 Spectrogram

Spectrograms have been computed using the *mtspecgramc* function of the Chronux toolbox (Mitra and Bokil 2007; "Chronux Toolbox"), with overlapping Hammer windows of 150 ms with a resolution of 50 ms.

2.2.6 Analysis of Visual Evoked Responses

Traces from recordings were analyzed on Matlab using a custom-made program. The visual evoked potential (VEP) of each mouse was calculated as the average of 120-180 trials. The peak amplitude was measured in a window from 90 ms to 500 ms after the stimulus, with respect to a baseline level computed in the 30-80 ms window. Contrast transfer functions obtained for every mouse have been fitted with a Michaelis Menten function: $A(k) = \frac{A_{max} \cdot k}{k_H + k}$, where A is the response amplitude, k is contrast, A_{max} is the response at "saturating" contrast levels and k_H is the contrast at which the amplitude is equal to half A_{max}. The VEP slope was calculated as the angular coefficient of a line fitting the VEP in a window of 80 ms centered on the half-peak value. Gamma band power (25-80 Hz) during the response was calculated for every trial as the root mean square (RMS) of the filtered trace in two different time windows: 30 ms to 80 ms and 90 ms to 500 ms after the stimulus. These two windows were called respectively "baseline" and "response"; then the base 10 logarithm of the ratio between response and baseline gamma power has been calculated and averaged among trials.

2.2.7 Power spectra

Multitaper spectral power density graphs have been calculated on 90-second traces recorded from anesthetized mice with no visual stimulation by using Chronux toolbox (Mitra and Bokil 2007; "Chronux Toolbox") function *mtspectrumc* (Mitra and Bokil 2007).

2.2.8 Power computation of traces

The power of a trace was calculated as the root mean square (RMS) of the trace (filtered or unfiltered). Usually the spectral power density is defined as the square mean of a signal, so in the thesis I will refer to the power as the "RMS power", to avoid any confusion.

$$P_x = \frac{1}{N} \sum_{n=1}^{N} |x(n)|^2$$

$$RMS\ P_x = \sqrt{\frac{1}{N} \sum_{n=1}^{N} |x(n)|^2}$$

I usually report the RMS power in dB, in this case the reported value is actually:

$$RMS\ P_x = 10\log_{10}\left(\sqrt{\frac{1}{N}\sum_{n=1}^{N}|x(n)|^2}\right)$$

2.2.9 Spectrogram

Spectrograms are calculated as short-time fast Fourier transforms using the *mtspecgramc* function of the Chronux toolbox, with an overlapping Hammer window of 150 ms width and 50 ms overlap.

Average spectrograms are obtained by averaging all spectrograms phase-locked on each stimulus presentation (trial), similarly to how VEPs are calculated.

2.2.10 Recording from human subjects

The measurements on human patients were managed in collaboration with Prof. Renzo Guerrini and Dr. Federico Melani from the neuropsychiatry department at Meyer Children Hospital in Florence. The study, named "studio del potenziale visivo in pazienti con sindrome di Phelan-McDermid", has been approved by the Ethical Committee in January 2016, and the experimental procedures followed the rules of 'Buona pratica Clinica' (i.e. good clinical practice).

The recordings were performed at Meyer Hospital. Five electrodes were positioned on the scalp of every subject by means of a conductive paste (electrodes impedance < 20M). An electrode placed on top of the head was used as ground, Fz electrode was used as reference and three channels where acquired: Oz-Fz (channel 1), O1-Fz (channel 2) and O2-Fz (channel 3). The electrodes were connected to a device for amplification and digitalization (Matrix, Micromed). Traces were monitored and recorded using a commercial software (Micromed) and were analyzed with custom Matlab software.

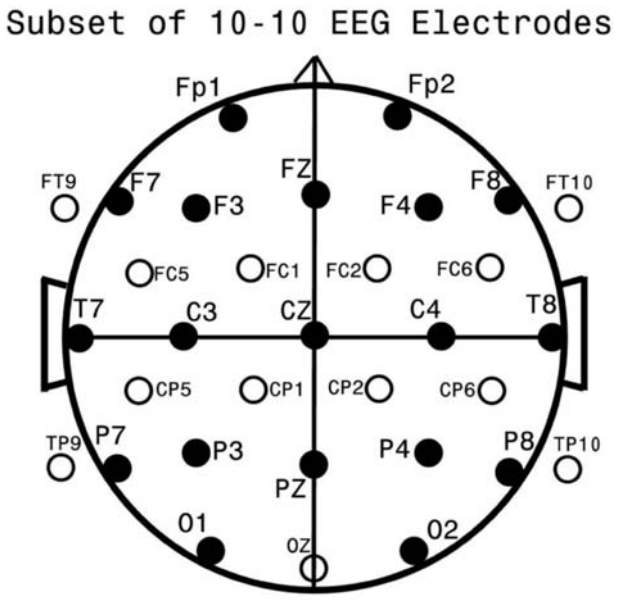

Figure 2.6. Standard EEG Electrode Names and Positions. Head in vertex view, nose above, left ear to left. EEG electrodes: Z: Midline: FZ: Midline Frontal; CZ: Midline Central; PZ: Midline Parietal; OZ: Midline Occipital. Even numbers, right

hemisphere locations; odd numbers, left hemisphere locations: Fp: Frontopolar; F: Frontal; C: Central; T: Temporal; P: Parietal; O: Occipital (Duffy et al. 2011).

2.3 Results

2.3.1 Steady state analysis showed increased activity

As in the mouse model of interictal activity, the first analysis we performed was on the slow-wave activity of the anesthetized mouse primary visual cortex.

Slow wave activity was recorded in both Shank3$^{-/-}$ mice (knockout, KO) and Shank3$^{+/+}$ mice (wild type, WT). An example trace of this activity is shown in Figure 2.7. In these traces, in both WT and KO mice, the up states were present and they did not show any major disruption to a qualitative analysis.

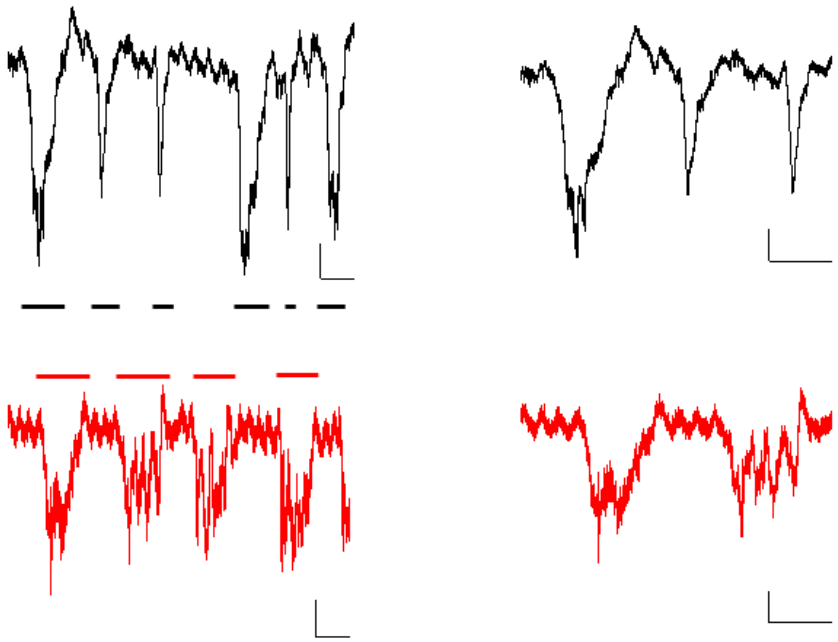

Figure 2.7. Representative up and down states in two control (black) and two KO (red) anesthetized mice. The scale bar value is 0.2 mV on the y-axis, 1 s on the x-axis.

To compare the two groups, power spectra of the whole recording has been computed (Figure 2.8).The spectra of the shank3$^{-/-}$ mice showed increased power on a broad set of frequencies (10-100 Hz).

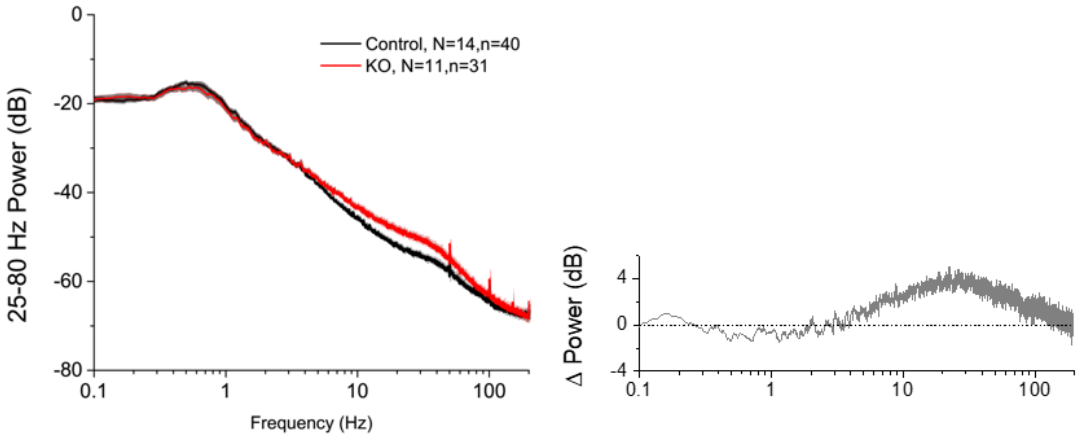

Figure 2.8. Shank KO mice are not openly epileptic. However, spectral analysis of the resting state under urethane anesthesia shows a larger spectral power at all frequencies between a few Hz to about 100 Hz. In particular, there is a diffused increase in the beta (10-25 Hz) and gamma frequency band (25-80Hz) (Mann-Whitney rank test over frequency window from 10-20Hz to 90-100Hz, p<0.001). Lines indicate the mean spectra and the shaded areas indicate the SEM (black, CTRL, N=14 animals, n=40 averaged spectra; red, KO, N=11, n=31).

For this reason, we looked to the temporal and spectral structure of individual up states, to understand where originates this increase in spectral power. By using the technique described in the Method section, we sorted up states from down states based on the instantaneous power in the gamma band. With this analysis, we found a significant difference of the up states duration, with Shank3$^{-/-}$mice displaying markedly longer up states.

Furthermore, we have investigated other parameters: power during the upstate, the amplitude of the recording during the upstate, the frequency of up states. None of these parameters showed a difference between the two groups.

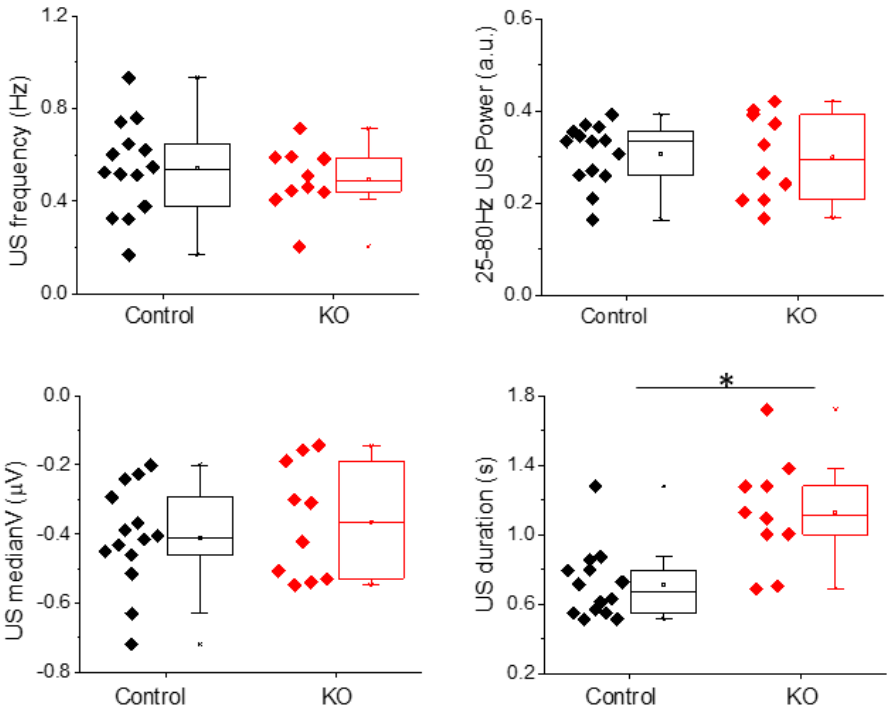

Figure 2.9. Analysis of slow-wave activity in Shank KO mice show an altered duration of up states (Mann-Whitney Test, p<0.05), whereas up and down states were identified automatically by selecting power in gamma band (Control, N=14, KO, N=11).

Thus, these data suggest that, since spectral power is raised over 10 Hz during the up states (see figure 1.1), the difference in duration explains the difference in spectral power between KO and WT mice.

Longer up states could be due to several underlying mechanisms. The most likely explanation suggests an involvement of inhibitory neurons, since it has been shown that both the triggering of an up state and its termination is linked to the activity of somatostatin and parvalbumin interneurons (Zucca et al. 2017), as previously mentioned in the introduction. In this framework, upstates are terminated by the activation op PV interneurons that are recruited by the collective activity occurring during the up state. This suggests an impairment in the recruitment of interneurons and this might represent a major player in determining the disease at cortical level.

2.3.2 Gain control is impaired in Shank KO mice

After obtaining such promising data from the resting state cortex, we recorded activity during visual stimulation by estimating the contrast response gain control in the primary visual cortex. LFPs were recorded in the mouse cortex from layer 2/3 in response to alternating checkerboards presented on a computer display.

Six different contrasts were used, 0%, 1.8%, 2.3%, 5.7, 28%, and 100%. The stimulation was provided by the reversal of the checkerboard with a period of 2 seconds and was repeated 40-100 times.

The LFP recording was then segmented to single trials, corresponding to each checkerboard reversal. All trials of the same contrast were then averaged, to reduce noise and measure more easily the visual evoked potential (VEP). The VEP were collected and analyzed for all 6 stimulations in both KO mice and WT mice.

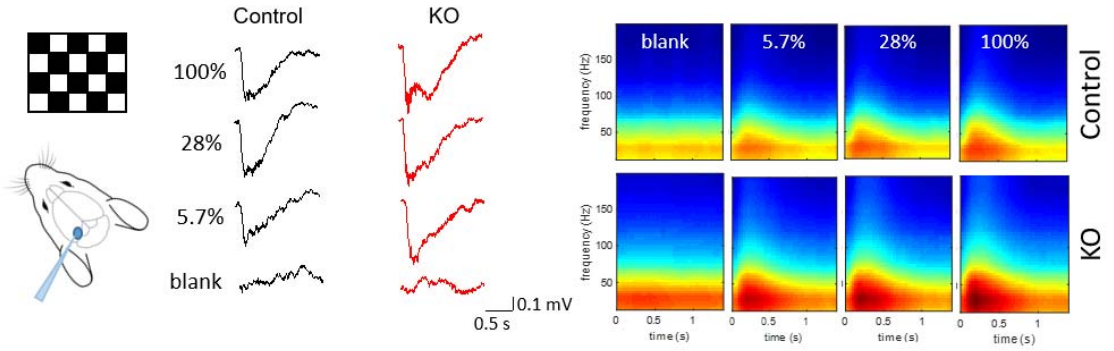

Figure 2.10. (left) Experimental paradigm and exemplificative waveforms (average of 60-100 trials) of responses to alternating checkerboards. (right) Short-time fast Fourier Transformed for Control (N=17) and KO mice (N=17) show an enhanced power in response to visual stimuli and with a blank stimulus.

The amplitude of the VEP measured in the time domain is proportional to the intensity of the stimulation and the curve obtained when plotting all the VEP amplitudes is a non-linear function, that nears saturation when approaching the maximum contrast. This is the contrast transfer function and, as explained above, its non-linearity is due to the cortical mechanism of gain control that makes sure that the brain response does not saturate for strong stimuli.

The contrast transfer function for Shank3$^{-/-}$ mice showed signs of early saturation, at relatively low contrast values. In particular, at contrast 28% the response has already reached saturation: even if this stimulus is very different from a 100%, it elicits a VEP of similar amplitude.

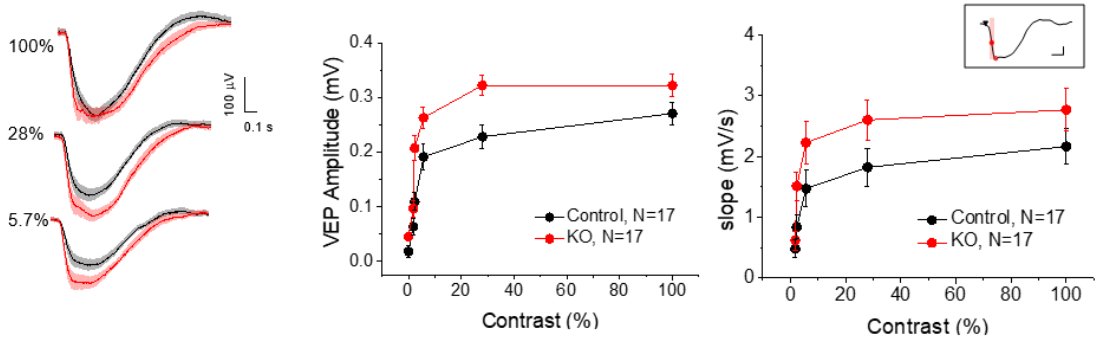

Figure 2.11. (left) Mean VEP waveforms at three different contrast show higher responses in KO mice at contrast 28% and 5.7%. (center) Contrast response curve is significantly different in Shank KO (N=17) versus CTRL mice (N=17) (Two-Way ANOVA, Holm-Sidak test, p<0.001). (right) Analysis of slope (calculated as shown in the inset and explained in Methods) show the same trend of contrast response in KO versus Control mice indicating a more rapid response to visual stimulation in KO mice (Two-Way ANOVA, post-hoc Holm-Sidak test, P<0.001).

The WT mice show a more controlled response that does not saturate for any presented stimulus. This alteration was also quantified by fitting the contrast response curve for each mouse with a hyperbolic function (Michaelis-Menten, see Materials and methods). For each mouse, the fitting gave two parameters: the maximum amplitude A_{max} and the K_H, the contrast at which the response is half A_{max}. In Figure 2.12 (left and center) the two parameters are plotted for control and KO mice. While A_{max} did not show any difference between the two groups, the K_H was significantly lower for KO. This means that the contrast response functions reached the same level of saturation in the two groups, but they reached saturation faster in KO mice.

Also the power in gamma band (25-80 Hz) during the response was quantified for different contrasts. The resulting curve showed the same features as the one calcula

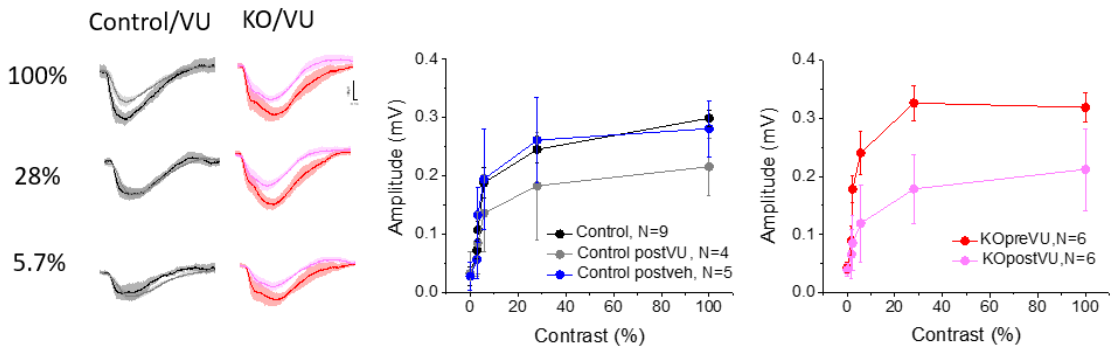

Figure 2.13. Contrast response is affected after 1h from i.p. injection of the mGluR5 agonist VU0409551. KOpreVU/postVU, n=6, Control,N=9,Control pre/postVU,N=4, CTRLpre/postveh, N=5.Two-Way ANOVA, post-hoc Holm-Sidak, KO vs. KO+VU, p<0.001, KO vs. CTRL, p=0.006, CTRL vs. KO+VU, p=0.011, Control postveh vs.KO postVU, p=0.025.(C) Paired comparison before and after treatment in KO (N=6) and Control mice respectively treated with VU (N=4) show an effect of VU on contrast response at maximum contrast also in Contrl mice (Wilcoxon signed rank test; 100% contrast, KOpreVU/KO postVU, p=0.043; Control preVU/Control postVU, p=0.003; 35% contrast, KOpreVU/KO postVU, p=0.02; Control preVU/Control postVU, not significant; 13% contrast, KOpreVU/KOpostVU, p=0.007; CTRLpreVU/CTRLpostVU, not significant. Contrast response curve of KO VU and Control VU are superimposable, indicating an effect of VU on control gain both in KO and in Control mice.

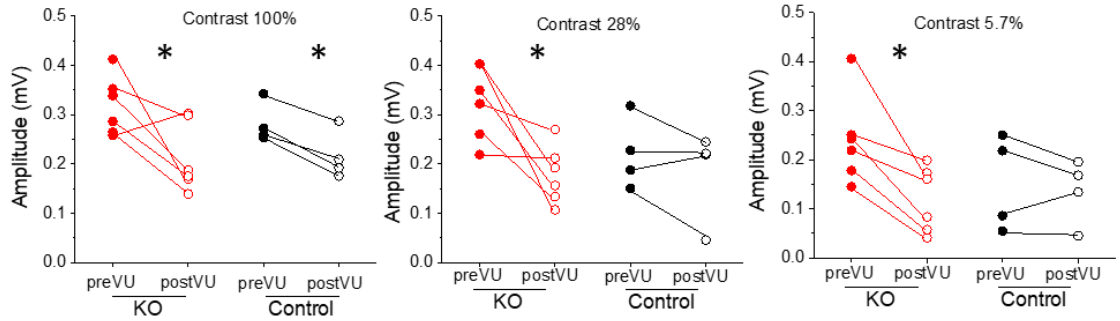

Figure 2.14. Paired quantification of the shift in VEP amplitude in response to the top three contrasts. The effect of the drug is very strong on KO mice for all three contrasts. Also for WT mice the response was diminished, but the effect was weaker and statistically significant only for the higher contrast (p<0.5 Wilcoxon signed rank test).

2.3.4 Recording in human. The problem of timing.

After obtaining these results from mice, we had access to recording from human patients. The aim was to investigate the contrast response function of human patients of Phelan McDermid syndrome. We performed EEG recordings from visual cortex, while delivering repeated stimuli, similarly to what we have done in mice.

Recording contrast VEPs in humans was very challenging, due to fact that we were dealing with awake subjects suffering from a mildly to strongly disabling syndrome. The patients were seldom collaborative and would not be easily recorded.

Initially, our setup had a few limitations. Classically, stimuli are presented on a computer screen that occupies only a small fraction of the visual field (about 25 degree) thus requiring that the subject keeps a stable fixation point. This condition requires a strong degree of collaboration from a verbal subject, a condition that is often not met with patients with PMS, which often just look away from the screen and avoid the stimulation. To counter this problem, we substituted the monitor with a virtual reality headset that allows the presentation of the stimuli on a much larger apparent visual field of about 100 degree. In practice, it is impossible not to see the stimulus by looking away from the screen (Figure 2.15).

Figure 2.15. Using a virtual reality headset provides a more reliable measurement of visual evoked potential compared to a normal monitor, especially in case of non-collaborating patients. The traces are averages of 20 repetitions of a checkerboard high-contrast stimulation recorded in a Phelan McDermid patient. In the (top) panel, there is a response trace obtained by using the conventional setup that delivers the stimulus by a conventional monitor. The patient had to look at the screen while being recorded and the quality of the recording strongly depends on whether the patient is moving his head or is looking at the center of the screen. Often PMS patients are not collaborative and therefore can be hard to record. When using a virtual reality headset (bottom), the trace recorded in the same patient in the same session showed a much larger peak, which can be easily identified as a "true response". As expected, when using the virtual reality headset, the quality of the recording was less dependent on the movement of the patients and was overall more stable.

Another limitation was the timing control of the recording: the recording was synchronized by a TTL signal generated by the computer at the time that the checkerboard reverse is issued to the graphic board. Depending on the characteristics of the graphic board and of the monitor, this signal was not necessarily delivered exactly at the time of the actual reversal (Figure 2.16). This È eek ł c e Ĭ th

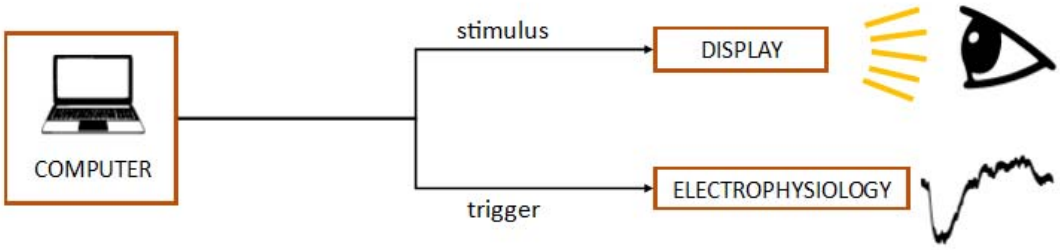

Figure 2.16: The traditional way to record LFP while presenting visual stimulation. LFP recording and visual stimulation are started together, but there may be a delay between the two, depending on the computer and screen used.

Because of these limitations we needed to improve our setup to obtain a better control over the delivery and timing of our stimulations.

2.3.5 Hermes. A simple system to synchronize stimulation and recording

The visual stimuli are generated by a custom Matlab code that employs the toolbox Psychophysics Toolbox (Brainard 1997; Pelli 1997; Kleiner, Brainard, and Pelli 2007). This a widely used library that allows a very efficient display of graphic pattern by progrmming directly any video board compatible with the Open GL standard and it is also used in GNU Octave. Most of the researchers performing visual stimulations use either this toolbox or PsychoPy, which is a similar toolbox for Python.

Even though this toolbox allows a large range of different stimuli and allowed people with low programming skills to write scripts for visual stimulation, it does not always allow a very good grip over the time control of the stimulation. The poor control over the synchronization was quantified for a few systems that used different computers and different screens (Figure 2.17).

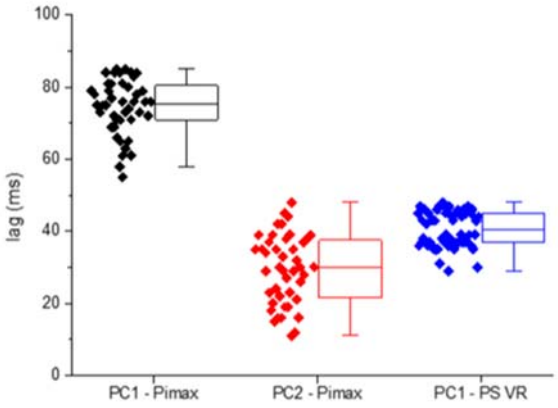

Figure 2.17. The lag between the trigger signal generated by the PC at the time of the software-issued checkerboard reversal and the time at which the reversal actually occurs on the display deends on the VR headset and on the PC. Furthermore, it is quite variable. This lag was quantified for three different systems: The Pimax headset connected to two different PCs (black and red) and the PlayStation headset (blue).

Psychophysics toolbox has some ways to take this delay into consideration and reduce it as much as possible. Nevertheless, depending of the screen and on the computer that is being used, a considerable delay can be produced. What is worse, since the lag has a rather large dispersion, it is impossible to take it into account a priori (Figure 2.17).

One solution can be to use a very fast screen (like a gaming PC monitor) and a fast and light operating system. But this is not always applicable in a laboratory. In particular fast and reliable screens can be quite expensive and might not always be available for any screen dimension. For example, if a very small screen is needed, such as the one required for a VR headset, it might be quite hard to find a fast and responsive model.

For this reason, we tried to overcome this problem by producing an external triggering system, called Hermes, which detects the exact moment when the stimulus is being displayed and quickly synchronizes the start of the recoding.

This system is composed of two parts: a sensor and a controller. The sensor is a phototransistor, that changes the current that is flowing through it according to the light received. The stronger the light received, the higher is the current that can flow through it. The sensor is placed on a corner of the screen, to minimize any disturbance to the stimulation delivery.

In the same position where the sensor is placed, the stimulus is changed to a very bright square that can be seen only by the sensor (Figure 2.18). While the stimulus delivered to the eyes might be changed in contrast and duration, the stimulus delivered to the sensor is always the same. This is to make sure that every stimulus is synchronized in the same way, even is the stimulus itself changes.

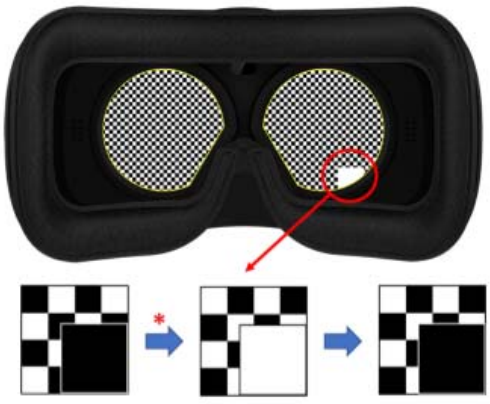

Figure 2.18. An example of the positioning and functioning of the phototransistor sensor. The sensor is placed in a corner of the screen. Here a white square is presented to the sensor when the stimulus starts. The white square stays on for a very brief time (200 ms) and then is turned into a black square.

The controller is designed around an Arduino board, which receives the signal from the sensor and elaborates it. When the stimulus starts on the screen, the Arduino detects the difference in the sensor signal and produces a brief transistor-transistor logic (TTL) signal as output. This output signal can be used to trigger the start of the recording with a very small delay (<0.1 ms). See Appendix for the Arduino code and electronics of the Hermes system.

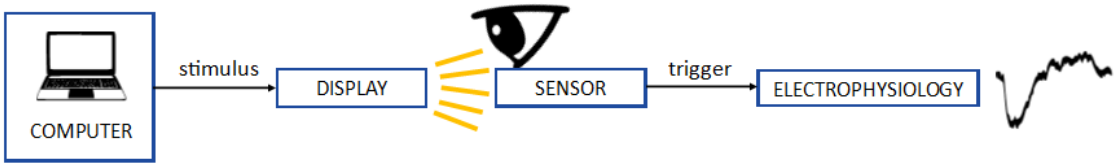

Figure 2.19. Operative scheme of Hermes operation. The sensor and the stimulated eye both sense simultaneously the visual cue. When the sensor is activated, it starts the electrophysiology recording with a minimal delay.

When we used Hermes to perform electrophysiology recording and we compared this system with the traditional system of recording, we found a great timing accuracy. Not only the lag was reduced to less than a millisecond, but also the variability was brought down to negligible values.

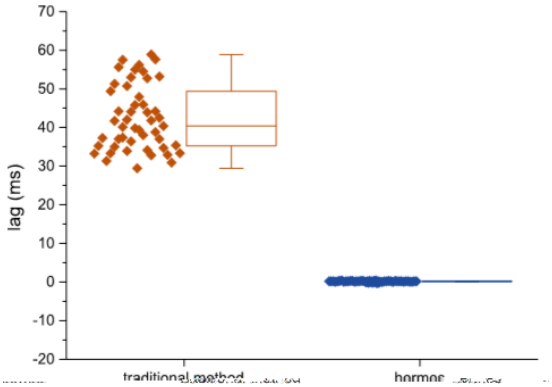

Figure 2.20. Quantification of the lag for traditional system (brown) and of the "Hermes" system (blue). With the traditional method, the lag is very high (median 40.4 ms, interquartile range 14.2 ms). While with Hermes, the lag is negligible with almost no jitter (median 0.2 ms, interquartile range 0.1 ms).

2.3.6 Hermes-based *in vivo* recording

This new recording system was finally tested on human patients. In these experiments, the control of the visual stimulation timing is crucial: In fact, in humans the first peak that is being measured in an EEG signal recorded in response to a visual stimulation is usually the negative peak at 75 ms, called N75. This peak is followed by a positive peak at 100 ms from the stimulation. The timing of these two peaks is important as any change in its value can hint to an impairment in signal conduction of the brain.

Timing between the actual visual stimulation and the start of the recording is also crucial for another reason: if there is a variable delay between the two, this would not affect only the latency of the N75 and P100 peaks, but, because of the jitter in the signal timing, each trial is not averaged exactly in phase with the others thus altering the shape of the average responses and, possibly, to make them disappear into the noise. This can be visualized in Figure 2.21, brown line, where a human control subject is recorded without the accurate triggering provided by Hermes leading to a poor identification of the N75 and P100 components.

When using Hermes, the shape of the VEP becomes clearly visible and its amplitude was improved. Overall, this system will likely allow us to perform better recordings from human patients, even when they are not collaborative and recording becomes challenging.

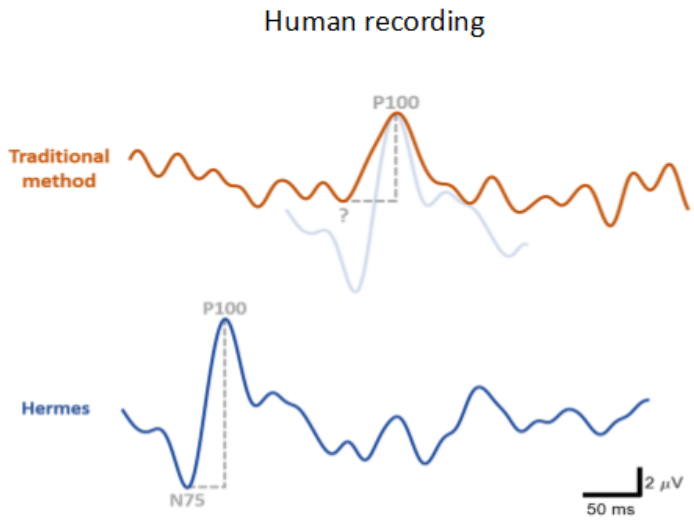

Figure 2.21. Comparison of visual evoked potentials recorded in a human subject, with traditional recording system (brown) or with Hermes (blue). With traditional systems, the VEP was hardly visible because of the variable jitter between soft trigger and actual stimulus presentation. The jitter causes a distortion of the response and a decrement of the S/N ratio. Also notice the long latency. The same patient was recorded with the hard trigger provided by Hermes and the S/N ratio improved markedly and exhibited the expected latency.

With this new tool, we are now confident to perform better measurements on non-collaborative patients and so we are soon to be starting new recordings together with visual stimulations. Starting from patients' parents reporting an increased visual sensitivity of the Phelan McDermid patients, we want to test if the findings that we got from mice recordings can be reproduced also in human patients and if the cortical gain of primary visual cortex is altered. This will be done by measuring response to contrast-modulated checkerboards and full-field flashes.

Other types of stimulation could be used in human patients, to expand the finding also to other areas outside primary visual cortex, like somatosensory cortex or auditory cortex.

2.4 Discussion

The model of Phelan McDermid syndrome exhibited a significant alteration of gain control in the visual cortex, suggesting a higher degree of excitability possibly because of a defective negative feedback from interneurons. Gain control is a property of the system that allows it to scale the input excitatory strength by using feed-forward inhibition. This makes it progressively harder for a given quantity of excitation to produce an increment in the response as input strength increases (Pouille et al. 2009). This expands the dynamic range of afferent inputs that neuronal populations can represent.

Atallah and collaborators demonstrated that increasing/decreasing PV interneurons activity in V1 by optogenetics resulted in a linear decrease/increase of pyramidal cell responses to contrast stimuli (Atallah et al. 2012). This observation suggests that our data can be explained by a reduced inhibitory feedback from PV interneurons to principal cells.

These results can lead to interesting speculations about alterations of sensory processing in PMS patients and about how the sensory processing network excitation/inhibition equilibrium is shifted towards hyperexcitability. This result was not trivial because, even if in PMS patients there is often comorbidity with epilepsy, in the PMS mouse model that we studied there is no sign of spontaneous epileptic discharges. It should be noted that the model we studied represents a simplification of a very complex disease, which can arise from a number of different mutations, each one affecting a different number of Shank3 isoforms as well as a different number of other genes present on the telomere of chromosome 22. Considering all the differences between the mouse model and human disease and all the limitations of working on a mouse model of autism, such as the difficulty to find the same signs and symptoms shown by human patients, one could ask if this model could really enhance our understanding of the human disease. I think that this mouse model can be useful to dissect alterations in the processing network and it can allow the molecular study of proteins involved in the disease as well as the use of drugs to test the validity of putative target proteins. Nevertheless, this study should obviously be accompanied by a study on human patients, to translate the results from the model to the actual disease and to prove the reliability of the model.

According to the results that we obtained from the mouse study, if we were able to obtain similar results in patients, this would demonstrate that cortical computation is altered in the early stages of sensory processing, and this hyper excitability could be present for other sensory modality. Indeed, autistic patients often report aversion for loud noises, bright lights and physical contact (Hohn et al. 2019; Wiggins et al. 2009; Orefice et al. 2019). In the near future we hope to understand whether these signs of the disease might be caused by the basic neurophysiological mechanism we described. If sensory hyperexcitability were present also in patients, that would open the way to the design of an environmental therapy where certain aspect of the sensory landscape could be tuned accordingly. For example, during the preliminary interview phase of the patients, the parents often reported that the affected kid often lamented of excessive light in bright environment, such as on the beach. In contrast they reported that the kid can easily navigate through the house in darkness. These anecdotal evidence suggest that sensory hyperexcitability might be a common feature of the disease.

Our interpretation might be at odd with the fact that Shank3 deficit should impair excitatory synapses, but, how is that possible that this deficit of excitation leads to hyperexcitability? The simplest solution to this apparent contradiction is that that excitatory synapses on interneurons, which are crucial for the recruitment of feedforward inhibition, are more affected than excitatory synapses on pyramidal neurons A possible explanation is that this difference is due to the structure of the excitatory synapse on pyramidal neurons and on interneurons. In pyramidal neurons the synaptic density is confined in the submicrometric volume of the dendritic spine, where the disruption of Shank3 scaffold protein could impact less on the overall integrity of postsynaptic

density. In PV interneurons, excitatory synapses are placed on smooth dendrites and the postsynaptic volume is not confined by a corralling structure. Therefore Shank3 ablation could impact more on excitatory transmission on interneurons, leading to a deficit of inhibition recruitment.

As future perspective, to test the hypothesis of a different deficit of mGluR5 in parvalbumin neurons compared to pyramidal neurons, one possibility is to perform calcium imaging in both parvalbumin and pyramidal neurons, while uncaging glutamate in proximity of the recorded neurons. This is to verify the effect of glutamate release on parvalbumin neurons and pyramidal neurons.

Understanding the role of different neuronal population in the disease is not only important in the theoretical study of PMS, but can also lead to discover some general mechanisms of the brain computation and how this computation can be disrupted in autism and it can also help us improve the patients' life conditions.

Chapter 3: : Chloride concentration measurement and GABAergic inhibition in an epilepsy model

Work published as:

Sulis Sato S., Artoni P., Landi S., Cozzolino O., Parra R., Pracucci E., Trovato F., Szczurkowska J., Luin S., Arosio D., Beltram F., Cancedda L., Kaila K., Ratto G.M. Simultaneous two-photon imaging of intracellular chloride concentration and pH in mouse pyramidal neurons *in vivo*. Proc Natl Acad Sci U S A. 2017 Oct 10;114(41)

3.1 Introduction

3.1.1 Intracellular chloride concentration

Neuronal function relies in the ability to form complex networks where literally billions of interactions exist and each neuron works as a functioning unit that can integrate signals from different inputs and compute an output signal, while retaining also a memory of its activity. Many functions and features of neurons come from the regulation of ionic concentrations. In particular, the ions that are most strictly connected to the neuronal excitability and signal processing are sodium (Na^+), potassium (K^+), chloride (Cl^-) and calcium (Ca^{2+}). Intracellular ionic concentrations are controlled by cell membrane transporters and channels. The intracellular and extracellular concentration of these ions, together with the voltage across the membrane, determine the tendency of these ions of exiting or entering the cell. In particular, for chloride the intracellular concentration is very important and its regulation is subject of debate. While extracellular concentration is fixed around 110 mM, intracellular concentration in adult neurons is slightly below 6-13 mM (Delpire and Staley 2014). In neonatal mice, high intracellular concentrations of chloride have been demonstrated. One major effect of the ionic concentration of chloride, is the effect on GABA transmission.

Traditionally, ionotropic GABA receptors are regarded as inhibitory. When they bind to GABA, they open and the cell conductance to chloride increases. When chloride is low (6-13 mM), the reverse potential for chloride is near to the membrane resting potential. In this case, GABA release results in hyperpolarization or shunting inhibition. When chloride is high, as high as 25 mM for example, GABA release results in chloride efflux leading to membrane depolarization and excitation, since the reverse potential of chloride is at the threshold potential or higher (Ben-Ari 2002).

This means that relatively small change in chloride concentration, from 12 mM to 25 mM, can affect profoundly the effects of GABA release. This is thought to be very important during development, when GABA can act together with glutamate to shape the developing network.

With the years, new evidence has challenged the idea that chloride concentration is fixed at a low level in adult brain for every neuron. For example, it is thought that this concentration can change in disease processes and in immature newly formed neurons. The regulation of chloride concentration is performed by the cell through the activity of two families of transporters: Na^+-K^+-$2Cl^-$ co-transporters (NKCCs) and K^+-Cl^- co-transporters (KCCs).

NKCCs typically transports one Na^+ ion, one K^+ ion and 2 Cl^- ions inside the cell. The ions are transported according to the electrochemical gradient. According to the traditional vision, NKCC1 is the transporter that during development accumulates Cl^- inside immature neurons. NKCC1 works

along gradient for Na^+, whose gradient provides the driving force for the K^+ and Cl^- import. The gradient of Na^+ and K^+ is maintained by the Na^+/K^+ pump (Delpire and Gagnon 2018).

KCCs are co-transporters that transport K^+ and Cl^- together according to their electrochemical gradients. During development, the NKCC1 expression lowers, while the KCC2 expression increases. KCC2 is responsible for transporting both Cl^- and K^+ outside of mature neurons, thus decreasing the concentration of intracellular Cl^-. Cl^- is transported against its electrochemical gradient, because the potassium gradient is used as driving force by KCC2 (Delpire 2000).

Recently we have published the first direct fluorescence imaging of the Cl^- shift during development, that was possible with a tool that was developed in our lab: LSSmClopHensor.

3.1.2 LSSmClopHensor

This fluorescent sensor is composed by two different fluorescent proteins fused together. The chloride sensor is represented by the green fluorescent protein E^2GFP (Bizzarri et al. 2006; Arosio et al. 2007): its fluorescence is sensitive to both pH variations and chloride concentration variations. E^2GFP is fused together with LSSmKate2, which is a red fluorescent protein insensitive to ion variations and serves as a ratiometric standard (Figure 3.1).

Figure 3.1. Structure of LSSmClopHensor construct. The chloride- and pH-sensitive protein E^2GFP is fused with a linker to the chloride- and pH-insensitive LSSmKate2. This sequence is placed under the constitutive strong promoter CAG.

The combination of the two proteins makes possible to perform an absolute measurement of pH and chloride concentration. This capability of ClopHensor to measure both pH and chloride variations is highly convenient, since regulation of Cl^- and pH is linked by the activity of a bicarbonate/chloride cotransporter (but also by some channels, like $GABA_A$ ionotropic receptors).

3.1.3 Spectral properties of LSSmClopHensor

The spectral properties of LSSmClopHensor have been determined both for what concerns one-photon excitation fluorescence and for what concerns two-photon excitation fluorescence by our laboratory. In particular, I want to focus on the two-photon properties of this sensor, since its major appeal is the possibility of performing *in vivo* intravital chloride imaging.

The excitation spectrum of E^2GFP is dependent on pH and Cl concentration. With pH changes, the protonation status of E^2GFP changes and also the excitation spectrum changes as shown in Figure 3.2 (right). Any excitation spectrum shown for a certain pH can be expressed as a linear combination of the spectrum of fully protonated protein (pH 6.0) and fully deprotonated protein (pH 8.0), as shown in Figure 3.2 (left).

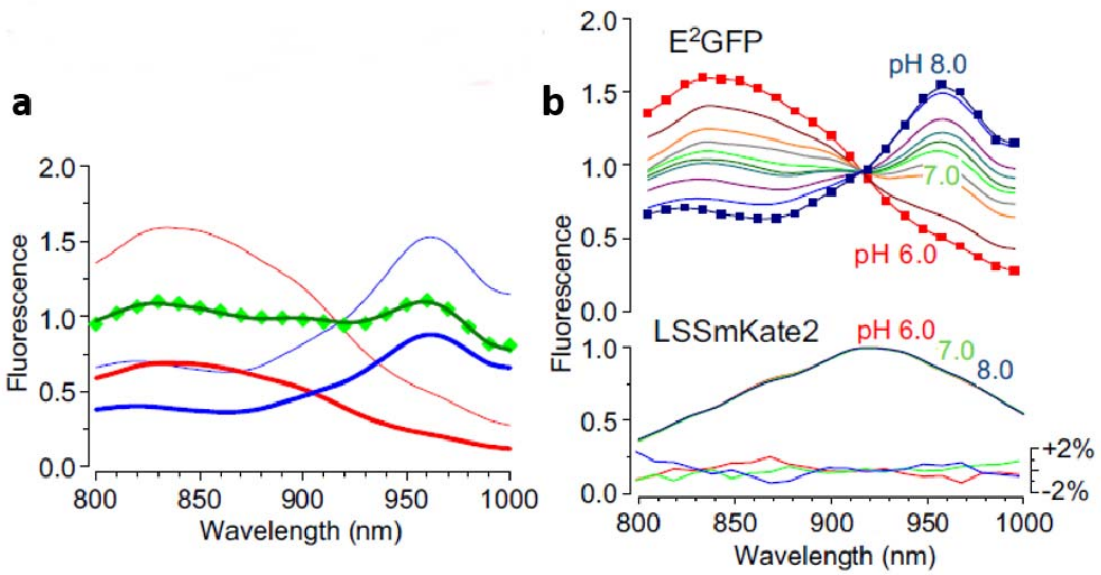

Figure 3.2. (left) Linear decomposition of the spectrum obtained at pH 7.0 (green symbols) on the spectra obtained at pH 6.0 and 8.0 (thin red and blue lines, respectively). The two components are represented by the thick red and blue curves, respectively, and their sum is the line running through the experimental points. (right) Excitation spectra of the E2GFP and LSSmKate2 components of LSSmClopHensor at different levels of pH at 24 °C. Data have been corrected for bleed through and normalized using the peak of the LSSmKate2 emission. The non-labeled spectra of E²GFP have been obtained at pH 6.4, 6.8, 6.9, 7.1, 7.2, 7.4, and 7.6. The excitation spectrum of LSSmKate2 is pH-insensitive: Lower shows the normalized difference (percentage) between the spectra obtained at pH values of 6, 7, and 8, with the mean spectrum averaged for all pH levels.

Chloride has a different effect on E²GFP fluorescence properties: binding to Cl^- quenches the fluorescence, so it reduces the overall fluorescence of the protein. Chloride binds to E²GFP with a dissociation constant (k_d) that depends on the protonation status of the protein (Figure 3.3). At physiological pH (~7.2) the k_d is ~40 mM. This value is not too far from physiological values, thus making the sensor suitable for experiments in cells and *in vivo*.

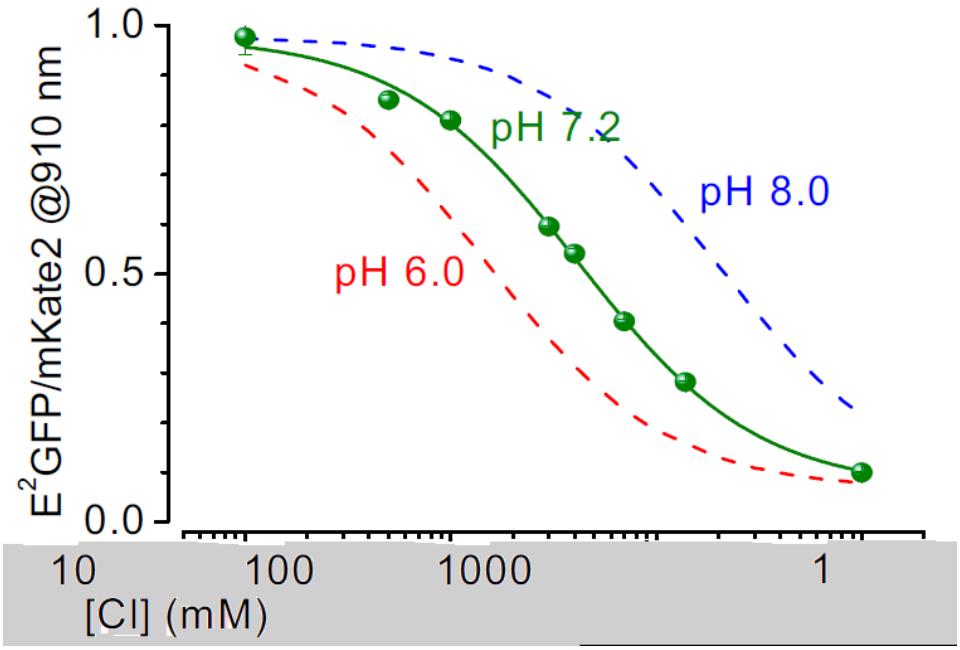

Figure 3.3. Chloride determines the quenching of the E²GFP signal as shown by the loss of fluorescence measured at the isosbestic point. Green circles and line of best fit show the ratio of the fluorescence excited at 910 nm in the green and red channels (normalized to 1 at the maximum) as a function of chloride concentration. The apparent chloride K_d depends on pH, because chloride binds only to protonated E²GFP. Dashed lines are calculated for pH 6.0 and 8.0.

3.2 Materials and methods

3.2.1 Animal and procedures for *in vivo* imaging

LSSmClophensor was transduced by *in utero* electroporation in CD-1 mice at embryonic day 15.5 to transfect neuronal progenitors of layer 2/3 pyramidal neurons of the visual cortex. Before imaging, mice were anesthetized with an intraperitoneal injection of urethane (1-1.5 g/kg), and were measured during their subjective day. Craniotomy (2- to 3-mm diameter) was performed as described previously, and the *dura mater* was removed to reduce light scattering. A custom-made steel head post with a central imaging chamber was glued to the skull. Hypercarbia was induced by exposing the animals to a mixture containing 30% CO_2 in environmental air. This study was performed in accordance with the recommendations of the Italian Ministry of Health.

3.2.2 Solutions

The composition of the sterile saline solution was 126 mM NaCl, 3 mM KCl, 1.2 mM KH_2PO_4, 1.3 mM $MgSO_4$, 26 mM $NaHCO_3$, 2.4 mM $CaCl_2$, 15 mM glucose, and 10 mM Hepes, pH 7.4.

3.2.3 Bleed-Through correction for LSSmClopHensor.

LSSmClopHensor emission was measured in two channels: a red channel and a green channel. The two-photon excitation spectra measured in the green channel strongly depend on pH. The pH dependency was also observed in the red channel as a result of bleed through of the E^2GFP emission. The magnitude of bleed through was determined by purifying the proteins composing the sensor (E^2GFP and LSSmKate2) and by measuring their fluorescence separately in both emission channels. These data provided the coefficients $\alpha(\lambda)$ and $\beta(\lambda)$ that describe the cross-talk between the emission channels. The fluorescence of E^2GFP and LSSmKate2 corrected for bleed through is given by the following system [3.1] of linear equations.

$$[3.1] \quad \begin{cases} G_*(\lambda) = G_{raw}(\lambda) - \alpha(\lambda) R_*(\lambda) \\ R_*(\lambda) = -\beta(\lambda) G_*(\lambda) + R_{raw}(\lambda) \end{cases}$$

Where $G_{raw}(\lambda)$ and $R_{raw}(\lambda)$ label the fluorescence measured in the green and red channels (after background subtraction and flat correction), and $G_*(\lambda)$ and $R_*(\lambda)$ indicate the fluorescence that originates from E^2GFP and LSSmKate2, respectively. LSSmClopHensor is characterized by the absence of intramolecular FRET, since LSSmKate2 has a very large Stokes shift: its peak of absorption (460 nm) is much bluer than the emission peak of E^2GFP (530 nm). To compare the sensor spectra obtained at different pH values, we had to consider that different samples had slightly different protein concentrations. Since the optical properties of LSSmKate2 are not influenced by pH, we normalized each spectrum at the peak of R_*, and this normalization is used through the study.

So, following [3.1], the "true" green ($G_*(\lambda)$) and red ($R_*(\lambda)$) components can be extracted, since the $\alpha(\lambda)$ and the $\beta(\lambda)$ are calculated during the calibration on the isolated proteins. After this, the first value that can be calculated is pH, just by using the green fluorescence.

3.2.4 Measurement of pH and calibration of LSSmClopHensor

The excitation spectrum of LSSmClopHensor at a given pH, $G_{*pH}(\lambda)$, can be described as the linear combination of the protonated ($G_{*_{6.0}}$) and deprotonated ($G_{*_{8.0}}$) spectra according to the equation [3.2].

$$[3.2] \quad G_{*_{pH}}(\lambda) = \delta G_{*_{6.0}}(\lambda) + \varepsilon G_{*_{8.0}}(\lambda)$$

This is a set of n equations, where n is the number of wavelengths at which spectra are sampled. If n = 2, the system becomes a simple two-equation system, written in [3.3].

$$[3.3] \quad \begin{cases} G_{*_{pH}}(\lambda_1) = \delta G_{*_{6.0}}(\lambda_1) + \varepsilon G_{*_{8.0}}(\lambda_1) \\ G_{*_{pH}}(\lambda_2) = \delta G_{*_{6.0}}(\lambda_2) + \varepsilon G_{*_{8.0}}(\lambda_2) \end{cases}$$

This system can be solved analytically according to the standard ratiometric analysis. For dynamic imaging, this was the analysis that was performed and the following is the analytic solution for determining δ and ε.

$$[3.4] \quad \begin{cases} \delta = -\dfrac{G_{*_{8.0}}(\lambda_1) \cdot G_{*_{pH}}(\lambda_2) - G_{*_{8.0}}(\lambda_2) \cdot G_{*_{pH}}(\lambda_1)}{G_{*_{6.0}}(\lambda_1) \cdot G_{*_{8.0}}(\lambda_2) - G_{*_{6.0}}(\lambda_2) \cdot G_{*_{8.0}}(\lambda_1)} \\ \varepsilon = \dfrac{G_{*_{6.0}}(\lambda_1) \cdot G_{*_{pH}}(\lambda_2) - G_{*_{6.0}}(\lambda_2) \cdot G_{*_{pH}}(\lambda_1)}{G_{*_{6.0}}(\lambda_1) \cdot G_{*_{8.0}}(\lambda_2) - G_{*_{6.0}}(\lambda_2) \cdot G_{*_{8.0}}(\lambda_1)} \end{cases}$$

In dynamic imaging, *[3.4]* was the equation used, with the two wavelengths λ_1=860 nm and λ_2=910 nm.

If possible, it is better to use a larger set of excitation wavelengths, that provides a result that is less sensitive to errors. When having more than 2 wavelengths, δ and ε can be determined by a least squares regression analysis, which can be performed by finding the δ and ε that minimize the residual sum of squares (RSS) defined as in [3.5].

$$[3.5] \quad RSS = \sum_{i=1}^{n} \left(G_{*_{pH}}(\lambda_i) - (\delta G_{*_{6.0}}(\lambda_i) + \varepsilon G_{*_{8.0}}(\lambda_i)) \right)^2$$

The size of the residue is an indicator of the quality of the fit. We applied this procedure to the dataset of Figure 3.2 (right): for each spectrum, we determined δ and ε.

A calibration curve can be obtained by the relationship between the polar angle $\theta = \operatorname{atan}(\varepsilon/\delta)$ and the pH of the fitted spectra. The calibration is fitted with the following sigmoidal function:

$$[3.6] \quad \theta = \frac{\theta_R - \theta_L}{1 + 10^{(pK_a - pH)a}}$$

Where pK_a is the affinity for H^+. The fit parameters (θ_R, θ_L, pK_a, and a) have been calibrated at three different temperatures (24 °C, 31 °C, and 36 °C).

3.2.5 Computation of the Intracellular Chloride Concentration

Since Cl^- binds solely to the protonated form of E^2GFP, only a fraction of the sensor fluorescence depends on $[Cl^-]_i$, and this fraction in turn depends on pH. This is summarized by the following equation (Arosio et al. 2007):

$$[3.7] \quad K_d^{Cl^-}(pH) = 13.1 \cdot \frac{1 + 10^{(pK_a - pH)}}{10^{(pK_a - pH)}}$$

where 13.1 mM is the Cl^- affinity for fully protonated E^2GFP (Arosio et al. 2010), and the term on the right is the inverse of the fraction of nonprotonated sensor (i.e., the fraction that is Cl^--insensitive). Finally, $[Cl^-]_i$ is given by equation [3.8].

$$[3.8] \quad [Cl^-] = K_d^{Cl^-}(pH)\left(\frac{r(0)}{r(Cl^-)} - 1\right)$$

Where r(0) is the ratio between the fluorescence of E^2GFP and LSSmKate2 measured at the isosbestic point when $[Cl^-]_i = 0$. The term r(Cl) is the same ratio measured at a given $[Cl^-]_i$.

3.2.6 *In Vivo* Two-Photon Imaging

In vivo two-photon imaging was performed on a Prairie Ultima Multiphoton microscope equipped with two mode-locked Ti: Sapphire lasers (Coherent Chameleon Ultra II and Coherent Verdi-Mira). Acquisitions were performed with a water immersion lens (60×, 1.00 N.A.; Olympus) with image size of 512 × 512 pixels and at optical zoom 2, leading to a field of 102 × 102 µm and a pixel size of 0.2 µm per pixel. Before each imaging session, we measured the power of the excitation laser at the optic bench and at the output of the objective lens for each wavelength used. This conversion function is required to infer the power at the sample (which is not accessible after the mouse is placed under the objective) from the power measured on the optic bench.

Time-lapse imaging was performed by alternating the excitation from the two lasers tuned at 860 nm and 910 nm. The two beams have been adjusted to have orthogonal polarization, so that they can be combined by a polarizing beam splitter. Two different sets of mirrors placed before the beam splitter were used for alignment of the two beams. The wavelength was selected by fast electromechanical shutters synchronized to the microscope scanning unit. The data were analyzed by custom ImageJ macros.

3.3 Results

Dynamic imaging of H^+ and Cl^- ions *in vivo*

During network activity, $[Cl^-]_i$ and pH are modulated by channel-mediated fluxes driven by ionic driving forces for Cl^- and for channel-permeant acid–base species (mainly HCO_3^-), respectively. However, active transport of Cl^- and H^+/HCO_3^- will oppose the effects of the passive fluxes, and thus, the instantaneous ion concentrations are set by the properties of the ion channel/transporter relationships (Kai Kaila et al. 2014).

So far, there are no data on intracellular Cl^- and pH dynamics in cortical neurons *in vivo*. Measurements of the steady-state values of pH and $[Cl^-]_i$ based on sampling the excitation spectra at several wavelengths are inherently slow and cannot provide time-resolved data. However, with ClopHensor it is possible to measure simultaneously pH and $[Cl^-]_i$ by alternating only two different excitation wavelengths, as demonstrated in Equation [3.4]. In these experiments, excitation was provided by two tunable lasers, which were steered and combined before the scanning head, and alternatively selected by electromechanical shutters during acquisition (Figure 3.4 a, b). We constructed time-lapse sequences by alternating excitation at 860 nm and at the isosbestic point at 910 nm: each pair of E^2GFP images provides an estimate of pH, while the LSSmKate2 images provide the signal for the correction of excitation power at the focal plane and the reference for computation of $[Cl^-]_i$. We performed dynamic measurements of pH and $[Cl^-]_i$ *in vivo* after induction of hypercapnia by inhalation of a gas mixture containing 30% CO_2 in air. Breathing this gas mixture induces fast acidification of the brain extracellular space and brain tissue (Albertazzi et al. 2011) leading to suppression of neuronal activity involving multiple mechanisms, such as enhancing GABAergic transmission (K Kaila 1994), as well as inhibition of NMDA receptors and voltage-gated Na^+ and Ca^{2+} channels (Tombaugh and Somjen 1996; Traynelis and Cull-Candy 1990). Time-lapse imaging was performed while recording the LFP with an intracortical KCl electrode inserted in the [illegible]

E Åi

7 mM. In all cases, the recovery of $[Cl^-]_i$ commenced immediately after the abrupt end of seizure activity. Interestingly, there was also a fall in pH that had a slower time course than the increase in $[Cl^-]_i$. These data do not permit identification of the underlying mechanism, but both a $GABA_AR$-mediated efflux of HCO_3^- and a production of metabolic acid are likely to contribute to the cellular acidosis, which in fact, is characteristic of seizures and seizure-like activity (Pavlov et al. 2013; Xiong, Saggau, and Stringer 2000).

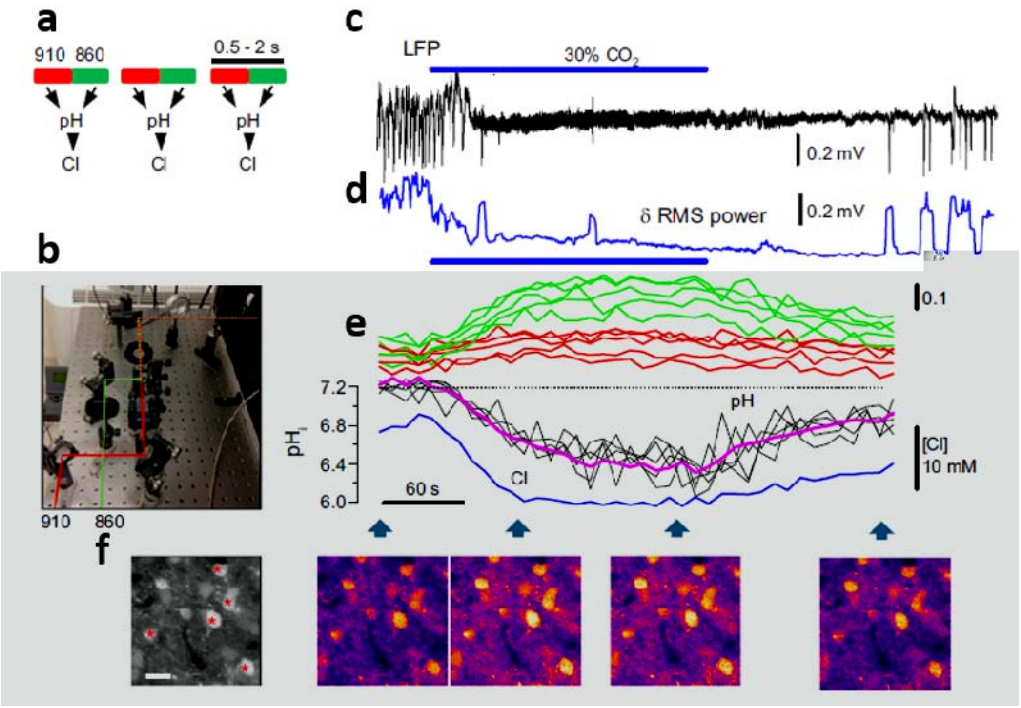

*Figure 3.4. Dynamic imaging of pH and Cl_i in vivo during hypercapnia induced by CO_2 inhalation. (**a**) Schematics of the acquisition processes: the sensor is excited alternatively at 910 and 860 nm by using two tunable lasers controlled by fast electrometrical shutters. The two fluorescence images can be obtained within 500 ms, and successive pairs can be acquired at the desired interval. The alternated images are used to compute pH. The chloride estimate is then obtained by the green to red emission ratio. (**b**) Schematic of the excitation pathway. The beams emerge from the shutters (not depicted) with orthogonal polarization, and they are combined with a polarizing beam splitter before entering in the scanning head. (**c**) LFP recorded in the occipital cortex of a P35 mouse anesthetized with urethane (band pass 0–4 Hz). The initial phase of the recording shows the characteristic oscillations present during slow-wave sleep characterized by a strong enhancement of the δ band of the EEG. The hypercarbic condition was induced by letting the mouse breath a mixture of 30% CO_2 in air with a face mask (blue horizontal line). (**d**) The RMS power of the δ band EEG signal drops rapidly after the onset of hypercarbia. (**e**) Time course of E_2GFP fluorescence after correction for bleed through and excitation loss. Red and green traces indicate the time course of fluorescence excited at 860 and 910 nm (green and red, respectively). Hypercarbia causes a clear increase of the fluorescence of the protonated peak, indicating intracellular acidification. The ratio of the two channels provides the pH measurement as shown in the traces for five different cells in the field (thin black lines) and for the neuropile (thick red line) in Lower. At this time resolution, all cells and the neuropile show a remarkably similar behavior. A representative trace from one cell in the field shows a decrement of $[Cl^-]_i$ (thick blue line) as pH falls and the network activity becomes suppressed. (**f**) Sample images of the fluorescence excited at 860 nm at the time points indicated by the arrowheads. The leftmost panel represents a maximum projection of the entire stack, and the five cells reported in the fluorescence recordings are identified by red stars. (Scale bar: 20 µm.)*

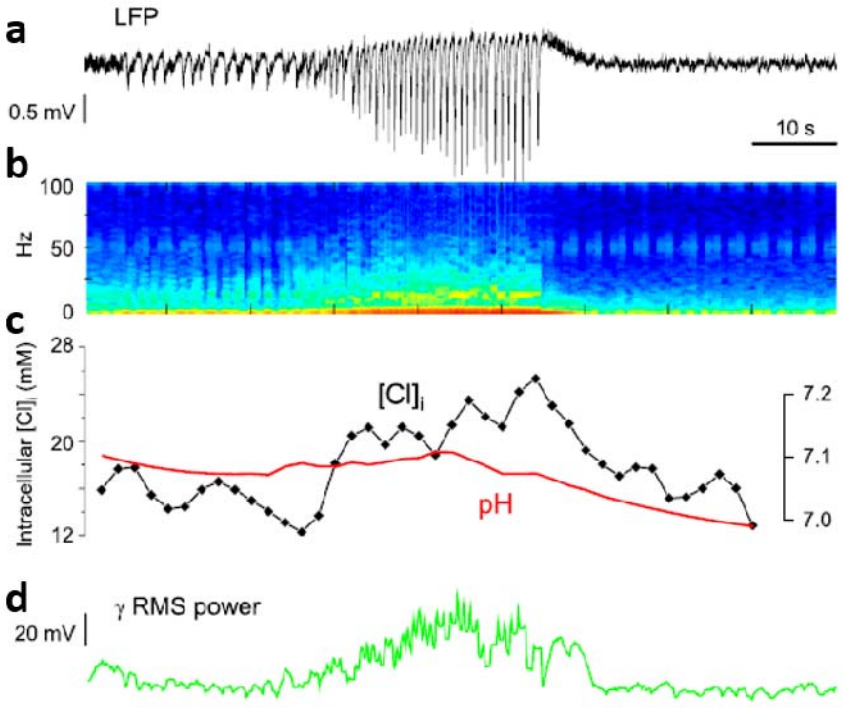

*Figure 3.5. Dynamic imaging of pH and Cl_i during epileptic seizure in vivo. (**a**) Seizures were triggered in the occipital cortex in vivo in an adult mouse (about 2 months of age) by means of localized treatment with the convulsive agent 4-AP. The trace shows the LFP recorded during a seizure characterized by high-frequency firing and a large increase of the power spectra at both low and high frequencies (**b**). (**c**) The simultaneous measurement of pH and Cl_i shows a sharp chloride increase at the onset of the seizure; note also the long-lasting intracellular acidification during and after seizure. (**d**) The temporal profile of the chloride influx correlates with the profile of the RMS power in the γ band (30–80 Hz). The recovery of chloride begins immediately at the end of high-frequency firing.*

3.4 Discussion

In this last part of my thesis, I demonstrated how LSSmClopHensor can be used to perform time-resolved measurement of pH and $[Cl^-]_i$ changes, to investigate GABAergic inhibition during alkaline challenge and epileptic seizures. The importance of chloride intracellular concentration in pathology has been only partially investigated, also because of the difficulty of performing a direct and precise measurement of chloride concentration and because of the sensitivity needed to detect a Cl^- concentration variation sufficient to determine a dramatic change of $GABA_AR$ activation effect, which is "only" a shift of a few mM.

From the measurements of both pH and intracellular chloride during seizures and in hypercarbia-induced termination of epileptic discharges, we found an interesting result: epileptic discharges rapidly increase intracellular chloride concentration and lower intracellular pH, although with a slightly slower timing. This acidification persists also after the termination of the seizure. If hypercarbia is induced during a seizure, intracellular pH and chloride concentration get lower and the seizure is terminated (Albertazzi et al. 2011). This is consistent with reports from the literature of CO_2 being able to terminate seizures and validates the theory according to which the spontaneous termination of a seizure is caused by the intracellular pH decrease consequent to the seizure itself. This is an important *in vivo* direct measurements of both pH and chloride concentration, which can support the claim of the use of carbon dioxide as treatment for seizures (Miller 2011). This could also prove very useful in case of epilepsy resistant to drug treatment and provides an insight on the role of chloride and pH in seizures.

Traditionally chloride intracellular concentration is derived by measuring the reverse potential in patch clamp recording. This measurement presents several drawback: it requires the use of perforated patch in order not to perturb intracellular chloride, leading to a rather large and variable input resistance. This can lead to a series resistance error in the clamp potential when away from the Cl reversal. Furthermore, this is also problematic in order to obtain a good space clamping of the neuron. Finally, it is obviously impossible to obtain a dynamic readout of chloride concentration during transient, out of equilibrium events as those I described.

Chloride genetically encoded sensors can offer some advantages: the measure of chloride concentration is direct, there is less disturbance of the system i.e. a less invasive technique is used since no perforation of the brain surface in needed. Compared to other chloride sensors, LSSmClopHensor showed a k_d ~40 mM very suitable for experiments in neurons, while another chloride sensors has the much higher k_d of 119 mM (Clomeleon). Nevertheless, it should be noted that a more sensitive version of Clomeleon, called Super Clomeleon, has also been developed (k_d ~20-40mM).

LSSmClopHensor was effectively validated as a sensor for assessing dynamic measurement of chloride and pH variations *in vivo*. These measurements provided a proof of principle to assess the applicability of this sensor to a complex problem, like a rapid variation of both chloride and pH in neurons during a fast event, as an epileptic seizure.

This tool could be effectively used for several others models of neurological disease or physiological neural variations, like stroke, traumatic injury, neuroendocrine responses and circadian rhythm in neurons just to name a few.

Although the dispersion of the data can make the sensor less reliable when measuring absolute chloride concentration in a single cell, the population measurement leads to reliable values with acceptable error range, in the range of the "classical" chloride concentrations previously reported. This makes the sensor particularly suitable for measurements of a chloride concentration shift

(repeated measurements of the same cell) and population measurements (measurement repeated in different cells).

References

Aarts, J H, C D Binnie, a M Smit, and a J Wilkins. 1984. "Selective Cognitive Impairment during Focal and Generalized Epileptiform EEG Activity." *Brain* 107 (Pt 1: 293–308.

Aeschbach, Daniel. 2009. "Slow Waves and Learning: Beyond Correlations." *Sleep* 32 (10): 1253–54. https://doi.org/10.1093/sleep/32.10.1253.

Ahnaou, A., D. Moechars, L. Raeymaekers, R. Biermans, N. V. Manyakov, A. Bottelbergs, C. Wintmolders, et al. 2017. "Emergence of Early Alterations in Network Oscillations and Functional Connectivity in a Tau Seeding Mouse Model of Alzheimer's Disease Pathology." *Scientific Reports* 7 (1): 1–14. https://doi.org/10.1038/s41598-017-13839-6.

Albertazzi, Lorenzo, Marco Brondi, Giovanni M Pavan, Sebastian Sulis Sato, Giovanni Signore, Barbara Storti, Gian Michele Ratto, and Fabio Beltram. 2011. "Dendrimer-Based Fluorescent Indicators: In Vitro and in Vivo Applications." *PloS One* 6 (12): e28450. https://doi.org/10.1371/journal.pone.0028450.

Albrecht, G, and B Hamilton. 1982. "Striate Cortex of Monkey and Cat : Contrast Response Function" 48 (1).

Arosio, Daniele, Gianpiero Garau, Fernanda Ricci, Laura Marchetti, Ranieri Bizzarri, Riccardo Nifosì, and Fabio Beltram. 2007. "Spectroscopic and Structural Study of Proton and Halide Ion Cooperative Binding to Gfp." *Biophysical Journal* 93 (1): 232–44. https://doi.org/10.1529/biophysj.106.102319.

Arosio, Daniele, Fernanda Ricci, Laura Marchetti, Roberta Gualdani, Lorenzo Albertazzi, and Fabio Beltram. 2010. "Simultaneous Intracellular Chloride and PH Measurements Using a GFP-Based Sensor." *Nature Methods* 7 (7): 516–18. https://doi.org/10.1038/nmeth.1471.

Assenza, Giovanni, Fioravante Capone, Lazzaro di Biase, Florinda Ferreri, Lucia Florio, Andrea Guerra, Massimo Marano, et al. 2017. "Oscillatory Activities in Neurological Disorders of Elderly: Biomarkers to Target for Neuromodulation." *Frontiers in Aging Neuroscience* 9 (JUN): 1–18. https://doi.org/10.3389/fnagi.2017.00189.

Atallah, Bassam V., William Bruns, Matteo Carandini, and Massimo Scanziani. 2012. "Parvalbumin-Expressing Interneurons Linearly Transform Cortical Responses to Visual Stimuli." *Neuron* 73 (1): 159–70. https://doi.org/10.1016/j.neuron.2011.12.013.

Avoli, M, M Barbarosie, A Lücke, T Nagao, V Lopantsev, and R Köhling. 1996. "Synchronous GABA-Mediated Potentials and Epileptiform Discharges in the Rat Limbic System in Vitro." *The Journal of Neuroscience : The Official Journal of the Society for Neuroscience* 16 (12): 3912–24. http://www.ncbi.nlm.nih.gov/pubmed/8656285.

Baroncelli, Laura, Joyce Bonaccorsi, Marco Milanese, Tiziana Bonifacino, Francesco Giribaldi, Ilaria Manno, Maria Cristina Cenni, et al. 2012. "Enriched Experience and Recovery from Amblyopia in Adult Rats: Impact of Motor, Social and Sensory Components." *Neuropharmacology* 62 (7): 2388–97. http://www.ncbi.nlm.nih.gov/pubmed/22532989.

Beaussart, M. 1975. "[Benign Epilepsy of Children with Rolandic Paroxysmal Electroencephalographic Foci]." *Pediatrie* 30 (3): 249–63. http://ovidsp.ovid.com/ovidweb.cgi?T=JS&CSC=Y&NEWS=N&PAGE=fulltext&D=med1&AN=809743%5Cnhttp://openurl.ac.uk/athens:_edu//lfp/LinkFinderPlus/Display?sid=OVID:Ovid+MEDLINE(R)&id=pmid:809743&id=&issn=0031-4021&isbn=&volume=30&issue=3&spage=249&pages=249-63&d.

Bédard, Claude, Helmut Kröger, and Alain Destexhe. 2004. "Modeling Extracellular Field Potentials and the Frequency-Filtering Properties of Extracellular Space." *Biophysical Journal* 86 (3): 1829–42. https://doi.org/10.1016/S0006-3495(04)74250-2.

Beghi, E, G Giussani, S Grosso, A Iudice, A La Neve, F Pisani, L M Specchio, et al. 2013. "Withdrawal of Antiepileptic Drugs: Guidelines of the Italian League Against Epilepsy." *Epilepsia* 54 (SUPPL.7): 2–12. https://doi.org/10.1111/epi.12305.

Ben-Ari, Yehezkel. 2002. "Excitatory Actions of GABA during Development: The Nature of the Nurture." *Nature Reviews Neuroscience* 3 (9): 728–39. https://doi.org/10.1038/nrn920.

Besag, F M C. 1995. "The Therapeutic Dilemma: Treating Subtle Seizures or Indulging in Electroencephalogram Cosmetics?" *Seminars in Pediatric Neurology* 2 (4): 261–68. https://doi.org/10.1016/S1071-9091(95)80005-0.

Binnie, C D. 2003. "Cognitive Impairment during Epileptiform Discharges: Is It Ever Justifiable to Treat the EEG?" *Lancet Neurology* 2 (12): 725–30. https://doi.org/10.1016/S1474-4422(03)00584-2.

Bizzarri, Ranieri, Caterina Arcangeli, Daniele Arosio, Fernanda Ricci, Paolo Faraci, Francesco Cardarelli, and Fabio Beltram. 2006. "Development of a Novel GFP-Based Ratiometric Excitation and Emission PH Indicator for Intracellular Studies." *Biophysical Journal* 90 (9): 3300–3314. https://doi.org/10.1529/biophysj.105.074708.

Bourgeois, Blaise F D. 2004. "Determining the Effects of Antiepileptic Drugs on Cognitive Function in Pediatric Patients with Epilepsy." *Journal of Child Neurology* 19 Suppl 1: S15--24. https://doi.org/10.1177/088307380401900103.

Brainard, David H. 1997. "The Psychophysics Toolbox." *Journal of Chemical Information and Modeling* 10 (4): 433–36. https://doi.org/10.1017/CBO9781107415324.004.

Buzsáki, György, Costas A. Anastassiou, and Christof Koch. 2012. "The Origin of Extracellular Fields and Currents-EEG, ECoG, LFP and Spikes." *Nature Reviews Neuroscience* 13 (6): 407–20. https://doi.org/10.1038/nrn3241.

Buzsáki, György, and Andreas Draguhn. 2004. "Neuronal Oscillations in Cortical Networks." *Science (New York, N.Y.)* 304 (5679): 1926–29. https://doi.org/10.1126/science.1099745.

Buzsáki, György, and Xiao-Jing Wang. 2012. "Mechanisms of Gamma Oscillations." *Annual Review of Neuroscience* 35 (1): 203–25. https://doi.org/10.1146/annurev-neuro-062111-150444.

Chatrian, G. E., C-M. Shaw, and H. Leffman. 1964. "The Significance of Periodic Lateralized Epileptiform Discharges in EEG:An Electrographic, Clinical and Pathological Study." *Electroencephalogr Clin Neurophysiol*, 177–93. https://doi.org/10.1016/0013-4694(64)90149-X.

"Chronux Toolbox." n.d. http://chronux.org/.

Collins, R C, and T V Caston. 1979. "Activation of Cortical Circuits during Interictal Spikes." *Annals of Neurology* 6 (2): 117--25 ST-- Activation of cortical circuits duri. https://doi.org/10.1002/ana.410060207 ET - 1979/08/01.

Contreras, D, and M Steriade. 1995. "Cellular Basis of EEG Slow Rhythms: A Study of Dynamic Corticothalamic Relationships." *The Journal of Neuroscience* 15 (1 Pt 2): 604–22.

Costales, Jesse L, and Alexander Kolevzon. 2015. "Phelan-McDermid Syndrome and SHANK3: Implications for Treatment." *Neurotherapeutics : The Journal of the American Society for Experimental NeuroTherapeutics* 12 (3): 620–30. https://doi.org/10.1007/s13311-015-0352-z.

Cozzolino, Olga, Maria Marchese, Francesco Trovato, Enrico Pracucci, Gian Michele Ratto, Maria Gabriella Buzzi, Federico Sicca, and Filippo M. Santorelli. 2018. "Understanding Spreading Depression from Headache to Sudden Unexpected Death." *Frontiers in Neurology* 9 (FEB): 1–13. https://doi.org/10.3389/fneur.2018.00019.

Cross, J Helen, and Brian G R Neville. 2009. "The Surgical Treatment of Landau-Kleffner Syndrome." *Epilepsia* 50 (SUPPL. 7): 63–67. https://doi.org/10.1111/j.1528-1167.2009.02223.x.

Crunelli, Vincenzo, Francois David, Magor L. Lorincz, and Stuart W. Hughes. 2015. "The Thalamocortical Network as a Single Slow Wave-Generating Unit." *Current Opinion in Neurobiology* 31: 72–80. https://doi.org/10.1016/j.conb.2014.09.001.

Curtis, M de, a Manfridi, and G Biella. 1998. "Activity-Dependent PH Shifts and Periodic Recurrence of Spontaneous Interictal Spikes in a Model of Focal Epileptogenesis." *The Journal of Neuroscience : The Official Journal of the Society for Neuroscience* 18 (18): 7543–51.

Curtis, M de, C Radici, and M Forti. 1999. "Cellular Mechanisms Underlying Spontaneous Interictal Spikes in an Acute Model of Focal Cortical Epileptogenesis." *Neuroscience* 88 (1): 107–17. https://doi.org/10.1016/S0306-4522(98)00201-2.

Curtis, Marco de, John G R Jefferys, and Massimo Avoli. 2012. "Interictal Epileptiform Discharges in Partial Epilepsy." In *Jasper's Basic Mechanisms of the Epilepsies 4th Edition.*, edited by Jeffrey L Noebels, Massimo Avoli, M A Rogawski, Richard W Olsen, and Antonio V Delgado-Escueta, 4th ed. Bethesda (MD): Oxford University Press.

Delpire, Eric. 2000. "Cation-Chloride Cotransporters in Neuronal Communication." *News in Physiological Sciences : An International Journal of Physiology Produced Jointly by the International Union of Physiological Sciences and the American Physiological Society* 15 (December): 309–12. http://www.ncbi.nlm.nih.gov/pubmed/11390932.

Delpire, Eric, and Kenneth B Gagnon. 2018. "Na+ -K+ -2Cl- Cotransporter (NKCC) Physiological Function in Nonpolarized Cells and Transporting Epithelia." *Comprehensive Physiology* 8 (2): 871–901. https://doi.org/10.1002/cphy.c170018.

Delpire, Eric, and Kevin J. Staley. 2014. "Novel Determinants of the Neuronal Cl- Concentration." *Journal of Physiology* 592 (19): 4099–4114. https://doi.org/10.1113/jphysiol.2014.275529.

Deonna, T W. 1991. "Acquired Epileptiform Aphasia in Children (Landau-Kleffner Syndrome)." *Journal of Clinical Neurophysiology* 8 (3): 288–98.

Duffy, Frank H, Gloria B McAnulty, Michelle C McCreary, George J Cuchural, and Anthony L Komaroff. 2011. "EEG Spectral Coherence Data Distinguish Chronic Fatigue Syndrome Patients from Healthy Controls and Depressed Patients-A Case Control Study." *BMC Neurology* 11 (1): 82. https://doi.org/10.1186/1471-2377-11-82.

Duncan, John S, Josemir W Sander, Sanjay M Sisodiya, and Matthew C Walker. 2006. "Adult Epilepsy." *Lancet (London, England)* 367 (9516): 1087–1100. https://doi.org/10.1016/S0140-6736(06)68477-8.

Dupret, D., B. Pleydell-Bouverie, and J. Csicsvari. 2008. "Inhibitory Interneurons and Network Oscillations." *Proceedings of the National Academy of Sciences* 105 (47): 18079–80. https://doi.org/10.1073/pnas.0810064105.

Elger, Christian E, Christoph Helmstaedter, and Martin Kurthen. 2004. "Review Chronic Epilepsy and Cognition." *Neurology* 3 (November): 663–72.

Esghaei, Moein, Mohammad Reza Daliri, and Stefan Treue. 2017. "Local Field Potentials Are Induced

by Visually Evoked Spiking Activity in Macaque Cortical Area MT." *Scientific Reports* 7 (1): 1–11. https://doi.org/10.1038/s41598-017-17372-4.

Fisher, Robert S., J. Helen Cross, Carol D'Souza, Jacqueline A. French, Sheryl R. Haut, Norimichi Higurashi, Edouard Hirsch, et al. 2018. "Instruction Manual for the ILAE 2017 Operational Classification of Seizure Types." *Zeitschrift Fur Epileptologie* 31 (4): 282–95. https://doi.org/10.1007/s10309-018-0217-7.

Fisher, Robert S. 1989. "Animal Models of the Epilepsies." *Brain Research Reviews* 14 (3): 245–78. https://doi.org/10.1016/0165-0173(89)90003-9.

Fisher, Robert S, Carlos Acevedo, Alexis Arzimanoglou, Alicia Bogacz, J Helen Cross, Christian E Elger, Jerome Engel, et al. 2014. "ILAE Official Report: A Practical Clinical Definition of Epilepsy." *Epilepsia* 55 (4): 475–82. https://doi.org/10.1111/epi.12550.

Frauscher, Birgit, Nicolás von Ellenrieder, Taissa Ferrari-Marinho, Massimo Avoli, François Dubeau, and Jean Gotman. 2015. "Facilitation of Epileptic Activity during Sleep Is Mediated by High Amplitude Slow Waves." *Brain* 138: 1629–41. https://doi.org/10.1093/brain/awv073.

Gelinas, Jennifer N, Dion Khodagholy, Thomas Thesen, Orrin Devinsky, and György Buzsáki. 2016. "Interictal Epileptiform Discharges Induce Hippocampal–Cortical Coupling in Temporal Lobe Epilepsy." *Nature Medicine* advance on (April). https://doi.org/10.1038/nm.4084.

Gray, Charles M., Pedro E. Maldonado, Mathew Wilson, and Bruce McNaughton. 1995. "Tetrodes Markedly Improve the Reliability and Yield of Multiple Single-Unit Isolation from Multi-Unit Recordings in Cat Striate Cortex." *Journal of Neuroscience Methods* 63 (1–2): 43–54. https://doi.org/10.1016/0165-0270(95)00085-2.

Guzzetta, Andrea, Sara Baldini, Ada Bancale, Laura Baroncelli, Francesca Ciucci, Paolo Ghirri, Elena Putignano, et al. 2009. "Massage Accelerates Brain Development and the Maturation of Visual Function." *The Journal of Neuroscience : The Official Journal of the Society for Neuroscience* 29 (18): 6042–51. https://doi.org/10.1523/JNEUROSCI.5548-08.2009.

Halász, Péter, Róbert Bódizs, Péter Przemyslaw Ujma, Dániel Fabó, and Anna Szűcs. 2019. "Strong Relationship between NREM Sleep, Epilepsy and Plastic Functions - A Conceptual Review on the Neurophysiology Background." *Epilepsy Research* 150: 95–105. https://doi.org/10.1016/j.eplepsyres.2018.11.008.

Heise, Christopher, Jan C. Schroeder, Michael Schoen, Sonja Halbedl, Dominik Reim, Sarah Woelfle, Michael R. Kreutz, Michael J. Schmeisser, and Tobias M. Boeckers. 2016. "Selective Localization of Shanks to VGLUT1-Positive Excitatory Synapses in the Mouse Hippocampus." *Frontiers in Cellular Neuroscience* 10 (April). https://doi.org/10.3389/fncel.2016.00106.

Hernan, Amanda E., Abigail Alexander, Pierre Pascal Lenck-Santini, Rod C. Scott, and Gregory L. Holmes. 2014. "Attention Deficit Associated with Early Life Interictal Spikes in a Rat Model Is Improved with ACTH." *PLoS ONE* 9 (2). https://doi.org/10.1371/journal.pone.0089812.

Hirase, Hajime, Lifen Qian, Peter Barthó, and György Buzsáki. 2004. "Calcium Dynamics of Cortical Astrocytic Networks in Vivo." *PLoS Biology* 2 (4): E96. https://doi.org/10.1371/journal.pbio.0020096.

Hohn, Vanessa D, Danielle M J de Veld, Kawita J S Mataw, Eus J W van Someren, and Sander Begeer. 2019. "Insomnia Severity in Adults with Autism Spectrum Disorder Is Associated with Sensory Hyper-Reactivity and Social Skill Impairment." *Journal of Autism and Developmental Disorders* 49 (5): 2146–55. https://doi.org/10.1007/s10803-019-03891-8.

Holmes, Gregory L. 2013. "EEG Abnormalities as a Biomarker for Cognitive Comorbidities in

Pharmacoresistant Epilepsy." *Epilepsia* 54 Suppl 2: 60–62. https://doi.org/10.1111/epi.12186.

Holmes, Gregory L, and Pierre Pascal Lenck-Santini. 2006. "Role of Interictal Epileptiform Abnormalities in Cognitive Impairment." *Epilepsy and Behavior* 8 (3): 504–15. https://doi.org/10.1016/j.yebeh.2005.11.014.

Holt, Abbey B., Eszter Kormann, Alessandro Gulberti, Monika Pötter-Nerger, Colin G. McNamara, Hayriye Cagnan, Magdalena K. Baaske, et al. 2019. "Phase-Dependent Suppression of Beta Oscillations in Parkinson's Disease Patients." *The Journal of Neuroscience* 39 (6): 1119–34. https://doi.org/10.1523/jneurosci.1913-18.2018.

Hughes, John R. 2011. "A Review of the Relationships between Landau-Kleffner Syndrome, Electrical Status Epilepticus during Sleep, and Continuous Spike-Waves during Sleep." *Epilepsy and Behavior* 20 (2): 247–53. https://doi.org/10.1016/j.yebeh.2010.10.015.

Hutt, S J, J Newton, and H Fairweather. 1977. "Choice Reaction Time and EEG Activity in Children with Epilepsy." *Neuropsychologia* 15 (2): 257–67. https://doi.org/10.1016/0028-3932(77)90034-3.

Irwin, K, V Birch, J Lees, C Polkey, G Alarcon, C Binnie, M Smedley, G Baird, and R O Robinson. 2001. "Multiple Subpial Transection in Landau-Kleffner Syndrome." *Developmental Medicine and Child Neurology* 43 (4): 248–52. https://doi.org/10.1017/S0012162201000470.

Kaila, K. 1994. "Ionic Basis of GABAA Receptor Channel Function in the Nervous System." *Progress in Neurobiology* 42 (4): 489–537. http://www.ncbi.nlm.nih.gov/pubmed/7522334.

Kaila, Kai, Theodore J. Price, John A. Payne, Martin Puskarjov, and Juha Voipio. 2014. "Cation-Chloride Cotransporters in Neuronal Development, Plasticity and Disease." *Nature Reviews Neuroscience* 15 (10): 637–54. https://doi.org/10.1038/nrn3819.

Kleen, Jonathan K, Rod C Scott, Gregory L Holmes, David W Roberts, Melissa M Rundle, Markus Testorf, Pierre Pascal Lenck-Santini, and Barbara C Jobst. 2013. "Hippocampal Interictal Epileptiform Activity Disrupts Cognition in Humans." *Neurology* 81 (1): 18–24. https://doi.org/10.1212/WNL.0b013e318297ee50.

Kleiner, Mario, David Brainard, and Denis Pelli. 2007. "What's New in Psychtoolbox-3?" In *European Conference on Visual Perception*. https://doi.org/10.1068/v070821.

Kobayashi, Eliane, A. P. Bagshaw, A. Jansen, F. Andermann, E. Andermann, J. Gotman, and F. Dubeau. 2005. "Intrinsic Epileptogenicity in Polymicrogyric Cortex Suggested by EEG-FMRI BOLD Responses." *Neurology* 64 (7): 1263–66. https://doi.org/10.1212/01.WNL.0000154640.23656.A3.

Kobayashi, Eliane, Andrew P. Bagshaw, Christophe Grova, Jean Gotman, and François Dubeau. 2006. "Grey Matter Heterotopia: What EEG-FMRI Can Tell Us about Epileptogenicity of Neuronal Migration Disorders." *Brain* 129 (2): 366–74. https://doi.org/10.1093/brain/awh710.

Krauss, G L, M Summerfield, J Brandt, S Breiter, and D Ruchkin. 1997. "Mesial Temporal Spikes Interfere with Working Memory." *Neurology* 49 (4): 975–80. https://doi.org/10.1212/WNL.49.4.975.

Krestel, Heinz E, Arto Nirkko, Andreas Von Allmen, Christian Liechti, Janine Wettstein, Antoinette Mosbacher, and Johannes Mathis. 2011. "Spike-Triggered Reaction-Time EEG as a Possible Assessment Tool for Driving Ability." *Epilepsia* 52 (10): 126–29. https://doi.org/10.1111/j.1528-1167.2011.03252.x.

Kyllerman, Mårten. 2013. "Angelman Syndrome." In , 287–90. https://doi.org/10.1016/B978-0-444-

52891-9.00032-4.

Landi, Silvia, Luigi Petrucco, Federico Sicca, and Gian Michele Ratto. 2019. "Transient Cognitive Impairment in Epilepsy." *Frontiers in Molecular Neuroscience* 11 (January): 252–67. https://doi.org/10.3389/fnmol.2018.00458.

Lenck-Santini, Pierre-Pascal, and Rodney C Scott. 2015. "Mechanisms Responsible for Cognitive Impairment in Epilepsy." *Cold Spring Harbor Perspectives in Medicine*, a022772. https://doi.org/10.1101/cshperspect.a022772.

Lévesque, Maxime, Pariya Salami, Charles Behr, and Massimo Avoli. 2013. "Temporal Lobe Epileptiform Activity Following Systemic Administration of 4-Aminopyridine in Rats." *Epilepsia* 54 (4): 596–604. https://doi.org/10.1111/epi.12041.

Ma, Hong-Tao, Cai-Hong Wu, and Jian-Young Wu. 2004. "Initiation of Spontaneous Epileptiform Events in the Rat Neocortex in Vivo." *Journal of Neurophysiology* 91 (2): 934–45. https://doi.org/10.1152/jn.00274.2003.

Massimini, Marcello, Reto Huber, Fabio Ferrarelli, Sean Hill, and Giulio Tononi. 2004. "The Sleep Slow Oscillation as a Traveling Wave." *Journal of Neuroscience* 24 (31): 6862–70. https://doi.org/10.1523/JNEUROSCI.1318-04.2004.

Meldrum, B S. 1971. "Convulsive Effects of 4-Deoxypyridoxine in Photosensitive Baboons (Papio Papio)." *Brain Research* 41 (2): 403P.

Miller, John W. 2011. "Stopping Seizures with Carbon Dioxide." *Epilepsy Currents* 11 (4): 114–15. https://doi.org/10.5698/1535-7511-11.4.114.

Mitra, Partha, and Hemant Bokil. 2007. *Observed Brain Dynamics*. Oxford University Press. https://doi.org/10.1093/acprof:oso/9780195178081.001.0001.

Mohajerani, M H, D A McVea, M Fingas, and T H Murphy. 2010. "Mirrored Bilateral Slow-Wave Cortical Activity within Local Circuits Revealed by Fast Bihemispheric Voltage-Sensitive Dye Imaging in Anesthetized and Awake Mice." *The Journal of Neuroscience* 30 (10): 3745–51. https://doi.org/10.1523/JNEUROSCI.6437-09.2010.

Morrell, F, W W Whisler, and T P Bleck. 1989. "Multiple Subpial Transection: A New Approach to the Surgical Treatment of Focal Epilepsy." *Journal of Neurosurgery* 70 (2): 231–39. https://doi.org/10.3171/jns.1989.70.2.0231.

Mukherjee, Sreedeep, and Denise Manahan-Vaughan. 2013. "Role of Metabotropic Glutamate Receptors in Persistent Forms of Hippocampal Plasticity and Learning." *Neuropharmacology* 66: 65–81. https://doi.org/10.1016/j.neuropharm.2012.06.005.

Nicolai, Joost, Saskia Ebus, Danielle P L J J G Biemans, Johan Arends, Jos Hendriksen, Johan S H Vles, and Albert P Aldenkamp. 2012. "The Cognitive Effects of Interictal Epileptiform EEG Discharges and Short Nonconvulsive Epileptic Seizures." *Epilepsia* 53 (6): 1051–59. https://doi.org/10.1111/j.1528-1167.2012.03491.x.

Noachtar, S, C Binnie, J Ebersole, F Mauguière, A Sakamoto, and B Westmoreland. 1999. "A Glossary of Terms Most Commonly Used by Clinical Electroencephalographers and Proposal for the Report Form for the EEG Findings. The International Federation of Clinical Neurophysiology." *Electroencephalography and Clinical Neurophysiology.* 52: 21–41. https://doi.org/10.1055/s-2003-812583.

Ool, Jans S van, Francesca M Snoeijen-Schouwenaars, Helenius J Schelhaas, In Y Tan, Albert P Aldenkamp, and Jos G M Hendriksen. 2016. "A Systematic Review of Neuropsychiatric

Comorbidities in Patients with Both Epilepsy and Intellectual Disability." *Epilepsy and Behavior* 60: 130–37. https://doi.org/10.1016/j.yebeh.2016.04.018.

Orefice, Lauren L., Jacqueline R. Mosko, Danielle T. Morency, Michael F. Wells, Aniqa Tasnim, Shawn M. Mozeika, Mengchen Ye, et al. 2019. "Targeting Peripheral Somatosensory Neurons to Improve Tactile-Related Phenotypes in ASD Models." *Cell* 178 (4): 867-886.e24. https://doi.org/10.1016/j.cell.2019.07.024.

Pavlov, Ivan, Kai Kaila, Dimitri M Kullmann, and Richard Miles. 2013. "Cortical Inhibition, PH and Cell Excitability in Epilepsy: What Are Optimal Targets for Antiepileptic Interventions?" *The Journal of Physiology* 591 (4): 765–74. https://doi.org/10.1113/jphysiol.2012.237958.

Pederzoli, Francesca, Barbara Ruozi, Enrico Pracucci, Giovanni Signore, Mauro Zapparoli, Flavio Forni, Maria Angela Vandelli, Gian Michele Ratto, and Giovanni Tosi. 2016. "Nanoimaging : Photophysical and Pharmaceutical Characterization of Poly- Lactide-Co-Glycolide Nanoparticles Engineered with Quantum Dots." *Nanotechnology* 27. https://doi.org/10.1088/0957-4484/27/1/015704.

Pelli, D G. 1997. "The VideoToolbox Software for Visual Psychophysics: Transforming Numbers into Movies." *Spatial Vision* 10 (4): 437–42. http://www.ncbi.nlm.nih.gov/pubmed/9176953.

Petrucco, L., E. Pracucci, M. Brondi, G. M. Ratto, and S. Landi. 2017. "Epileptiform Activity in the Mouse Visual Cortex Interferes with Cortical Processing in Connected Areas." *Scientific Reports* 7 (August 2016): 1–12. https://doi.org/10.1038/srep40054.

Piers, Thomas M, Dong Hyun Kim, Byeong C Kim, Philip Regan, Daniel J Whitcomb, and Kwangwook Cho. 2012. "Translational Concepts of MGluR5 in Synaptic Diseases of the Brain" 3 (November): 1–7. https://doi.org/10.3389/fphar.2012.00199.

Pizzorusso, Tommaso, Paolo Medini, Silvia Landi, Sara Baldini, Nicoletta Berardi, and Lamberto Maffei. 2006. "Structural and Functional Recovery from Early Monocular Deprivation in Adult Rats." *Proceedings of the National Academy of Sciences of the United States of America* 103 (22): 8517–22. https://doi.org/10.1073/pnas.0602657103.

Porciatti, Vittorio, Tommaso Pizzorusso, and Lamberto Maffei. 1999. "The Visual Physiology of the Wild Type Mouse Determined with Pattern VEPs." *Vision Research* 39 (18): 3071–81. https://doi.org/10.1016/S0042-6989(99)00022-X.

Pouille, Frédéric, Antonia Marin-Burgin, Hillel Adesnik, Bassam V Atallah, and Massimo Scanziani. 2009. "Input Normalization by Global Feedforward Inhibition Expands Cortical Dynamic Range." *Nature Neuroscience* 12 (12): 1577–85. https://doi.org/10.1038/nn.2441.

Reig, R, Y Zerlaut, R Vergara, A Destexhe, and M V Sanchez-Vives. 2015. "Gain Modulation of Synaptic Inputs by Network State in Auditory Cortex In Vivo." *Journal of Neuroscience* 35 (6): 2689–2702. https://doi.org/10.1523/JNEUROSCI.2004-14.2015.

Ridder, W H, and S Nusinowitz. 2006. "The Visual Evoked Potential in the Mouse--Origins and Response Characteristics." *Vision Research* 46 (6–7): 902–13. https://doi.org/10.1016/j.visres.2005.09.006.

Sala, Carlo, Cinzia Vicidomini, Ilaria Bigi, Adele Mossa, and Chiara Verpelli. 2015. "Shank Synaptic Scaffold Proteins: Keys to Understanding the Pathogenesis of Autism and Other Synaptic Disorders." *Journal of Neurochemistry* 135 (5): 849–58. https://doi.org/10.1111/jnc.13232.

Sale, Alessandro, José Fernando Maya Vetencourt, Paolo Medini, Maria Cristina Cenni, Laura Baroncelli, Roberto De Pasquale, and Lamberto Maffei. 2007. "Environmental Enrichment in Adulthood Promotes Amblyopia Recovery through a Reduction of Intracortical Inhibition."

Nature Neuroscience 10 (6): 679–81. https://doi.org/10.1038/nn1899.

Salinas, Emilio, Peter Thier, and La Jolla. 2000. "Gain Modulation : A Major Computational Principle of the Central Nervous System A Lot Is Known about How Neurons in the Brain Represent A Brief History of Gain Fields." *Neuron* 27 (x): 15–21.

Sarasua, Sara M., Luigi Boccuto, Julia L. Sharp, Alka Dwivedi, Chin Fu Chen, Jonathan D. Rollins, R. Curtis Rogers, Katy Phelan, and Barbara R. DuPont. 2014. "Clinical and Genomic Evaluation of 201 Patients with Phelan-McDermid Syndrome." *Human Genetics* 133 (7): 847–59. https://doi.org/10.1007/s00439-014-1423-7.

Scheffer, Ingrid E., Samuel Berkovic, Guiseppe Capovilla, Mary B. Connolly, Jacqueline French, Laura Guilhoto, Edouard Hirsch, et al. 2018. "ILAE Classification of the Epilepsies: Position Paper of the ILAE Commission for Classification and Terminology." *Zeitschrift Fur Epileptologie* 31 (4): 296–306. https://doi.org/10.1007/s10309-018-0218-6.

Schmeisser, Michael J, Elodie Ey, Stephanie Wegener, Juergen Bockmann, A Vanessa Stempel, Angelika Kuebler, Anna-Lena Janssen, et al. 2012. "Autistic-like Behaviours and Hyperactivity in Mice Lacking ProSAP1/Shank2." *Nature* 486 (7402): 256–60. https://doi.org/10.1038/nature11015.

Schroeder, C E, C E Tenke, S J Givre, J C Arezzo, and H G Vaughan. 1990. "Laminar Analysis of Bicuculline-Induced Epileptiform Activity in Area 17 of the Awake Macaque." *Brain Research* 515 (1–2): 326–30. http://www.ncbi.nlm.nih.gov/pubmed/2357572.

Schwartz, T H, and T Bonhoeffer. 2001. "In Vivo Optical Mapping of Epileptic Foci and Surround Inhibition in Ferret Cerebral Cortex." *Nature Medicine* 7 (9): 1063–67. https://doi.org/10.1038/nm0901-1063.

Schwartzkroin, Philip A, Kin J Futamachi, Jeffrey L Noebels, and David A Prince. 1975. "Transcallosal Effects of a Cortical Epileptiform Focus." *Brain Research* 99 (1): 59–68. https://doi.org/10.1016/0006-8993(75)90608-3.

Sela, Yaniv, Vladyslav V Vyazovskiy, Chiara Cirelli, Giulio Tononi, and Yuval Nir. 2016. "Responses in Rat Core Auditory Cortex Are Preserved during Sleep Spindle Oscillations." *Sleep*. https://doi.org/10.5665/sleep.5758.

Sherwin, Ira. 1982. "Fine-Structure Differences of Unit Firing Patterns Penicillin-Induced Primary and Secondary Epileptogenic Foci." *Experimental Neurology* 275: 263–75.

Shewmon, D A, and R J Erwin. 1988. "The Effect of Local Interictal Spikes on Perception and Reaction Time. I. General Considerations." *Electroencephalography and Clinical Neurophysiology* 69: 319–37.

Sulis Sato, Sebastian, Pietro Artoni, Silvia Landi, Olga Cozzolino, Riccardo Parra, Enrico Pracucci, Francesco Trovato, et al. 2017. "Simultaneous Two-Photon Imaging of Intracellular Chloride Concentration and PH in Mouse Pyramidal Neurons in Vivo." *Proceedings of the National Academy of Sciences* 114 (41): E8770–79. https://doi.org/10.1073/pnas.1702861114.

Tombaugh, G C, and G G Somjen. 1996. "Effects of Extracellular PH on Voltage-Gated Na+, K+ and Ca2+ Currents in Isolated Rat CA1 Neurons." *The Journal of Physiology* 493 (Pt 3 (June): 719–32. https://doi.org/10.1113/jphysiol.1996.sp021417.

Tononi, Giulio, and Chiara Cirelli. 2014. "Sleep and the Price of Plasticity: From Synaptic and Cellular Homeostasis to Memory Consolidation and Integration." *Neuron* 81 (1): 12–34. https://doi.org/10.1016/j.neuron.2013.12.025.

Traynelis, S F, and S G Cull-Candy. 1990. “Proton Inhibition of N-Methyl-D-Aspartate Receptors in Cerebellar Neurons.” *Nature* 345 (6273): 347–50. https://doi.org/10.1038/345347a0.

Trevelyan, Andrew J, Willy Bruns, Edward O Mann, Valerie Crepel, and Massimo Scanziani. 2013. “The Information Content of Physiological and Epileptic Brain Activity.” *The Journal of Physiology* 591 (Pt 4): 799–805. https://doi.org/10.1113/jphysiol.2012.240358.

Uchino, Shigeo, and Chikako Waga. 2013. “SHANK3 as an Autism Spectrum Disorder-Associated Gene.” *Brain and Development* 35 (2): 106–10. https://doi.org/10.1016/j.braindev.2012.05.013.

Uva, Laura, Gian Luca Breschi, Vadym Gnatkovsky, Stefano Taverna, and M de Curtis. 2015. “Synchronous Inhibitory Potentials Precede Seizure-like Events in Acute Models of Focal Limbic Seizures.” *Journal of Neuroscience* 35 (7): 3048–55. https://doi.org/10.1523/JNEUROSCI.3692-14.2015.

Uva, Laura, Laura Librizzi, Fabrice Wendling, and Marco De Curtis. 2005. “Propagation Dynamics of Epileptiform Activity Acutely Induced by Bicuculline in the Hippocampal-Parahippocampal Region of the Isolated Guinea Pig Brain.” *Epilepsia* 46 (12): 1914–25. https://doi.org/10.1111/j.1528-1167.2005.00342.x.

Vannini, Eleonora, Anna Panighini, Chiara Cerri, Alessia Fabbri, Simonetta Lisi, Enrico Pracucci, Nicola Benedetto, et al. 2014. “The Bacterial Protein Toxin, Cytotoxic Necrotizing Factor 1 (CNF1) Provides Long-Term Survival in a Murine Glioma Model.” *BMC Cancer* 14 (1): 1–10. https://doi.org/10.1186/1471-2407-14-449.

Verpelli, Chiara, Elena Dvoretskova, Cinzia Vicidomini, Francesca Rossi, Michela Chiappalone, Michael Schoen, Bruno Di Stefano, et al. 2011. “Importance of Shank3 Protein in Regulating Metabotropic Glutamate Receptor 5 (MGluR5) Expression and Signaling at Synapses.” *The Journal of Biological Chemistry* 286 (40): 34839–50. https://doi.org/10.1074/jbc.M111.258384.

Vicidomini, C., L. Ponzoni, D. Lim, M. J. Schmeisser, D. Reim, N. Morello, D. Orellana, et al. 2017. “Pharmacological Enhancement of MGlu5 Receptors Rescues Behavioral Deficits in SHANK3 Knock-out Mice.” *Molecular Psychiatry* 22 (5): 689–702. https://doi.org/10.1038/mp.2016.30.

Vyazovskiy, Vladyslav V, and Kenneth D Harris. 2013. “Sleep and the Single Neuron: The Role of Global Slow Oscillations in Individual Cell Rest.” *Nature Reviews. Neuroscience* 14 (6): 443–51. https://doi.org/10.1038/nrn3494.

Wang, Xiao-Jing. 2010. “Neurophysiological and Computational Principles of Cortical Rhythms in Cognition.” *Physiological Reviews* 90 (3): 1195–1268. https://doi.org/10.1152/physrev.00035.2008.

Wang, Xiaoming, Qiong Xu, Alexandra L. Bey, Yoonji Lee, and Yong Hui Jiang. 2014. “Transcriptional and Functional Complexity of Shank3 Provides a Molecular Framework to Understand the Phenotypic Heterogeneity of SHANK3 Causing Autism and Shank3 Mutant Mice.” *Molecular Autism* 5 (1): 1–14. https://doi.org/10.1186/2040-2392-5-30.

Watt, J L, I A Olson, A W Johnston, H S Ross, D A Couzin, and G S Stephen. 1985. “A Familial Pericentric Inversion of Chromosome 22 with a Recombinant Subject Illustrating a ‘pure’ Partial Monosomy Syndrome.” *Journal of Medical Genetics* 22 (4): 283–87. https://doi.org/10.1136/jmg.22.4.283.

Weisman, David, and Ian McKeith. 2007. “Dementia with Lewy Bodies.” *Seminars in Neurology* 27 (1): 42–47. https://doi.org/10.1055/s-2006-956754.

Wiggins, Lisa D, Diana L Robins, Roger Bakeman, and Lauren B Adamson. 2009. “Brief Report: Sensory Abnormalities as Distinguishing Symptoms of Autism Spectrum Disorders in Young

Children." *Journal of Autism and Developmental Disorders* 39 (7): 1087–91. https://doi.org/10.1007/s10803-009-0711-x.

Xing, D., C.-I Yeh, and R. M. Shapley. 2009. "Spatial Spread of the Local Field Potential and Its Laminar Variation in Visual Cortex." *Journal of Neuroscience* 29 (37): 11540–49. https://doi.org/10.1523/jneurosci.2573-09.2009.

Xiong, Z Q, P Saggau, and J L Stringer. 2000. "Activity-Dependent Intracellular Acidification Correlates with the Duration of Seizure Activity." *The Journal of Neuroscience : The Official Journal of the Society for Neuroscience* 20 (4): 1290–96. http://www.ncbi.nlm.nih.gov/pubmed/10662818.

Yoo, Juyoun, Bakes Joseph, Bradley Clarrisa, Collingridge Graham L., and Kaang Bong-Kiun. 2014. "Shank Mutant Mice as an Animal Model of Autism." *Philosophical Transactions of the Royal Society B: Biological Sciences* 369 (1633): 20130143. https://doi.org/10.1098/rstb.2013.0143.

Zhou, Shanglin, and Yuguo Yu. 2018. "Synaptic E-I Balance Underlies Efficient Neural Coding." *Frontiers in Neuroscience* 12 (FEB): 1–11. https://doi.org/10.3389/fnins.2018.00046.

Zucca, Stefano, Giulia D'Urso, Valentina Pasquale, Dania Vecchia, Giuseppe Pica, Serena Bovetti, Claudio Moretti, et al. 2017. "An Inhibitory Gate for State Transition in Cortex." *ELife* 6: 1–31. https://doi.org/10.7554/eLife.26177.001.

Appendix

Code for delivering stimulation

This is the link to the GitHub page where I shared my code for the Matlab app that we used for presenting stimulation mice and humans:

https://github.com/eprk/EscherUDP

Arduino scheme of Hermes

In Figure 0.1 the scheme of the circuit of Hermes, based on an Arduino board. The sensor is the phototransistor LTP 20A ORSAM. The phototransistor output value is read by the analogic input A0, while the TTL output of the system is captioned as "TTL", in the bottom right corner. The switch connecting digital I/O D3 and D4 is used during the calibration phase of Hermes. Digital I/O pin D11, D12, D13 are connected to an RGB LED that is used as a status LED.

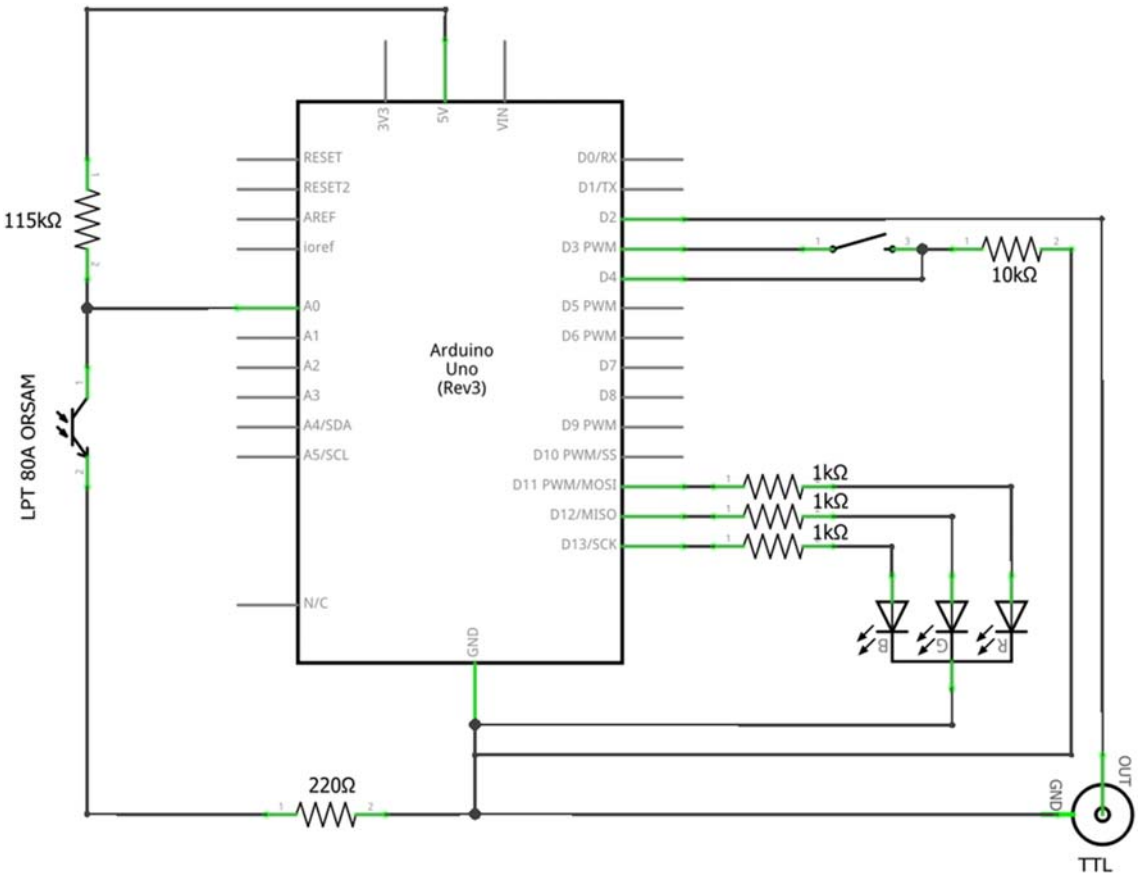

Figure 0.1: Schematics of Hermes circuit.

To operate the device, the Arduino board has to be loaded with the Hermes code for Arduino, that is provided at following link:

https://github.com/eprk/Hermes

Then there are some instructions to follow to calibrate Hermes at the beginning of the experimental session, before the actual experiment can start:

1. The Hermes sensor has to be properly connected and juxtaposed to a corner of the screen that is going to be used for stimulation.
2. On EscherApp, the position for the visual cue for Hermes must be selected (any of the four corners of the screen can be used).
3. Hermes must be connected to the power plug. If the code Hermes.ino was not loaded on the Arduino board, then it should be connected.
4. When Hermes is ready to start the calibration, the status LED should turn blue.
5. The calibration can be started: on EscherApp, press “Calibrate W”, to start white calibration. The screen should turn black with a white square in the corner where the sensor is located.
6. Press the calibration button on Hermes. The status LED should turn purple and start blinking.
7. When the status LED stops blinking and remains purple, press “Calibrate B” button on EscherApp. The screen should turn white with a black square in the corner where the sensor is located.
8. Press the calibrate button on Hermes again, and the status LED should start blinking in purple again.
9. The LED should stop blinking after a few seconds and become green. This means that Hermes is calibrated and the experiment can be started.